Rheology of Complex Fluid Films for Biological and Mechanical Adhesive Locomotion

by

Randy H. Ewoldt

B.S., Mechanical Engineering
Iowa State University (2004)

Submitted to the Department of Mechanical Engineering
in partial fulfillment of the requirements for the degree of

Master of Science in Mechanical Engineering

at the

MASSACHUSETTS INSTITUTE OF TECHNOLOGY

June 2006

Author .....
Department of Mechanical Engineering
May 12, 2006

Certified by .....
Anette Hosoi
Assistant Professor, Mechanical Engineering
Thesis Supervisor

Certified by .....
Gareth H. McKinley
Professor, Mechanical Engineering
Thesis Supervisor

Accepted by .....
Lallit Anand
Chairman, Department Committee on Graduate Students

Rheology of Complex Fluid Films for Biological and Mechanical Adhesive Locomotion

by

Randy H. Ewoldt

Submitted to the Department of Mechanical Engineering
on May 12, 2006, in partial fulfillment of the
requirements for the degree of
Master of Science in Mechanical Engineering

Abstract

Many gastropods, such as snails and slugs, crawl using adhesive locomotion, a technique that allows the organisms to climb walls and walk across ceilings. These animals stick to the crawling surface by excreting a thin layer of biopolymer mucin gel, known as pedal mucus, and their acrobatic ability is due in large part to the rheological properties of this slime. The primary application of the present research is to enable a mechanical crawler to climb walls and walk across ceilings using adhesive locomotion. A properly selected slime simulant will enable a mechanical crawler to optimally perform while climbing in the horizontal, inclined, and inverted positions.

To this end, the rheology of gastropod pedal mucus is examined in greater detail than any previously published work. The linear rheological response of pedal mucus is examined with flow, oscillation, and creep tests. Nonlinear rheology is examined with large amplitude oscillatory shear (LAOS), and analyzed with Lissajous curves, Fourier transform rheology, and a new measure of non-linear elasticity. In addition, pedal mucus is examined with a flexure-based microgap rheometer, which can test the sample at the biologically relevant gap of 10-20μm, the measured thickness of pedal mucus under a crawling slug.

Adhesive locomotion of a mechanical crawler is modeled in order to find the criteria for an optimal slime simulant. After developing the selection criteria for the ideal simulant, a range of candidate materials are examined including polymeric gels, particulate gels, emulsions, composites, and field-responsive fluids. Two promising simulants are examined in detail and compared with native gastropod pedal mucus.

Thesis Supervisor: Anette Hosoi
Title: Assistant Professor, Mechanical Engineering

Thesis Supervisor: Gareth H. McKinley
Title: Professor, Mechanical Engineering

Acknowledgments

I would like to thank the National Science Foundation Graduate Research Fellowship Program for financial support and the freedom to pursue this research, Brian Chan for his original idea to pursue a robotic snail, and my advisors Prof. Anette Hosoi and Prof. Gareth H. McKinley for their enthusiasm, encouragement, and confidence in me. Furthermore, I would like to thank Dr. Christian Clasen for his help with microgap rheology, and my numerous lab mates, colleagues, and friends for their support.

Finally, I am indebted to my wife Erin, who continues to be a constant source of wisdom, encouragement, and strength. A.M.D.G.

R.H.E.

Contents

List of Figures

List of Tables

Chapter 1

Introduction and Background

Many gastropods, such as snails and slugs, crawl using adhesive locomotion, a technique that allows the organisms to climb walls and walk across ceilings. These animals stick to the crawling surface with an excreted thin layer of biopolymer gel, known as pedal mucus, and their acrobatic ability is due in large part to the rheological properties of this slime.

The primary application of the present research is to enable a mechanical crawler to climb walls and walk across ceilings using adhesive locomotion. The mechanical design and fabrication is being pursued by a fellow student, Brian Chan [5]. A properly selected slime simulant will enable Chan's mechanical crawler to optimally perform while climbing in the horizontal, inclined, and inverted positions.

To this end, the rheology of gastropod pedal mucus is examined in greater detail than any previously published work. The linear rheology of pedal mucus is examined with flow, oscillation, and creep tests. Nonlinear rheology is examined with large amplitude oscillatory shear (LAOS) tests. In addition, pedal mucus is examined with microgap rheology, which can test the sample at the biologically relevant gap of 10-20μm, the measured thickness of pedal mucus under a crawling slug [6].

Adhesive locomotion of a mechanical crawler is modeled in order to find the criteria for an optimal slime simulant. After developing the selection criteria for the ideal simulant, a range of candidate materials are examined including polymeric gels, particulate gels, and emulsions. Two promising simulants are then examined in detail,

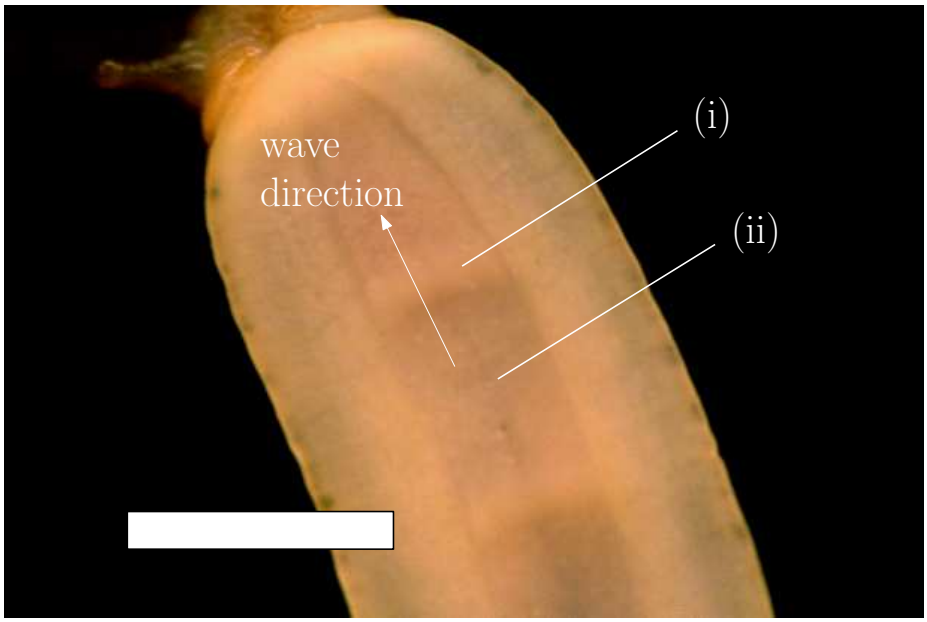

Figure 1-1: Bottom view of a crawling terrestrial slug *Limax maximus*, 1cm scale bar; i) compression wave, ii) interwave

.

and compared with native pedal mucus.

1.1 Adhesive locomotion

It has been known for some time that snails crawl upon a thin layer of excreted mucus, but the exact mechanism of gastropod locomotion was unclear until Denny examined the rheological properties of pedal mucus from the banana slug, *Ariolimax columbianus* [4, 6]. He discovered that the thin layer of mucus served both as glue and lubricant, holding part of the animal to the substrate while allowing another part to glide forward.

Animals that crawl using adhesive locomotion exert shear stresses on the thin layer of structurally sensitive mucus that holds the organism to the substrate. The pedal mucus has an effective yield stress; at high applied stresses the network structure breaks enabling the foot to glide forward over a fluid layer, whereas in regions of low applied stress the network structure reforms into a solid-like layer connecting the foot to the substrate. Molluscan pedal mucus films are physically crosslinked

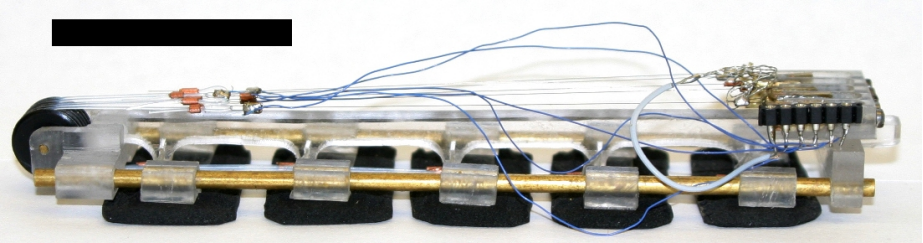

Figure 1-2: Chan's Robosnail mimics adhesive locomotion with five discrete pads which move forward sequentially while other pads remain stationary, 5cm scale bar.

gels containing 0.3-9.9% solid matter in water [7]. The solid constituent which dominates the mechanical properties is a mucus protein-polysaccharide complex. These glycoconjugates in pedal mucus share similarities with both mucin glycoproteins and glycosaminoglycans in vertebrates.

Figure 1-1 shows the bottom view of a crawling terrestrial slug, *Limax maximus*, commonly known as the leopard slug, tiger slug, or great gray garden slug. The muscular contractions lead to waves that (i) compress the foot parallel with the substrate, creating an area of high shear stress which ruptures the mucus network structure. The interwaves (ii) are areas of lower shear stress which allow the transient network structure to reform into a solid-like material, holding that part of the organism to the substrate. Muscular compression waves move toward the head (top of picture) during locomotion. With adhesive locomotion it is important to note that the thickness of pedal mucus between the foot and the substrate is constant; the waves are not peristaltic. However, other gastropods that do not use adhesive locomotion, such as many marine snails, instead use a peristaltic wave that propagates from the head toward the rear of the animal.

The adhesive locomotion mechanical crawler designed by Chan [5] is shown in Figure 1-2. The discrete pads can be individually actuated, creating an area of high shear stress under the single forward moving pad, while the remaining stationary pads exert a lower shear stress on the material. This so-called Robosnail2 is the basis of the adhesive locomotion modeling presented in Chapter 4.

1.2 Mucus composition

Mucus is a biological secretion common to both vertebrates and invertebrates, and is best known for coating cells that line the respiratory, digestive, and urogenital tracts. Mucus serves many functions, such as lubrication, protection from dehydration or infection, and assisting in adhesive locomotion. It is primarily composed of water, salts, and large biopolymer complexes made of proteins and polysaccharides. In vertebrates these large macromolecules are known as mucin, but for invertebrates the high molecular weight polymer is less defined. Much research has been directed at understanding human mucin, since mucus is related to a number of diseases (e.g. cystic fibrosis). Thus invertebrate mucus researchers have often looked to vertebrate mucin for insight (e.g. [7]).

1.2.1 Vertebrate mucus

Vertebrate mucin molecules are glycoproteins, consisting of a protein backbone onto which polysaccharides have covalently attached (glycosylation). Mucins are distinguished from other glycoproteins by heavy glycosylation, consisting of at least 50% *O*-glycans by weight which are concentrated in particular regions on the polypeptide core [1] (*O*-glycans are polysaccharides attached at the amino acids hydroxylysine, hydroxyproline, serine, or threonine, in contrast to *N*-glycans which are polysaccharides attached at asparagine). Mucins are identified by the gene which encodes the protein backbone. For example, in humans each gene name follows the form MUC#, in which chronologically identified mucins have been assigned a unique number. Common human mucins include MUC1, which can be found in the bronchus, salivary gland, and stomach, and MUC2, which is known to exist in the salivary gland, small intestine, and colon [8].

Mucins are classified into two distinct categories: membrane-bound mucins and secretory mucins. For human mucins, it has been suggested that six are membrane-bound (MUC1, MUC3A, MUC3B, MUC4, MUC12, and MUC13), four are secreted (MUC2, MUC5AC, MUC5B, and MUC6), and the remaining three mucins (MUC7,

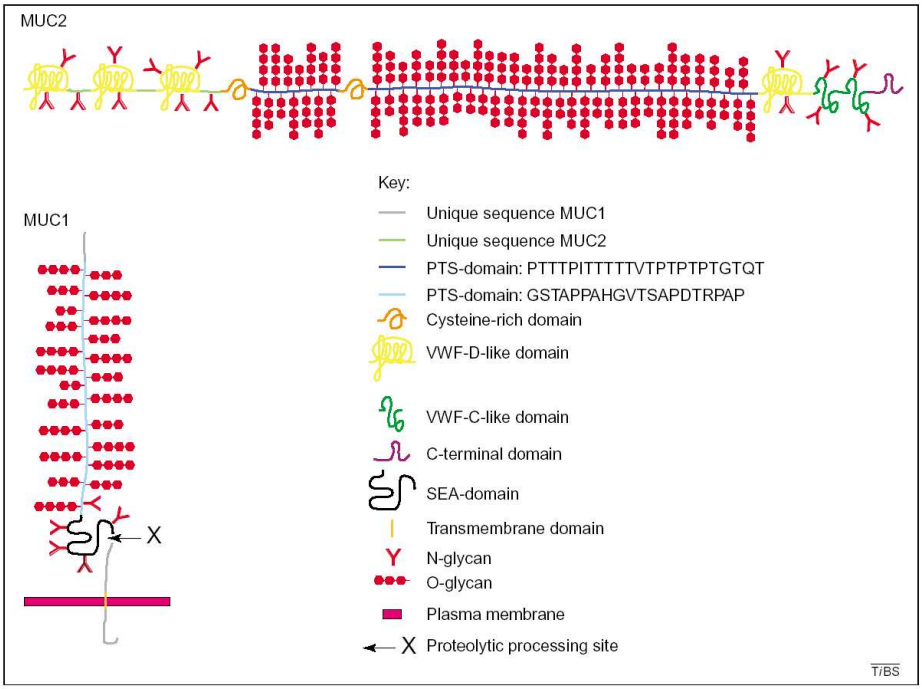

Figure 1-3: Schematic representation of two well characterized human mucins (from [1]); MUC1 is a membrane-bound mucin and MUC2 is a secretory mucin.

MUC8, and MUC16) cannot be classified [1]. Figure 1-3 (from [1]) compares the architecture of two well characterized human mucins, MUC1 and MUC2, and shows the contrast between a membrane-bound mucin (MUC1) and a secreted mucin (MUC2). Different domains of the protein backbone are distinguished by the amino acid sequence, in which the amino acid names are abbreviated to one letter. A table listing the amino acids and their abbreviations is included in Appendix A. Secreted mucins such as MUC2 are the primary interest of this research because they alone have the ability to form gels.

The part of the polypeptide core that is heavily *O*-glycosylated contains no secondary structure, and is held in an extended position by the polysaccharides. These *O*-glycans are mutually repulsive due to their negative charge [9]. Mucins therefore occupy a large volume with a small weight fraction when in solution. Individual mucin chains are assembled via disulphide bonds into molecules with molecular weights in the millions [9]. Secretory mucins may then form gels via entanglement and non-covalent bonding, such as hydrophobic interactions between protein segments [10].

1.2.2 Invertebrate mucus

Mucus is quite abundant among invertebrates. As mentioned in [11], most of the 99% of animals without backbones are bursting with mucus secretions. In contrast to vertebrate mucus, the constituent molecule of invertebrate mucus is not necessarily a traditional glycoprotein. Both protein and carbohydrate are present in invertebrate mucus, but these subunits are not ordered in the same way as glycoproteins. It has been suggested that the constituent molecules of invertebrate mucus are better described as protein-polysaccharide complexes [7]. While there is a clear distinction between glycoproteins and glycosaminoglycans for vertebrates, that distinction is blurred for invertebrate mucus. As suggested, the protein-polysaccharide complexes found in invertebrate mucus lie somewhere on the spectrum between a glycoprotein and a glycosaminoglycan. Whereas a glycoprotein consists of a distinct protein backbone onto which polysaccharides are attached, a glycosaminoglycan is a linear chain of predominantly carbohydrates with a small amount of protein.

Invertebrates also use their mucus secretions in unique ways compared to vertebrates. For example, gastropod slime trails are used for navigating and many invertebrates coat themselves with distasteful slime to detract predators [11].

1.3 Prior work on the rheology of mucus

This section reviews relevant studies of mucus rheology. Vertebrate mucus is kept distinct from invertebrate mucus to emphasize the difference in composition, as discussed in Section 1.2.2.

1.3.1 Vertebrate mucus

Many of the early studies of vertebrate mucus rheology focused on bronchial mucus, attempting to understand common disorders such as chronic bronchitis and cystic fibrosis. For example, [12] describes the role of mucus viscoelasticity in the ciliary transport of pulmonary secretions. Bronchial mucus is described with a Maxwell

model, which is an elastic spring in series with a viscous damper. More recently, [13] describes experimental methods for studying mucociliary clearance, including magnetic bead rheology using beads with a diameter of 100μm.

Rheology has been used to help elucidate the association mechanism of mucin molecules. For example, [10] has concluded that tracheobronchial mucin associates due to the hydrophobic attraction between protein segments. Additionally, native pig gastric mucus has been examined by [14], which concludes that that both transient (e.g. entanglements) and nontransient (e.g. physical gelation) associations are responsible for for the bulk rheological response of the material.

At yet a smaller scale, the mechanics of individual mucin subunits have been examined. For example, [15] uses atomic force microscopy (AFM) to measure the persistence length of human ocular mucins, which are present in the precorneal tear film. Ocular mucins possess short oligosaccharide side chains in comparison with many gastrointestinal mucins. The persistence length was found to be 36nm, which the authors say is consistent with that of an extended, flexible polymer.

Vertebrate mucus has been examined with nontraditional rheological methods. For example, [16] uses dynamic light scattering to examine porcine gastric mucus. This technique requires a small sample volume (on the order of tens of picoliters) to be imbedded with small particles (109-nm polystyrene spheres are used in this example). The results show a pH dependent sol-gel transition and a so-called microviscosity that is 100-fold lower than the bulk viscosity. The authors attribute this dramatic viscosity difference to the probe particles being smaller than the pore size of the mucus gel.

A recent study of mucus systems by [2] reports a novel mechanical response for three mucus systems: porcine gastric mucus, purified mucin gels, and mucin-alginate gels. Specifically, the authors observe a frequency-dependent strain-hardening, as indicated by stress-sweep oscillatory rheology. The authors monitored strain-hardening by observing "stress/strain" for each cycle of oscillation. No clear definition of "stress/strain" is given in the article, so it can only be assumed that by "stress/strain" the authors mean τ_{max}/γ_{max}, the stress amplitude divided by the strain amplitude. The novel observation is that the ratio "stress/strain" increases while G^*, the complex

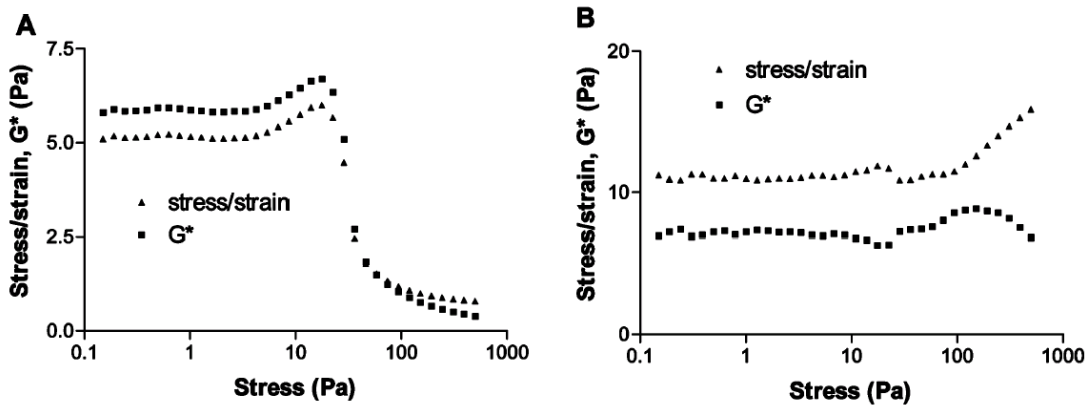

Figure 1-4: The frequency dependent stress hardening and flow of native pig gastric mucus, as reported by [2] (A) 0.2 Hz and (B) 1 Hz.

modulus, decreases. Figure 1-4 is an example of this novel observation for native pig gastric mucus. The authors interpret this as both strain-hardening and flow occurring simultaneously. This unique hardening behavior occurs gradually for each mucus system starting near 0.5 Hz. Frequencies above 1 Hz were not examined.

1.3.2 Invertebrate mucus

The first absolute measures of viscosity and elasticity of molluscan mucus were reported by [3]. Pedal mucus from the limpet *Patella vulgata* was examined by the means of creep tests under constant imposed shear stress. Mucus was collected from a large number of limpets and pooled together so that an adequate sample size was obtained. Figure 1-5 shows a typical creep test which exhibits a dominant elastic response. The initial creep compliance J_0 was used to determine the initial elastic modulus $G_0 = J_0^{-1} = 3 \times 10^3$ Pa. At long enough times a slow flow was observed with viscosity $\eta_0 \approx 2 \times 10^6$ Pa.s. These creep tests were performed in the linear regime under a constant applied stress $\tau_0 = 40$ Pa.

The role of pedal mucus in gastropod locomotion was elucidated by Denny [4, 6]. These experiments explored the nonlinear regime of pedal mucus rheology from the terrestrial pulmonate slug *Ariolimax columbianus*, commonly known as the banana slug. Denny observed a predominantly elastic response in the linear regime. Oscilla-

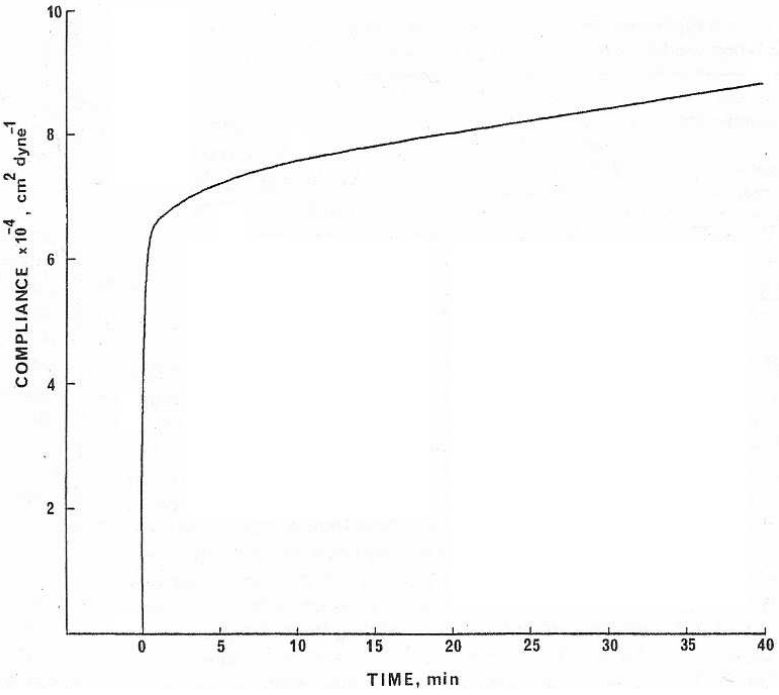

Figure 1-5: A typical creep curve for the pedal mucus of the limpet *Patella vulgata* as reported by [3].

tory rheology gave a linear elastic modulus $G' \approx 50$ Pa, and a loss modulus $G'' \approx 3$ Pa. However, after exceeding a critical strain $\gamma_{yield} \approx 5$ the pedal mucus flowed with a viscosity $\eta \approx 4$ Pa.s. Figure 1-6 shows the controlled-strain test used to observe the yield transition. The yield stress as reported by [4] is more commonly known as an overshoot stress. Figure 1-7 depicts how flow stress and overshoot stress depend on the imposed shear rate. For the limiting case when shear rate $\dot{\gamma} \rightarrow 0$, the overshoot stress may be interpreted in terms of a yield stress, as it is more commonly defined. Thus the yield stress $\tau_{yield} \approx 300$ Pa.

More recent studies of invertebrate pedal mucus, for example [17], have identified a difference between trail mucus and adhesive mucus. Adhesive mucus is used by some limpets and snails to form a strong bond to the substrate, in contrast to the trail mucus used for locomotion. These studies have not examined the comparative mechanical response of the different mucus, but have identified biochemical differences. In general, adhesive mucus tends to contain more protein with no significant difference in carbohydrate concentration.

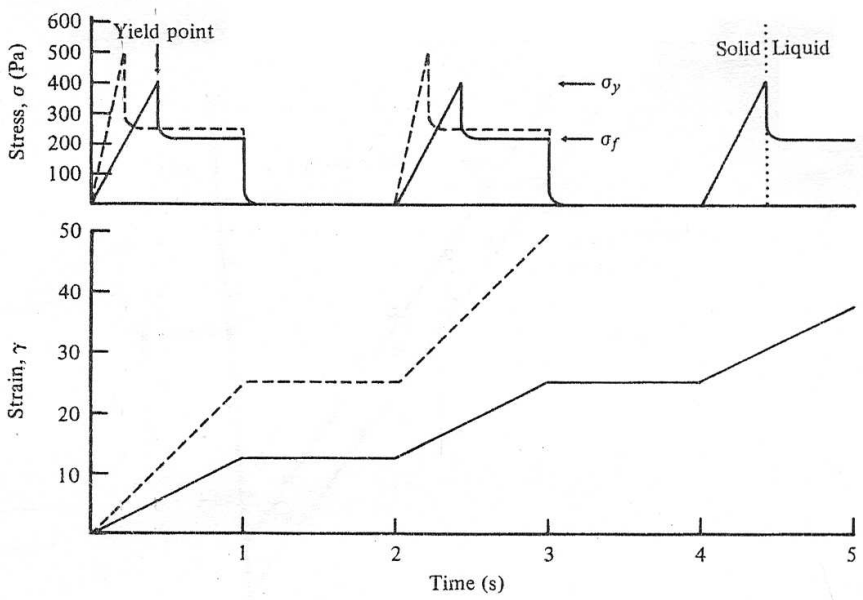

Figure 1-6: A typical strain-controlled test performed by [4] to show the transition to flow of the pedal mucus from the terrestrial slug *Ariolimax columbianus*.

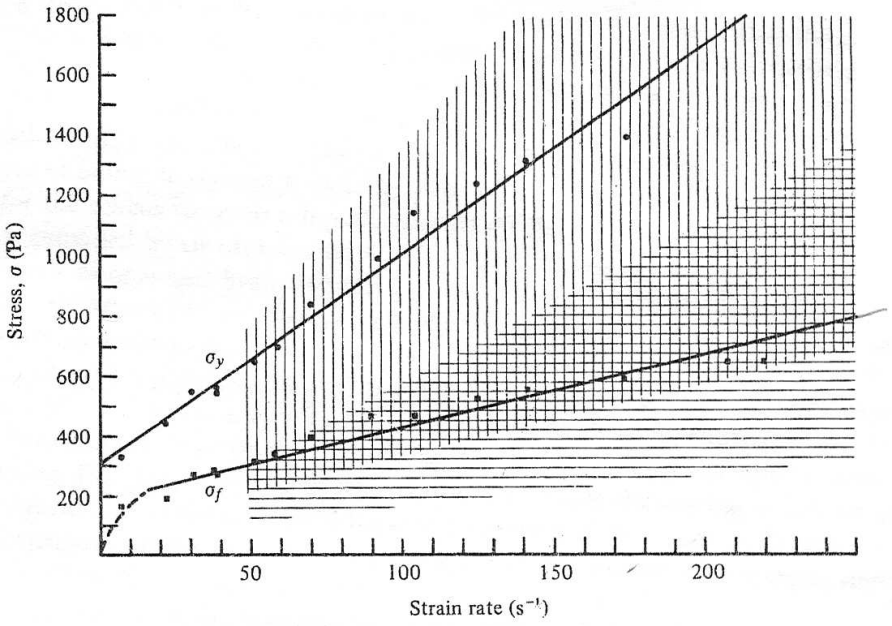

Figure 1-7: Overshoot stress σ_y and flow stress σ_f depend on the imposed shear rate for pedal mucus from the terrestrial slug *Ariolimax columbianus*, as reported by [4]. The data points are from a representative sample, and the ruled areas show the total range observed in all samples tested.

Chapter 2

Experimental Methods

Rheological measurements were performed with multiple instruments, including a stress-controlled CSL^2 500 rheometer, a stress-controlled AR1000-N rheometer, a stress-controlled AR-G2 rheometer, a strain-controlled ARES-LS rheometer (all TA Instruments, New Castle, DE), and the Flexure-based Microgap Rheometer (FMR) which is discussed in detail in Section 2.4.

Bulk rheology was examined with the AR1000-N, AR-G2, and ARES rheometers. Samples were tested between both plate-plate and cone-plate geometries. For plate-plate geometries, diameters ranged from 0.8cm to 4cm, and gaps ranged from 200μm to 1000μm. When necessary, adhesive-backed waterproof sandpaper (2000 grit, Eastwood Co., Pottstown, PA) was attached to the top and bottom plates to help avoid slip at the boundaries. All samples were tested at room temperature. Specific test details will be included with each set of results presented.

2.1 Materials

The terrestrial slug *Limax maximus* and terrestrial snail *Helix aspera* were collected from various places around Cambridge, MA. The animals were kept in a dry aquarium and fed a variety of foods such as lettuce, carrots, and mushrooms. A dish of water was in constant supply, and the aquarium was frequently sprayed with water to maintain a moist environment.

Pedal mucus was collected from *Limax maximus* and *Helix aspera* using the following protocol: A single animal was removed from the containment area, placed on a glass plate, and allowed to crawl toward a piece of food such as lettuce or a carrot. No mucus was collected until the gastropod had traveled a minimum of one body length so that no debris from the containment area remained in the sample, and to help ensure that locomotive mucus was present, rather than adhesive mucus which has been shown in some cases to have different composition and mechanical properties [17]. Deposited trail mucus was gathered by scraping with a razor blade behind the crawling organism until an adequate sample size was obtained. The sample was immediately deposited in a rheometer for testing.

2.2 Linear viscoelasticity and steady-flow rheology

The steady shear viscosity was determined by subjecting a sample to constant stress τ (or strain rate $\dot{\gamma}$) and waiting for $\dot{\gamma}$ (or τ) to reach steady state. At steady state the viscosity η was then calculated from the definition $\eta \equiv \tau/\dot{\gamma}$. After reaching steady state, a new stress (or strain rate) was then imposed to examine the non-Newtonian behavior of the material.

Creep tests were performed on the AR1000-N rheometer by subjecting the sample to a step input of shear stress τ_0, which is held constant until the end of the test. The strain response $\gamma(t)$ is recorded and the creep compliance $J(t)$ is calculated by the definition $J(t) \equiv \gamma(t)/\tau_0$.

Linear viscoelastic moduli G' (storage modulus) and G'' (loss modulus) were examined with small amplitude oscillatory shear (SAOS) tests. For a strain-controlled input (e.g. on the ARES rheometer) of

$$\gamma(t) = \gamma_0 sin(\omega t) \tag{2.1}$$

the linear response of the material will be a sinusoid at the same harmonic, shifted

by a phase angle δ,

$$\tau(t) = \tau_0 sin(\omega t + \delta). \tag{2.2}$$

This single harmonic response can be rewritten in terms of the viscoelastic moduli

$$\tau(t) = \gamma_0 |G^*(\omega)| sin(\omega t + \delta) \tag{2.3}$$

$$\tau(t) = \gamma_0 [G'(\omega) sin(\omega t) + G''(\omega) cos(\omega t)] \tag{2.4}$$

such that

$$G^{*2}(\omega) = G'^2(\omega) + G''^2(\omega) \tag{2.5}$$

$$G'(\omega) = \frac{\tau_0 cos\delta}{\gamma_0} \tag{2.6}$$

$$G''(\omega) = \frac{\tau_0 sin\delta}{\gamma_0} \tag{2.7}$$

in which G^* is the complex modulus, $G'(\omega)$ is the in-phase elastic component or "storage modulus" and $G''(\omega)$ is the out-of-phase viscous component or "loss modulus" of the response. It is important to note that by definition, the *linear* viscoelastic moduli are not a function of the strain input amplitude γ_0.

If the input is an oscillatory stress, instead of strain, then the output can be written as

$$\gamma(t) = \tau_0 |J^*(\omega)| sin(\omega t + \delta) \tag{2.8}$$

$$\gamma(t) = \tau_0 [J'(\omega) sin(\omega t) + J''(\omega) cos(\omega t)] \tag{2.9}$$

where J^* is the complex compliance, $J'(\omega)$ is the storage compliance and $J''(\omega)$ is the loss compliance. In the linear regime one can interrelate the moduli and compliances

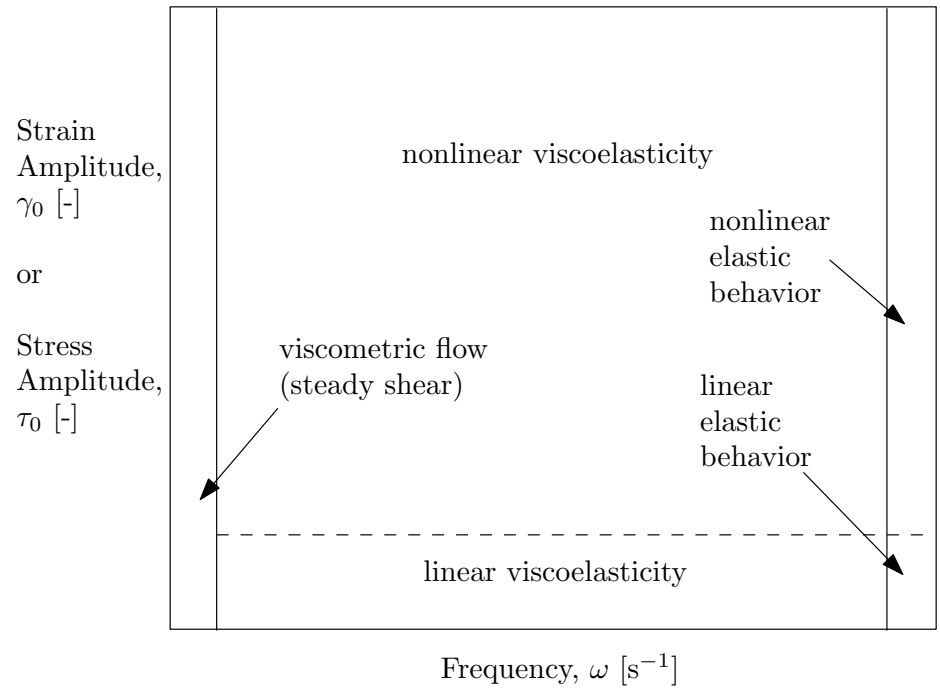

Figure 2-1: A Pipkin diagram maps the phase-space of linear and nonlinear material responses.

using the relationships [18]

$$|G^*||J^*| = 1 \tag{2.10}$$

$$G' = \frac{J'}{J'^2 + J''^2} \tag{2.11}$$

$$G'' = \frac{J''}{J'^2 + J''^2}. \tag{2.12}$$

2.3 Nonlinear oscillatory shear rheology

The response of a material to oscillatory shear is considered nonlinear if either of two things occur: 1) the viscoelastic moduli (G' or G'') depend on the input amplitude (γ_0 or τ_0) or 2) the response is not a sinusoid. These nonlinearities tend to appear as the input amplitude is increased beyond a critical point, and thus the nonlinear regime is typically referred to as large amplitude oscillatory shear (LAOS). It is convenient to draw a map which shows the various regimes of linear and nonlinear material behavior. Such a map is commonly referred to as a Pipkin diagram (see Figure 2-1),

which shows regimes of material behavior as a function of the strain amplitude γ_0 and frequency ω. The Pipkin diagram will be used later to map the phase-space in which experiments have been performed.

The first condition for nonlinearity, input amplitude dependence, will modify the material response so that

$$\tau(t) = \gamma_0[G'(\omega, \gamma_0)sin(\omega t) + G''(\omega, \gamma_0)cos(\omega t)]. \tag{2.13}$$

Although the response is nonlinear by definition, both G' and G'' are still well defined. In general, however, G' and G'' may not be well defined in the nonlinear regime, as will be shown in the following section.

2.3.1 Fourier transform rheology

If the second condition for nonlinearity appears, and the response is not a sinusoid, then G' and G'' are not defined as in the linear case. The material response can, in general, be written as a Fourier series to capture the higher harmonics in the response [19]

$$\tau(t) = \gamma_0 \sum_{\substack{n=1 \\ n \text{ odd}}}^{N} [G'_n(\omega, \gamma_0)sin(n\omega t) + G''_n(\omega, \gamma_0)cos(n\omega t)]. \tag{2.14}$$

Here n can only be odd due to the non-negativity of stored energy, as argued by [20]. A different framework must be developed to interpret the elastic and viscous components when higher harmonics are present. It has been shown [21] that the dissipation of energy depends on only one material function, G''_1. For a sinusoidal strain input, the energy dissipated per unit volume per cycle, E_d, is

$$E_d = \oint \tau d\gamma = \oint \tau(t)\dot{\gamma}(t)dt \tag{2.15}$$

$$= \gamma_0^2 \omega \int_0^{2\pi/\omega} \sum_{\substack{n=1 \\ n\text{odd}}}^{N} [G'_n sin(n\omega t) + G''_n cos(n\omega t)]cos(\omega t)dt \tag{2.16}$$

and due to the orthogonality of the trigonometric basis functions this reduces to

$$E_d = \gamma_0^2 \omega G_1'' \int_0^{2\pi/\omega} cos^2(\omega t) dt \tag{2.17}$$

$$E_d = \gamma_0^2 \pi G_1''. \tag{2.18}$$

Note that a similar result is achieved for the linear case when no higher harmonics are present, such that $G_1'' = G''$.

Although the dissipative nature of a material depends on only one material function, G_1'', the elastic nature of a material is more complicated. The storage of energy is related to all the remaining material functions. It has thus been proposed [21] to name G_1' the first harmonic modulus, G_2' and G_2'' the second harmonic moduli, G_3' and G_3'' the third harmonic moduli, and so on. Higher harmonics tend to decay away rapidly, which is a strength of Fourier transform rheology; typically only a few higher harmonics are needed to reconstruct the original signal.

It is complicated to understand the physical basis of the higher harmonic moduli, and this is a weakness of Fourier transform rheology. However, the higher harmonic moduli can serve as a sensitive rheological fingerprint for a material (e.g. [22]), and therefore can be used in quality control situations. The strengths and limitations of Fourier transform rheology have recently been reviewed by [23].

2.3.2 Lissajous curves

Another method of analyzing LAOS rheological data is to plot data in the form of a so-called Lissajous curve. In rheology a Lissajous curve is a parametric plot of stress $\tau(t)$ on the ordinate against strain $\gamma(t)$ (or strain rate $\dot{\gamma}(t)$) on the abscissa. The curve appears as an ellipse for a linear viscoelastic material. Figure 2-2 shows examples of linear viscoelastic Lissajous curves for various phase angles, normalizing

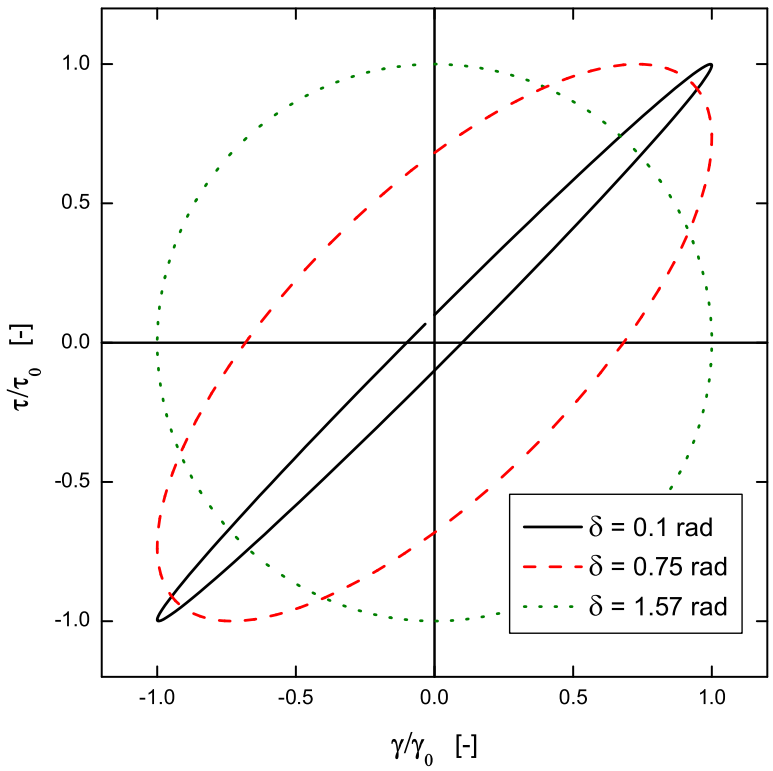

Figure 2-2: Normalized Lissajous curves of linear viscoelastic materials with varying phase angle δ.

the strain input and stress output of Equations 2.1 and 2.2 such that

$$x(t) = \frac{\gamma(t)}{\gamma_0} = sin(\omega t) \tag{2.19}$$

$$y(t) = \frac{\tau(t)}{\tau_0} = sin(\omega t + \delta). \tag{2.20}$$

A strongly elastic material will appear more like a straight line through the origin, whereas a viscous material will enclose more area. The enclosed area of a Lissajous curve, where τ is plotted against γ, is equal to the energy dissipated per unit volume per cycle E_d, as given by Equations 2.15 - 2.18.

A nonlinear, non-sinusoid material response will distort the ellipse. Thus a Lissajous curve, like Fourier transform rheology, can be used to indicate a deviation from

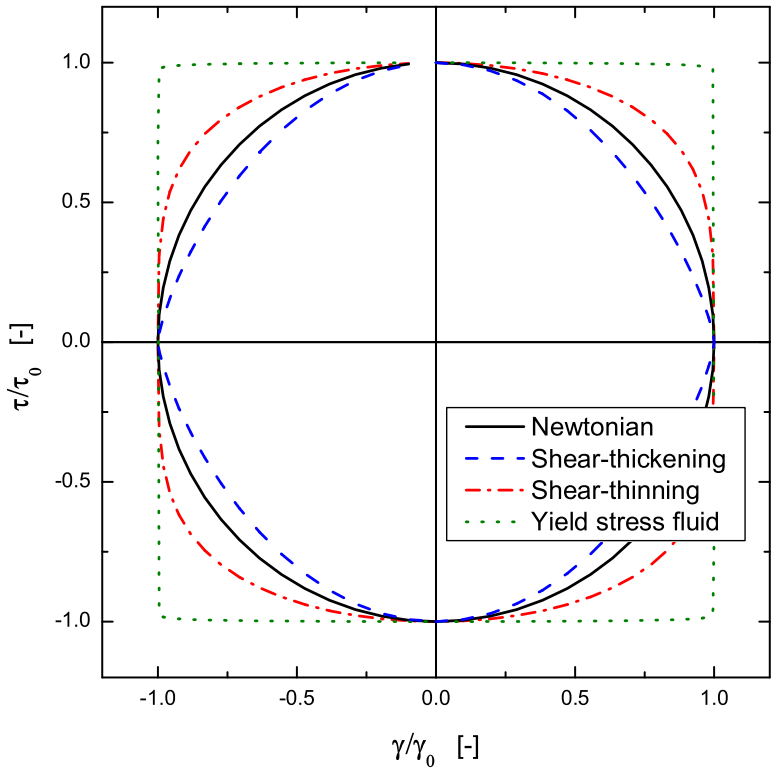

Figure 2-3: Normalized Lissajous curves of some nonlinear viscous fluids.

the linear viscoelastic regime. Distorted ellipses can take many forms. Figure 2-3 displays the Lissajous curves of some model nonlinear fluids, each obeying a variation of the power law

$$\tau = \kappa \dot{\gamma}^n. \tag{2.21}$$

Curves are shown for a Newtonian ($n = 1$), shear-thickening ($n = 1.5$), shear-thinning ($n = 0.5$), and a yield-stress-like fluid ($n = 0.01$).

Two basic examples of a nonlinear solid response are shown in Figure 2-4. Curves are shown for a linear, a strain-stiffening, and a strain-softening response. The elastic shear modulus, or tangent modulus, is equal to the slope of a Lissajous curve for a purely elastic material, $G = d\tau/d\gamma$. The examples in Figures 2-3 and 2-4 are

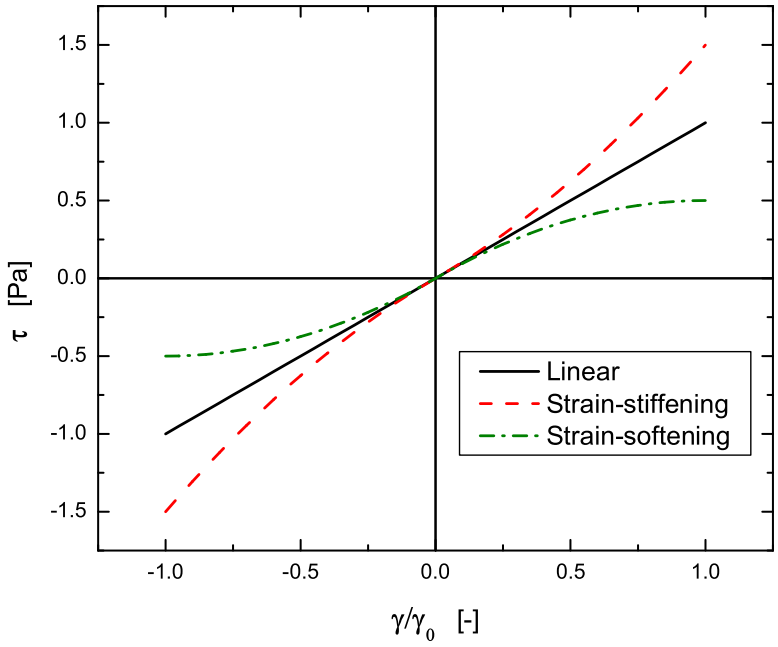

Figure 2-4: Sample Lissajous curves of some nonlinear purely-elastic solids.

the beginning of a framework for physically interpreting Lissajous curves of general nonlinear viscoelastic materials. This section has shown that the shape of a Lissajous curve depends on the type of material. It will also be shown (Section 2.4.4) that the shape of a Lissajous curve depends on the forcing function used. The examples given in this section consider a sinusoidal input (Equation 2.1). Section 2.4.4 will consider a triangle wave strain input.

2.3.3 Newly proposed quantitative measures for LAOS

Some quantitative material functions for describing LAOS rheology have been previously proposed. For example, [24] proposes three parameters for interpreting Lissajous curves which plot stress τ upon strain-rate $\dot{\gamma}$. The three parameters are an attempt to describe the dissipative, elastic, and nonlinear nature of the material. However, these three parameters, along with other previously suggested material functions, do not adequately describe the type of nonlinear response shown in the tests of pedal mucus,

as will be seen in Chapter 3. Thus, a new framework is proposed for interpreting LAOS results.

Four parameters are proposed to describe the elastic, viscous, and nonlinear characteristics of a material in LAOS. The dissipative nature of the material is completely captured by the loss modulus G_1'', since G_1'' is the only mode of viscous energy dissipation for a single harmonic input as shown in Section 2.3.1. Three other parameters are proposed to describe the elasticity and nonlinearity of the material.

Small strain elastic shear modulus, M

The elasticity and nonlinearity of a material are described by three parameters. First, the slope of the curve at zero strain, that is

$$M \equiv \left.\frac{d\tau}{d\gamma}\right|_{\gamma=0}. \tag{2.22}$$

This first measure of elasticity, M, can be interpreted as the small strain elastic modulus. That is, M is the elastic modulus at zero strain, and can be written in terms of the higher harmonic elastic moduli by referring to Equation 2.14. First note that

$$M = \left.\frac{d\tau}{d\gamma}\right|_{\gamma=0} = \left.\frac{d\tau}{dt}\frac{dt}{d\gamma}\right|_{\gamma=0}. \tag{2.23}$$

Then it is shown, from Equation 2.14, that

$$\frac{d\tau}{dt} = \gamma_0\omega \sum_{\substack{n=1 \\ n\text{odd}}}^{N} n[G_n'(\omega,\gamma_0)cos(n\omega t) - G_n''(\omega,\gamma_0)sin(n\omega t)]. \tag{2.24}$$

Substituting $t = 0$ and π/ω gives

$$\left.\frac{d\tau}{dt}\right|_{\gamma=0} = \gamma_0\omega(\pm 1) \sum_{\substack{n=1 \\ n\text{ odd}}}^{N} nG_n'(\omega,\gamma_0) \tag{2.25}$$

since, for an input of $\gamma(t) = \gamma_0 sin(\omega t)$, $\gamma = 0$ when $t = 0$ and $t = \pi/\omega$, and the ± 1 term corresponds to each of those times, respectively. Additionally we have

$$\left.\frac{d\gamma}{dt}\right|_{\gamma=0} = \gamma_0\omega(\pm 1). \tag{2.26}$$

Thus we conclude that

$$M(\omega, \gamma_0) = \sum_{\substack{n=1 \\ n \text{ odd}}}^{N} nG'_n(\omega, \gamma_0). \tag{2.27}$$

It is then apparent that M reduces to G' in the linear regime, that is

$$\lim_{\gamma_0 \to 0} M(\omega) = G'(\omega). \tag{2.28}$$

Large strain elastic shear modulus, L

The second measure of elasticity, L, is defined as the stress at maximum strain divided by the maximum strain, that is

$$L \equiv \frac{\tau|_{\gamma=\pm\gamma_0}}{\pm\gamma_0}. \tag{2.29}$$

Thus L serves as some measure of the large strain elastic modulus, that is, the shear modulus at maximum strain $\gamma = \gamma_0$. This second measure of elasticity can also be represented in terms of the higher harmonic elastic moduli. From Equation 2.14

$$\frac{\tau}{\gamma_0} = \sum_{\substack{n=1 \\ n\text{odd}}}^{N} [G'_n(\omega, \gamma_0) sin(n\omega t) + G''_n(\omega, \gamma_0) cos(n\omega t)] \tag{2.30}$$

and substituting $t = \pi/2\omega$ and $3\pi/2\omega$ gives

$$L(\omega, \gamma_0) = \frac{\tau|_{\gamma=\pm\gamma_0}}{\pm\gamma_0} = \sum_{\substack{n=1 \\ n\text{odd}}}^{N} G'_n(\omega, \gamma_0) \tag{2.31}$$

since $\gamma = \pm\gamma_0$ when $t = \pi/2\omega$ and $3\pi/2\omega$. It is thus shown that L also reduces to G' in the linear regime, that is

$$\lim_{\gamma_0 \to 0} L(\omega) = G'(\omega). \tag{2.32}$$

Elastic stiffening ratio, L/M

Comparing the material functions L and M is a way to compare large strain and small strain elasticity. This comparison will be referred to as the elastic stiffening ratio S, given by

$$S(\omega, \gamma_0) \equiv \frac{L(\omega, \gamma_0)}{M(\omega, \gamma_0)}. \tag{2.33}$$

If $S > 1$ then the material strain-stiffens, and is in some way analogous to the strain-stiffening solid in Figure 2-4. Likewise, if $S < 1$ the material is strain-softening. The elastic stiffening ratio then serves as a measure of nonlinearity. Since M and L both reduce to G' in the linear regime, a linear viscoelastic material will have $S = 1$, as given by Equations 2.28 and 2.32. The fact that $S = 1$ in the linear regime can also be seen graphically in Figure 2-2 which shows Lissajous curves for linear viscoelastic materials. Note that for a Newtonian fluid $M = 0$ and $L = 0$, which causes S to be undefined. However, in the *limit* of a Newtonian fluid as the phase angle δ approaches $\pi/2$,

$$\lim_{\delta \to \pi/2} S = 1 \tag{2.34}$$

as it does for all linear viscoelastic materials.

Figure 2-5 shows schematically the definitions of M, L, and S for an arbitrary nonlinear viscoelastic material. It is important to note that the current definitions and linear viscoelastic limits of the quantitative measures M, L, and S are only valid for a sinusoidal input (e.g. Equation 2.1). Section 2.4 will discuss LAOS quantifiers for a triangle wave strain input.

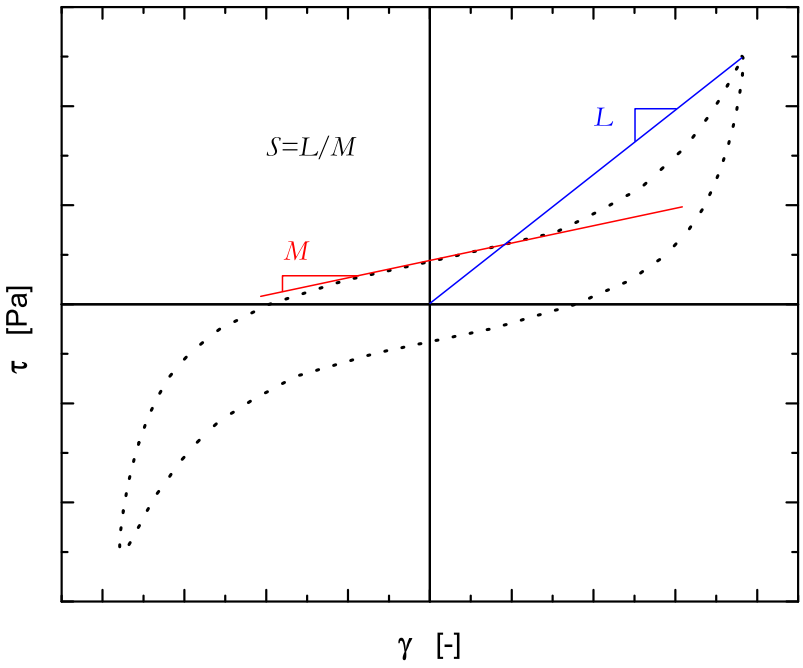

Figure 2-5: Schematic definitions for elastic material functions of a nonlinear viscoelastic material; M: small strain elastic shear modulus; L: large strain elastic shear modulus; $S = L/M$: elastic stiffening ratio.

2.4 Microgap rheology

Gastropod pedal mucus secretions were also examined with microgap rheology using the Flexure-based Microgap Rheometer (FMR) [25]. Microgap rheology is distinct from bulk rheology in that gap sizes can be as small as 1μm, whereas bulk rheology is typically limited to gaps larger than 50μm. Microgap rheology offers two distinct benefits for testing gastropod pedal mucus. First, smaller sample sizes are required, which is important for many biological samples. Second, microgap rheology is able to test pedal mucus at its biologically relevant thickness, which under a crawling slug has been measured in the range of 10-20 μm [6].

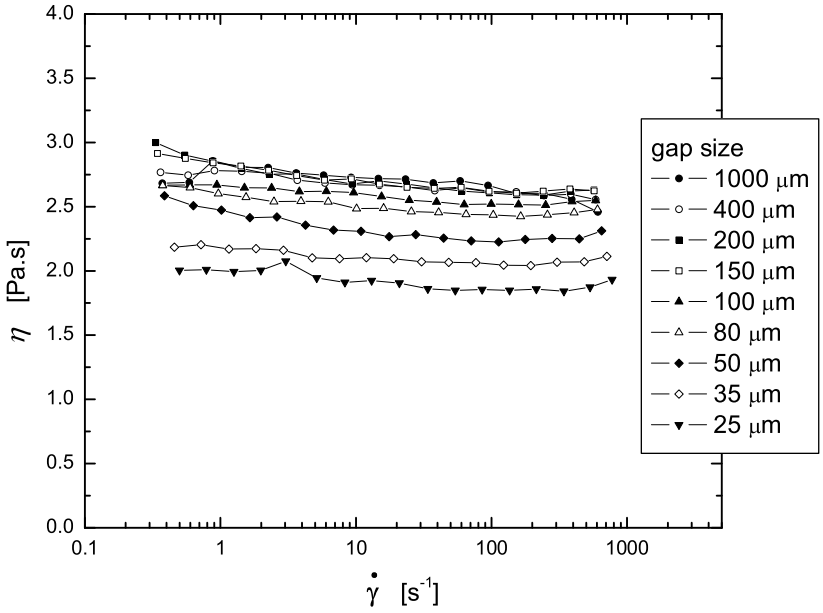

Figure 2-6: Apparent bulk viscosity of a Newtonian oil deviates due to errors at decreasing gap sizes (AR1000, 4cm plate, 20°C).

2.4.1 Gap limits of bulk and microgap rheology

As an example of the minimum gap achievable with bulk rheology, Figure 2-6 displays the apparent viscosity of a Newtonian oil (N1000, $\eta(20°C) = 2.867$ Pa.s, Cannon Instrument Co., State College, PA) at various gap separations. The test was performed on the stress-controlled AR1000 rheometer with a 4cm plate at 20°C. Results start to deviate at a gap of 100μm, and continue to deviate at smaller gaps. Smaller gaps magnify errors such as nonparallelism, nonconcentricity, and nonflatness of plates. A significant error may also be due to a miscalculation of zero gap, due to the squeeze flow of air between parallel plates resulting in a high normal force before the plates actually touch [26].

The maximum attainable gap for a bulk rheometer is determined by a balance of surface tension helping the sample to bridge the gap and gravity pulling the sample

downward. Surface tension will hold a fluid sample in the gap with a force

$$F_\sigma \cong \sigma cos\theta 2\pi r \tag{2.35}$$

where σ is surface tension, θ is the contact angle, and r is the radius of the plate. Gravity, in the form of hydrostatic pressure, fights to flow the material out of the gap with a force

$$F_g \cong \frac{1}{2}\rho g h^2 2\pi r \tag{2.36}$$

where ρ is the fluid density, g is the gravitational acceleration, and h is the gap height. The ratio of gravity to surface tension forces is captured by the Bond number,

$$Bo \equiv \frac{F_g}{F_\sigma} = \frac{\rho g h^2}{\sigma} \tag{2.37}$$

where the numerical coefficients have been discarded. Surface tension dominates so long as $Bo < 1$, thus one might expect the maximum gap to occur when $Bo \approx 1$, giving

$$h_{\max} \approx \sqrt{\frac{\sigma}{\rho g}}. \tag{2.38}$$

For water $h_{\max} \approx 3$ mm, giving an approximate upper bound for the maximum gap height for testing liquids in a rheometer.

The experimental limits of a typical bulk rheometer and the FMR are shown graphically in Figure 2-7. For the FMR, viscosity is calculated from (see Section 2.4.2)

$$\eta = \frac{\tau}{\dot{\gamma}} = \frac{\tau}{V/h} \tag{2.39}$$

where τ is the measured shear stress, V is the velocity of the sliding plate, and h is the gap height between the plates. The limits of measuring the stress τ, imposing a velocity V, and maintaining a gap h are shown in Table 2.1. The boundaries shown

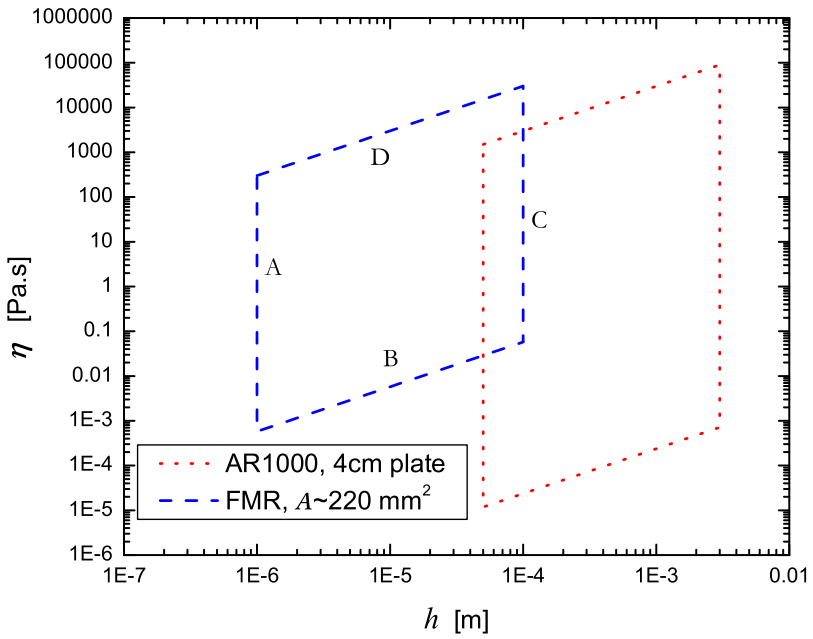

Figure 2-7: Experimental limits of a typical bulk rheometer (AR1000, 4cm plate) and the Flexure-based Microgap Rheometer.

in Figure 2-7 for the FMR are calculated as

$$\text{A)}\ \ \eta = \frac{\tau h_{min}}{V} \tag{2.40}$$

$$\text{B)}\ \ \eta = \frac{\tau_{min} h}{V_{max}} \tag{2.41}$$

$$\text{C)}\ \ \eta = \frac{\tau h_{max}}{V} \tag{2.42}$$

$$\text{D)}\ \ \eta = \frac{\tau_{max} h}{V_{min}} \tag{2.43}$$

where τ, V, and h vary from their minimum to maximum values.

2.4.2 FMR working principles

The FMR is a strain-controlled rheometer that tests a sample in planar Couette flow. A front view schematic of the FMR is shown in Figure 2-8. The sample is held in the area between the two black plates. The inchworm motor actuates the lower compound

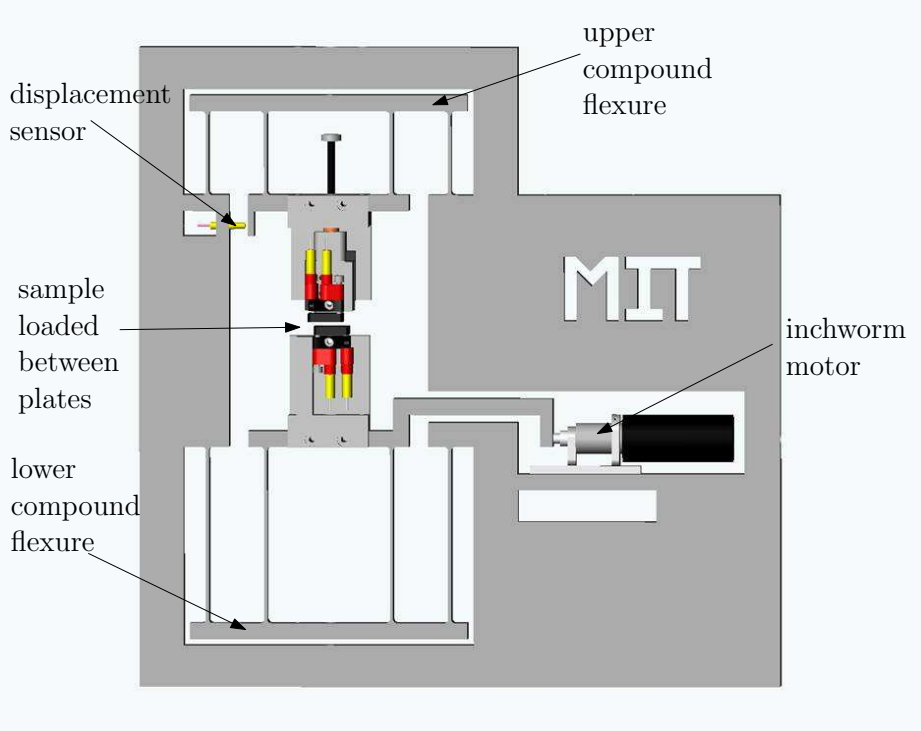

Figure 2-8: A schematic view of the Flexure-based Microgap Rheometer (image courtesy of Dr. Christian Clasen).

flexure, which imposes a simple shear deformation on the sample. The rate of strain depends on the velocity of actuation V and the gap height h,

$$\dot{\gamma} = \frac{V}{h}. \tag{2.44}$$

The top flexure responds to the shear stress transferred through the sample, and its displacement is measured with an inductive proximity sensor. The stress in the material is then calculated from the displacement of the upper flexure Δx, the spring constant of the upper flexure ($k = 8.2 \times 10^4 \mathrm{N/m}$), and the area of the top confining plate A ($A = 217.3$ mm^2 and $A = 20.1$ mm^2 are both available),

$$\tau = \frac{k\Delta x}{A}. \tag{2.45}$$

The compound flexures serve the purpose of maintaining a constant gap height while the sample is being sheared. Compound flexures significantly reduce displace-

	minimum	maximum
V (m/s)	5×10^{-5}	2×10^{-3}
h (m)	1×10^{-6}	1×10^{-4}
Δx (m)	3×10^{-9}	4×10^{-5}
$\dot{\gamma}$ (s^{-1})	0.5	2000
F (N)	2.5×10^{-4}	3.28
τ (Pa)	1.1	1.6×10^{5}

Table 2.1: Experimental limitations of the Flexure-based Microgap Rheometer.

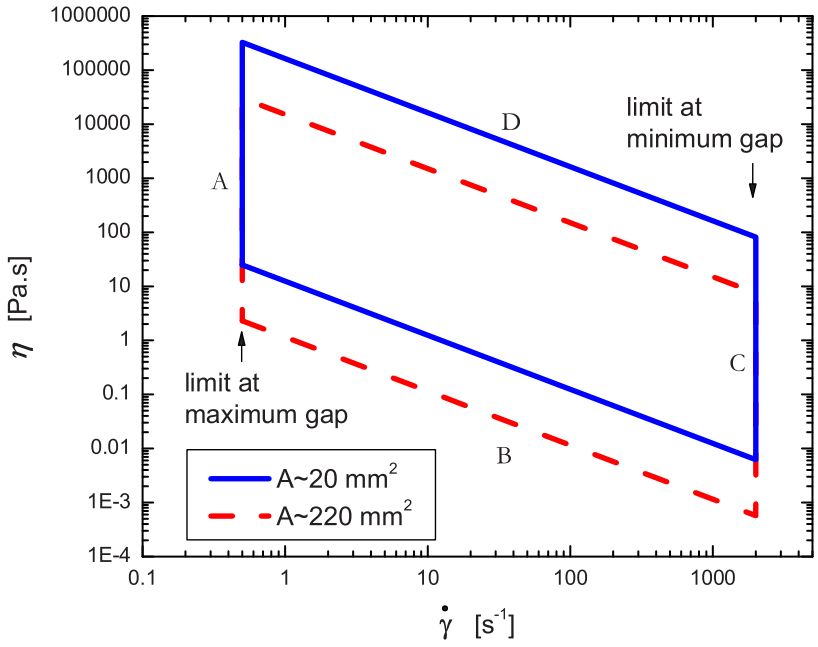

Figure 2-9: Experimental limits of the Flexure-based Microgap Rheometer.

ment perpendicular to the direction of motion of the top and bottom plates. The plates must be transparent, because the absolute gap height is measured with white light interferometry. Visible light is directed through the semi-reflective transparent plates and the gap, which creates a fringe pattern upon exiting. The fringe spacing is used to determine the absolute spacing of the gap h.

2.4.3 FMR experimental range

The experimental range of the FMR is fundamentally limited by three parameters as seen from Equations 2.44 and 2.45: the actuation velocity V, the gap height h, and the displacement of the force-sensing upper flexure Δx. Table 2.1 displays the limits of these fundamental parameters in addition to the consequential limits of derived parameters: the shear rate $\dot{\gamma}$, the force measured with the upper flexure F, and the resulting shear stress τ. The minimum and maximum values of τ depend on the choice of plate area A; Table 2.1 gives the minimum and maximum values possible assuming that both geometries can be used.

The experimentally accessible range for a steady-state flow viscosity test on the FMR can be determined from Table 2.1. The experimental range is shown graphically in Figure 2-9, where the boundary lines $A - D$ are calculated from

$$\text{A)}\ \ \eta = \frac{F}{A}\frac{h_{max}}{V_{min}} \tag{2.46}$$

$$\text{B)}\ \ \eta = \frac{F_{min}}{A}\frac{h}{V} \tag{2.47}$$

$$\text{C)}\ \ \eta = \frac{F}{A}\frac{h_{min}}{V_{max}} \tag{2.48}$$

$$\text{D)}\ \ \eta = \frac{F_{max}}{A}\frac{h}{V} \tag{2.49}$$

where F, h, and V vary from their minimum to maximum values. The experimental range of shear-rate $\dot{\gamma}$ depends on the gap height, and thus the limits shown in Figure 2-9 are on a sliding scale. The absolute limits at maximum and minimum gap height h are labeled to reinforce this point.

2.4.4 Theoretical models of LAOS rheology on the FMR

Oscillatory shear rheology on the FMR is distinct from typical oscillation rheology because the strain input is a triangle wave, rather than a sinusoid. The actuating motor is programmed to drive forward or backward at a constant speed, thus creating the strain input shown in Figure 2-10. Since the strain input is not a simple sinusoid,

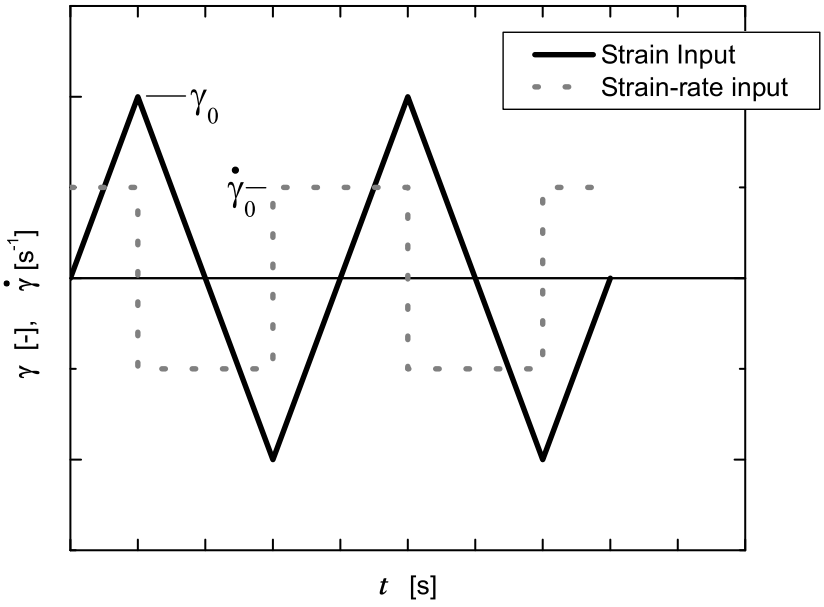

Figure 2-10: Controlled strain input for FMR is a triangle wave.

the typical G' and G'' framework (Equations 2.1 - 2.7) for describing viscoelastic models does not readily apply. The response of some model materials will be examined in this section.

Figure 2-11 shows two typical ways to model linear viscoelastic materials. The Maxwell model consists of a spring (modulus G) in series with a damper (damping coefficient η). The Maxwell model represents a viscoelastic *fluid*, since a constant applied stress will cause a steady state flow. In the limit that G approaches infinity,

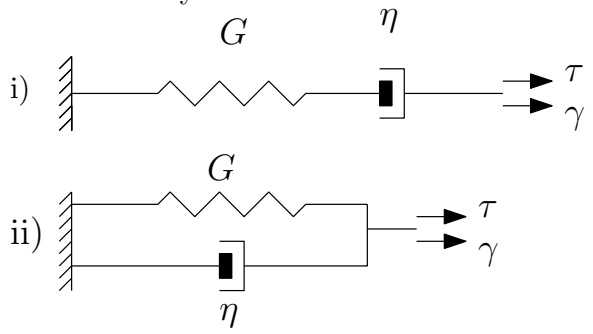

Figure 2-11: Schematics of i) Maxwell model for a viscoelastic fluid and ii) Kelvin model for a viscoelastic solid.

the Maxwell model represents a Newtonian fluid.

The Kelvin model consists of a spring (modulus G) in parallel with a viscous damper (damping coefficient η). The Kelvin model represents a viscoelastic *solid*, since an applied stress will result ultimately in a steady state strain. For the limiting case where η approaches zero the Kelvin model represents a purely elastic solid.

The governing equation for the linear Maxwell model is

$$\dot{\tau} + \frac{G}{\eta}\tau = G\dot{\gamma}. \tag{2.50}$$

The characteristic time of the Maxwell model λ is given by $\lambda = \eta/G$. Equation 2.50 is a first order non-homogeneous differential equation which can be solved via the technique of an integrating factor. The forcing function is a square wave, which will be represented as

$$\dot{\gamma}(t) = \dot{\gamma}_0[1 - 2H(t-a) + 2H(t-3a) - 2H(t-5a) + ...] \tag{2.51}$$

where $H(t-a)$ represents a Heaviside step function occurring at $t = a$. The steady state solution for stress $\tau(t)$ is then given by

$$\begin{aligned}\tau(t) = \eta\dot{\gamma}_0[(1 - e^{-t/\lambda}) - 2(1 - e^{-(t-a)/\lambda})H(t-a) \\ + 2(1 - e^{-(t-3a)/\lambda})H(t-3a) - ...].\end{aligned} \tag{2.52}$$

Equation 2.52 can be rendered dimensionless by introducing a non-dimensional stress

$$\tau^* = \frac{\tau}{\eta\dot{\gamma}_0}. \tag{2.53}$$

Additionally, a non-dimensional time may be introduced as

$$t^* = \frac{t}{t_{cycle}/2} = \frac{t}{2\gamma_0/\dot{\gamma}}. \tag{2.54}$$

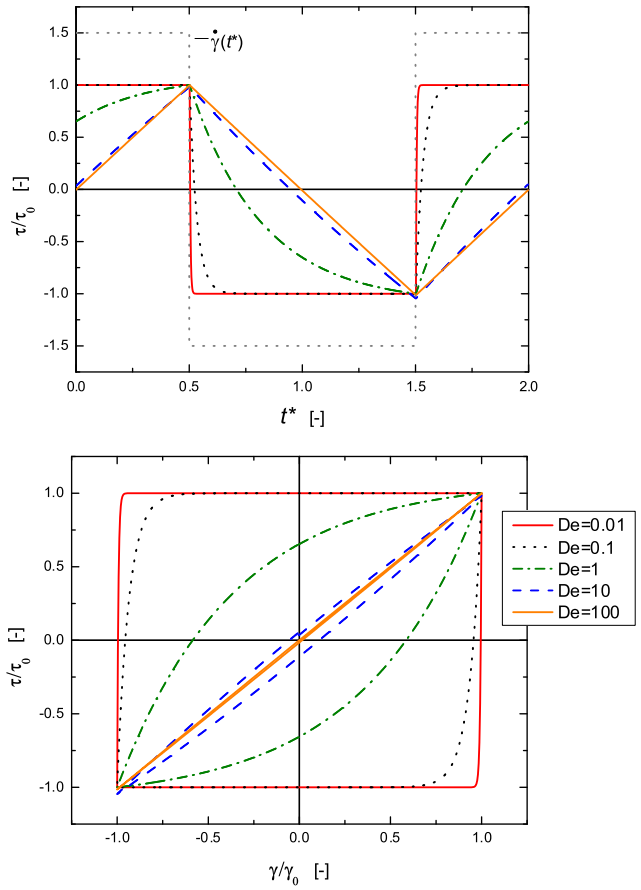

Figure 2-12: Steady-state Maxwell model response to triangle wave strain input.

Finally, the non-dimensional Deborah number is given by

$$\mathrm{De} = \frac{\text{material timescale}}{\text{experimental timescale}} = \frac{\lambda}{2\gamma_0/\dot{\gamma}}. \tag{2.55}$$

The Deborah number is a ratio of the material timescale λ divided by the experimental timescale $2\gamma_0/\dot{\gamma}$. Small Deborah numbers represent a situation where the the experimental timescale is much longer than the material timescale, and thus the

viscoelastic fluid can achieve steady state flow. Conversely, a high Deborah number represents a more solid-like response. Equation 2.52 is then rewritten in dimensionless form as

$$\tau^*(t) = (1 - e^{-t^*/\mathrm{De}}) - 2(1 - e^{-(t^*-a^*)/\mathrm{De}})H(t^* - a^*) + 2(1 - e^{-(t^*-3a^*)/\mathrm{De}})H(t^* - 3a^*) - ... \tag{2.56}$$

The dependence of the material behavior on the experimental timescale is shown schematically in the Pipkin diagram of Figure 2-1. Lissajous curves of the Maxwell model response on the FMR are shown in Figure 2-12. Note that the limiting case $\mathrm{De} \rightarrow 0$ represents the response of a Newtonian fluid. The Lissajous curves of Figure 2-12 are distinct from the curves of Figure 2-2, even though the material is linear viscoelastic in each case. For example, in the limit of a Newtonian fluid, the Lissajous curve is a circle for a sinusoidal input (Equation 2.1 and Figure 2-2), but the curve is a square for a triangle wave strain input (Figure 2-10 and 2-12).

The governing equation for the Kelvin model is

$$\tau = G\gamma + \eta\dot{\gamma} \tag{2.57}$$

where G is the shear modulus and η is the viscosity of the elements shown in the Kelvin model of Figure 2-11. The characteristic time of the Kelvin model λ is given by $\lambda = \eta/G$. A convenient way to explore the parameter space of a Kelvin model is to hold G constant while increasing η starting from $\eta = 0$, as shown in Figure 2-13, which plots the Lissajous curves expected for the Kelvin model subjected to a triangle wave strain input. The axes are *not* normalized in this plot to show two distinct features of the Kelvin model response to a triangle wave strain input. First, the slope is equal to the elastic shear modulus

$$\frac{d\tau}{d\gamma} = G \tag{2.58}$$

which is independent of all other parameters (η, $\dot{\gamma}_0$, and γ_0). Second, the zero-strain

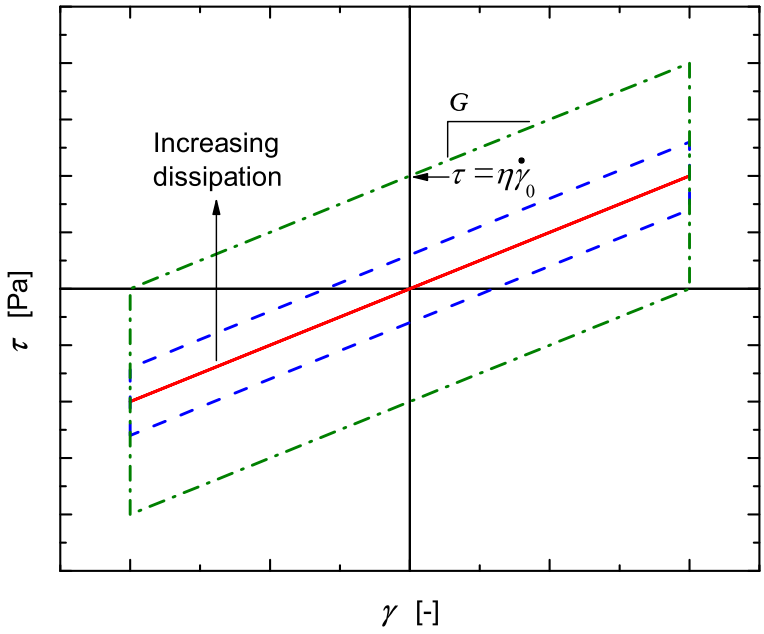

Figure 2-13: Kelvin model response to triangle wave strain input.

intercept is due entirely to viscous stresses

$$\tau|_{\gamma=0} = \eta\dot{\gamma}_0. \tag{2.59}$$

Note that for a purely solid material ($\eta = 0$) no area is enclosed in the Lissajous curve, and thus no energy is dissipated.

The proposed quantitative measures for LAOS (Section 2.3.3) only apply for a sinusoidal input such as Equation 2.1. Thus M, L, and S can not, in general, be applied to the Lissajous curves produced by the FMR. However, a measure of nonlinear elasticity can still be quantified if the material has solid-like qualities. Specifically for a Kelvin model, the slope of the Lissajous curve is always equal to the shear modulus, as given by Equation 2.58 (in general, with a triangle wave strain input, at large De the slope is approximately equal to the shear modulus). The shear modulus at maximum strain $G(\gamma = \gamma_0)$ can be compared to the shear modulus at zero strain $G(\gamma = 0)$ to quantify the stiffening or weakening of a Kelvin material. Thus, an

elastic stiffening ratio for a Kelvin model on the FMR can be written as

$$S_{\text{FMR}} = \frac{G(\gamma = \gamma_0)}{G(\gamma = 0)}. \tag{2.60}$$

The Maxwell and Kelvin models are only the simplest descriptions of a linear viscoelastic fluid and solid. Although many other linear viscoelastic (and non-linear viscoelastic) responses are possible, the examples of this section provide a framework for analyzing results from the Flexure-based Microgap Rheometer that are presented in Section 3.3.

Chapter 3

Results and Discussion: Rheology of Pedal Mucus from Terrestrial Gastropods

This chapter presents results from examining pedal mucus using the rheological characterization methods discussed in Chapter 2. First, results from traditional rheology are presented, including flow, creep, and linear oscillation tests. The nonlinear mechanical response of pedal mucus is discussed in Section 3.2, in which Fourier transform rheology, Lissajous curves, and the new quantitative measures (introduced in Section 2.3.3) are used to characterize pedal mucus. Microgap rheology is used to examine pedal mucus at physically relevant length scales. Finally, the Pipkin space (introduced in Figure 2-1) is used as a framework for mapping the linear and nonlinear response of pedal mucus.

3.1 Traditional rheology

The steady-state flow viscosity of pedal mucus from the garden snail *Helix aspera* is shown in Figure 3-1, as measured in a controlled stress rheometer. It is apparent that pedal mucus is extremely non-Newtonian. At stresses below 300 Pa the viscosity is of the order $10^3 - 10^4$ Pa.s, but decreases by several orders of magnitude at a critical

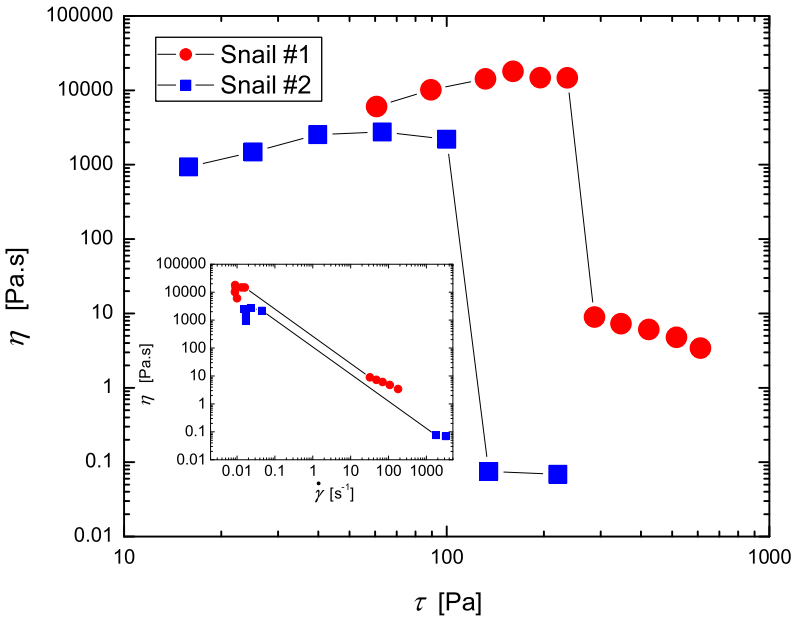

Figure 3-1: Steady state flow viscosity of native pedal mucus collected from two snails *Helix aspera* (D=0.8 cm plate with sandpaper, 20°C, Snail#1 on CSL^2 500, 100μm gap; Snail#2 on AR1000, 50μm gap).

stress near $100 - 250$ Pa. Below this critical stress, pedal mucus is almost solid-like, as compared to higher stresses when the material flows with a dramatically lower viscosity. Since flow exists at any finite stress, pedal mucus does not exhibit a *true* yield stress. However, this behavior may be described as an *apparent* yield stress, since the flow at low applied stresses may be difficult to measure, and it is followed by a dramatic drop in viscosity over a narrow range of stress. The critical stress at which viscosity dramatically changes will henceforth be referred to as the yield stress τ_y [27, 28].

After exceeding the yield stress the steady shear viscosity η decreases with increasing stress τ. Thus pedal mucus exhibits shear-thinning above τ_y. The yield stress τ_y and post-yield viscosity values are similar to those reported by [4] for pedal mucus from the banana slug *Ariolimax columbianus*. However, [4] does not explicitly report a finite viscosity below τ_y.

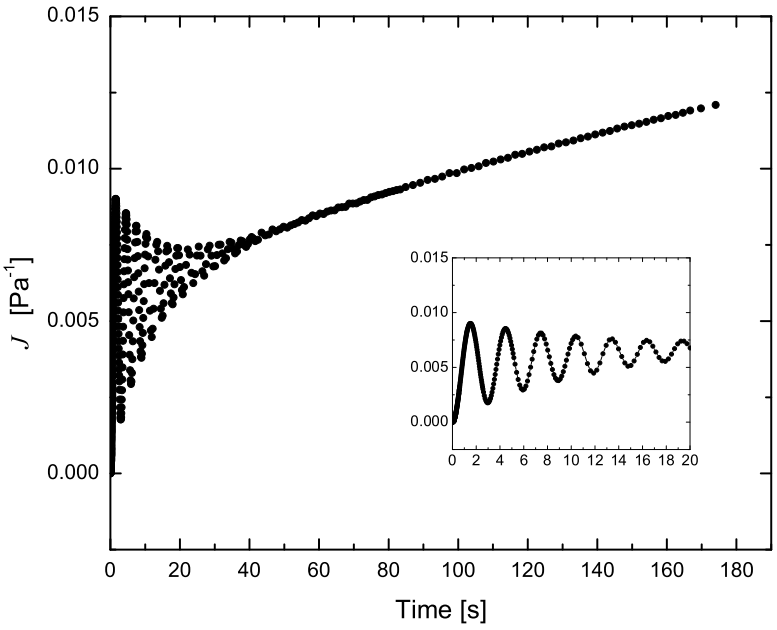

Figure 3-2: Creep compliance of native pedal mucus from the terrestrial snail *Helix aspera* (AR-G2, D=0.8 cm plate with sandpaper, 1000μm gap, 22°C, $\tau_0 = 5$ Pa $< \tau_y$).

Pedal mucus from the garden snail *Helix aspera* was also tested under creep conditions of constant applied stress. Results from one such creep test are shown in Figure 3-2. Pedal mucus initially shows a dominant elastic response, followed by a small amount of flow as indicated by the slope of the compliance curve. At sufficiently long times the slope of the compliance curve approaches a constant. The rate of change of compliance with time is exactly equal to the inverse of viscosity, that is $dJ(t)/dt = \eta^{-1}$. At steady state $dJ(t)/dt = 2.96 \times 10^{-5}$ Pa^{-1}.s^{-1}, which corresponds to a viscosity $\eta = 3.4 \times 10^4$ Pa.s. This matches well with the large finite viscosity below the yield stress, as shown in Figure 3-1.

At short times a damped inertio-elastic ringing can be seen, which is the result of the moment of inertia of the rotating fixture and draw rod of the torsional rheometer in series with the elastic response of the material. If the moment of inertia of the fixture is known, then the storage modulus G' and loss modulus G'' can be determined at the free oscillation ringing frequency [29]. This will be discussed further at the end

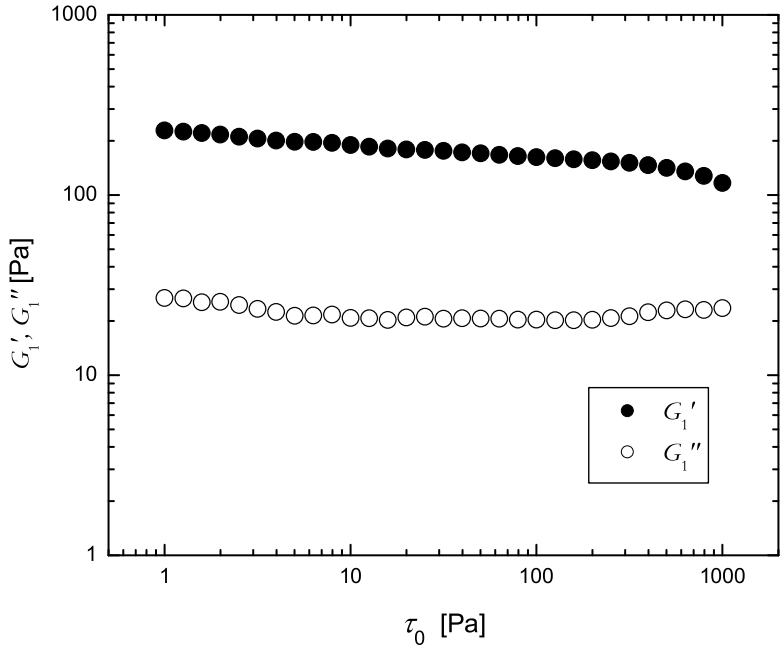

Figure 3-3: Oscillatory stress sweep of native pedal mucus from the terrestrial slug *Limax maximus* (AR1000, 2cm plate with sandpaper, solvent trap, 200μm gap, 22°C, $\omega = 1$ rad.s^{-1}).

of this subsection, in order to compare with the results obtained from oscillatory testing.

The linear viscoelastic moduli, G' and G'', were examined at multiple frequencies within the linear regime using small amplitude oscillatory shear (SAOS), as described in Section 2.2. All oscillatory tests were performed on pedal mucus from the terrestrial slug *Limax maximus*. The linear regime was first identified by performing an oscillatory stress sweep at a constant frequency $\omega = 1$ rad.s^{-1}, as shown in Figure 3-3. Note that although the instrument reports G' and G'', this information is interpreted here as G_1' and G_1'', to emphasize that higher harmonics may exist in the non-linear regime. As discussed in Section 2.3 the linear viscoelastic regime is defined to be the region in which G' and G'' are independent of the oscillation stress τ_0 and the strain response is a single harmonic sinusoid. The first condition seems to be weakly satisfied for most of the stress range examined. It is noteworthy that higher stresses

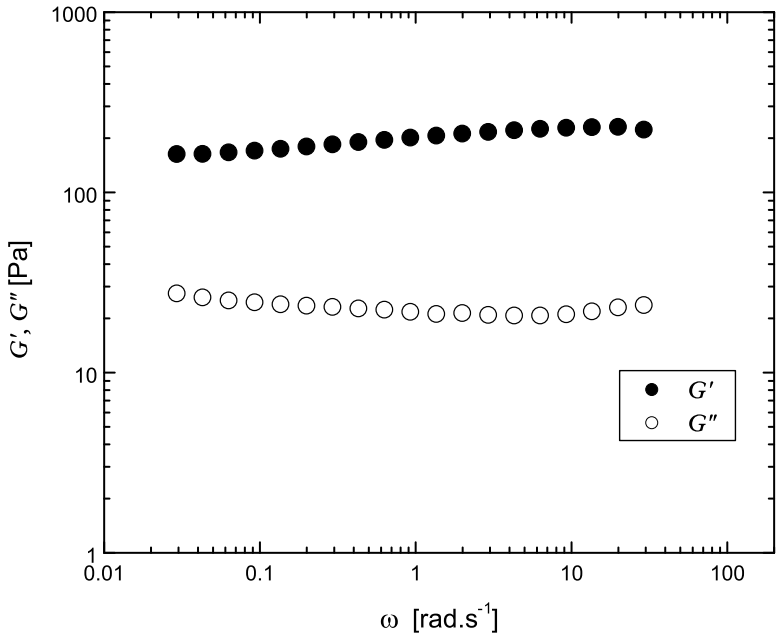

Figure 3-4: Oscillatory frequency sweep of native pedal mucus from the terrestrial slug *Limax maximus* (AR1000, 2cm plate with sandpaper, solvent trap, 200μm gap, 25°C, $\tau_0 = 5$ Pa$< \tau_y$).

($\tau_0 > 1000$ Pa) could not be explored because the sample yielded and was quickly thrown out of the gap. The second requirement for linearity, a single harmonic response, will be discussed in the following section (Section 3.2) where it will be shown that $|G_3^*| << |G_1^*|$ for $\tau_0 < 30$ Pa (Figure 3-8). An oscillating stress with amplitude $\tau_0 = 5$ Pa (which corresponds to $\tau_0 << \tau_y$) was chosen for a frequency sweep in the linear regime (Figure 3-4). It is observed that both G' and G'' are weak functions of frequency in the linear regime. This is typical behavior for a viscoelastic solid, although it may be speculated that at low enough frequencies the material would exhibit more dissipation, since a finite steady state flow was observed in the creep test of Figure 3-2.

It is interesting to examine the similarity in pedal mucus from *Helix aspera* (Figures 3-1 and 3-2) and *Limax maximus* (Figures 3-3 and 3-4). To do this, the viscoelastic moduli, G' and G'', of pedal mucus from *Helix aspera* must be extracted

from the inertio-elastic ringing of the creep experiment (Figure 3-2) [29].

For a torsional spring-mass-damper system, the equation of motion can be written as

$$I\ddot{\theta} = T_0 - T_R. \tag{3.1}$$

where θ is the angular rotation of the fixture, I is the moment of inertia of the system, T_0 is the applied torque, and T_R is the torque resistance of the material. In a torsional rheometer the torque resistance T_R is related to the shear stress τ by

$$T_R = \int_0^R \tau 2\pi r^2 dr \tag{3.2}$$

where R is the radius of the geometry. The shear stress τ is related to the shear strain γ and strain-rate $\dot{\gamma}$ by an appropriate constitutive model. The Kelvin model for a viscoelastic solid (introduced in Figure 2-11) is initially chosen. The Kelvin model was given by Equation 2.57, but is repeated here for convenience

$$\tau = G\gamma + \eta\dot{\gamma}. \tag{3.3}$$

For the experiment of Figure 3-2 a parallel plate geometry was used, in which case γ depends on the radial location within the sample as

$$\gamma = \frac{r\theta}{h} \tag{3.4}$$

where h is equal to the gap height. Equations 3.3 and 3.4 can be substituted into Equation 3.2 to relate T_R and θ for a parallel plate geometry, resulting in

$$T_R = F(G\theta + \eta\dot{\theta}). \tag{3.5}$$

$$F = \frac{\pi R^4}{2h} \tag{3.6}$$

where F is given for a parallel plate geometry. The radial displacement can be scaled

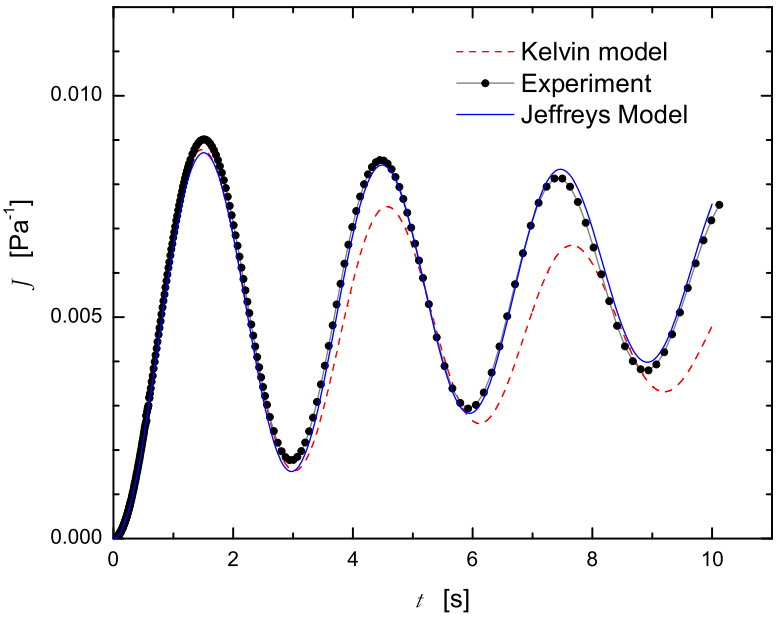

Figure 3-5: Kelvin and Jeffreys models fit to inertio-elastic ringing during creep test of native pedal mucus from the terrestrial snail *Helix aspera* (AR-G2, D=0.8 cm plate with sandpaper, 1000μm gap, 22°C, $\tau_0 = 5$ Pa $< \tau_y$).

by the elastic nature of the material such that

$$\theta^* \equiv \frac{\theta}{\theta|_{t\to\infty}} = \frac{\theta FG}{T_0} \tag{3.7}$$

where $\theta|_{t\to\infty}$ is the steady state result when $T_0 = T_R$. Equations 3.5–3.7 can now be directly substituted into Equation 3.1, which results in a second-order non-homogeneous differential equation for the radial displacement θ^*, where the applied torque is a step function $T_0 = T_0 H(t)$

$$\frac{I}{FG}\ddot{\theta}^* + \frac{\eta}{G}\dot{\theta}^* + \theta^* = H(t). \tag{3.8}$$

The equation above is that of a classical spring-mass-damper system. Ringing

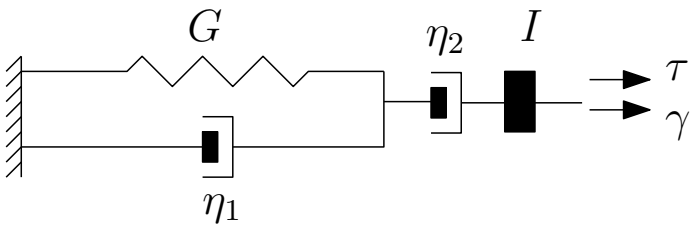

Figure 3-6: Jeffreys model for a viscoelastic fluid in series with the moment of inertia of the rheometer; if η_2 is not included a Kelvin model is retained.

occurs only with an under-damped system, with the solution given by

$$\theta^* = \left\{1 - e^{-\frac{\eta F}{2I}t}\left[cos(\omega t) - \frac{\eta F}{2I\omega}sin(\omega t)\right]\right\} \tag{3.9}$$

$$\omega = \sqrt{\frac{GF}{I} - \left(\frac{\eta F}{2I}\right)^2}. \tag{3.10}$$

The two Kelvin model parameters are fit to the first ten seconds of the data. Figure 3-5 shows the result of the fit to the data originally shown in Figure 3-2, and Table 3.1 gives the fitting parameters. Note that compliance $J(t)$ is related to angular displacement as

$$J(t) \equiv \frac{\gamma(t)}{\tau_0} = \frac{\theta^*(t)}{G}. \tag{3.11}$$

The Kelvin model is unable to capture steady-state flow at long times, due to the parallel spring element. Since steady-state flow is observed in pedal mucus, a three-parameter model was used to see if an additional parameter can accurately capture this behavior.

A Jeffreys model is equivalent to a Kelvin model (parameters G, η_1) in series with a viscous damper (parameter η_2), as shown in Figure 3-6. Note that the steady-state flow viscosity $\eta = \eta_2$. Furthermore, two time constants may be defined as

$$\lambda_1 = \eta_1/G \tag{3.12}$$

$$\lambda_2 = \eta_2/G \tag{3.13}$$

	Kelvin	Jeffreys	SAOS (Figure 3-4)
G (Pa)	210	224	n/a
η_1 (Pa.s)	12.7	5.94	n/a
η_2 (Pa.s)	n/a	5.26×10^3	n/a
λ_1 (s)	0.061	0.027	n/a
λ_2 (s)	n/a	23	n/a
ω (rad.s^{-1})	2.03	2.11	1.99
G' (Pa)	210	223	211
G'' (Pa)	25.9	17.0	21.4

Table 3.1: Fitting parameters for creep ringing experiment with pedal mucus from *Helix aspera* (Small amplitude oscillatory shear (SAOS) test included for reference, which was performed on pedal mucus from *Limax maximus*).

where λ_1 is the relaxation time and λ_2 is the retardation time. In a similar way to the previous development with the Kelvin model, a second order differential equation may be constructed to describe the motion of the system [29]. Figure 3-5 shows the resulting fit of the Jeffreys model to the creep data from Figure 3-2; the fitting parameters are given in Table 3.1.

The addition of a third parameter, corresponding to a steady viscous flow element, dramatically improves the fit to the data. The steady-state flow viscosity $\eta_2 = 5.26 \times 10^3$ Pa.s compares well with the steady-state flow results of Figure 3-1 ($\tau_0 < \tau_y$), which is interesting because the value of η_2 is determined by only the first ten seconds of the creep test, whereas each data point in Figure 3-1 may take more than 120 s to reach steady state.

Table 3.1 gives the fitting parameters of the Kelvin and Jeffreys models, along with the resulting G' and G'' which can be found after the model parameters are known. Table 3.1 also includes the results of testing pedal mucus from *Limax maximus* in oscillatory shear. The comparison is remarkably similar, with $G' \approx 200$ Pa for pedal mucus from both creatures. Furthermore, the loss moduli are also similar, $G'' \approx 20$ Pa, for both creatures, which is about one order of magnitude less than the storage modulus. This corresponds to $\tan\delta = G''/G' \approx 0.1$, which is a comparative measure of the significance of dissipative to elastic effects in the material.

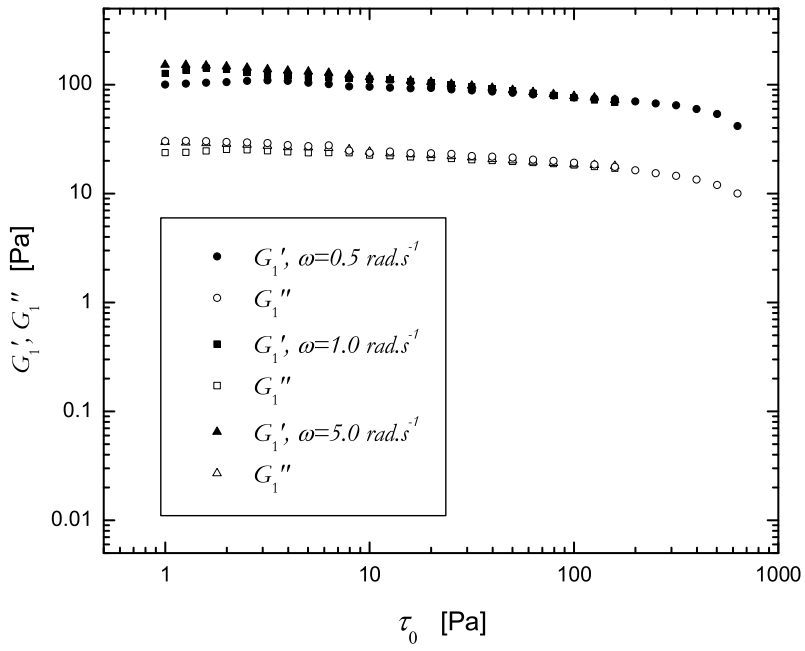

Figure 3-7: Oscillatory stress sweep of native pedal mucus from the terrestrial slug *Limax maximus* (AR1000, 2cm plate with sandpaper, solvent trap, 180μm gap, 22°C). Note these results are for a different sample than Figures 3-3 and 3-4.

3.2 Nonlinear LAOS rheology

A crawling slug subjects pedal mucus to shear stress above the yield stress, and thus the nonlinear viscoelastic properties of native slime are relevant in adhesive locomotion. The shear stress exerted by a crawling slug can exceed 2000 Pa, as measured by Denny [30]. Furthermore, the strain amplitude under a crawling slug can be estimated from the speed versus time profile reported by Denny [30]. Using this data, and assuming the pedal mucus thickness to be 10-20 μm, a maximum strain $\gamma \approx 10^3$ is imposed on the pedal mucus with each pulsatile wave.

3.2.1 Viscoelastic moduli

An oscillatory stress sweep of pedal mucus from *Limax maximus* is shown in Figure 3-7, in which a stress sweep was performed at multiple frequencies. Pedal mucus

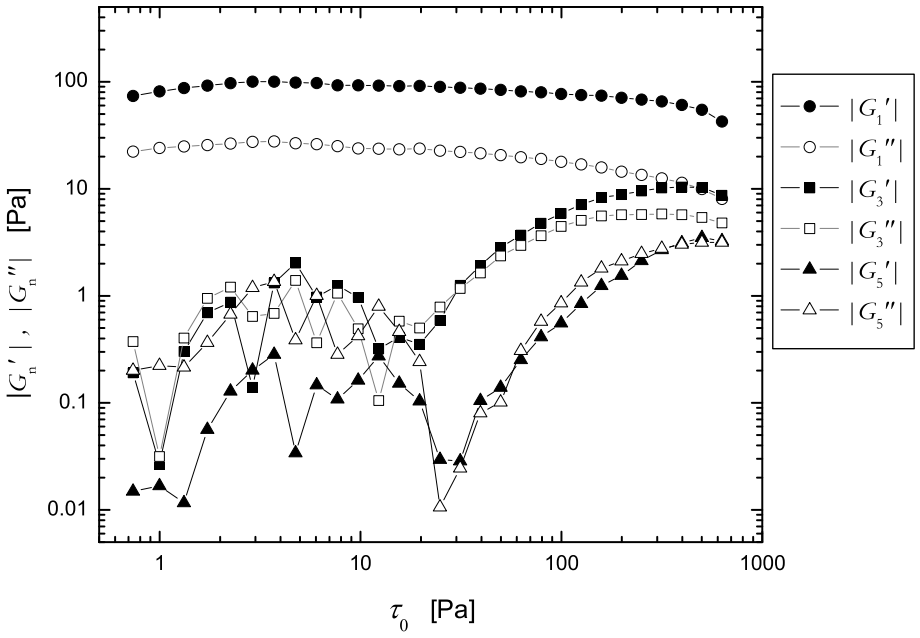

Figure 3-8: Higher harmonic moduli for an oscillatory stress sweep of native pedal mucus ($\omega = 0.5$ rad.s^{-1}).

undergoes a transition at a critical stress beyond which the elastic response dramatically decreases. However, no quantitative data could be collected for native slime beyond this critical stress since the material was ejected from the gap. The critical stress amplitude for this transition is slightly larger than the yield stress in steady flow tests, where $\tau_{y,flow} \approx 100 - 250$ Pa, and the maximum oscillatory shear stress $\tau_{0,crit} \approx 800 - 1000$ Pa.

Figure 3-7 distinctly reports only the first harmonic moduli, G_1' and G_1'', as a function of oscillation stress τ_0 (see Equation 2.14 which defines the Fourier series decomposition). It may appear that the material is linear over most of the stress range probed, since G_1' and G_1'' are nearly independent of τ_0. However, the second criteria for linear behavior, a single harmonic response, is not satisfied over the entire stress range, as will be shown in the following section.

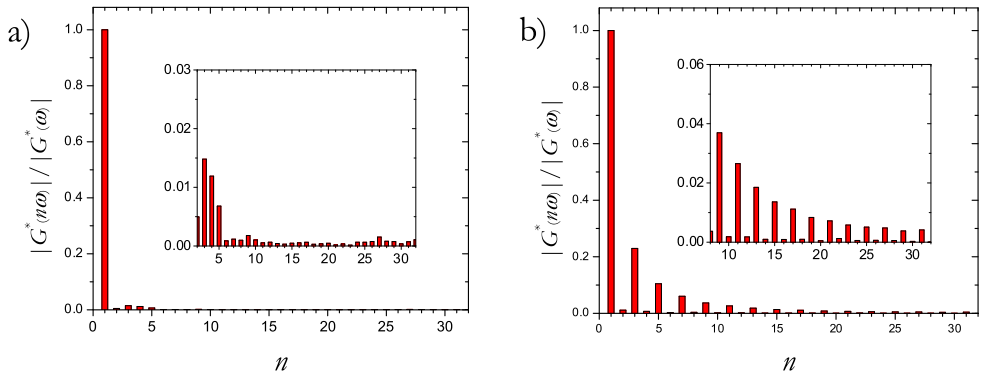

Figure 3-9: Normalized intensity of Fourier coefficients for oscillatory data points in the linear and nonlinear regime; a) $\tau_0 = 2.3$ Pa, and b) $\tau_0 = 630$ Pa.

3.2.2 Fourier transform rheology

The stress sweep at $\omega = 0.5$ rad.s^{-1} shown in Figure 3-7 was analyzed with a discrete fourier transform (Matlab) in order to calculate the higher harmonic contributions to the complex modulus. Figure 3-8 shows the higher harmonic moduli, $|G'_n|$ and $|G''_n|$, as a function of τ_0 for pedal mucus from *Limax maximus*. At low stresses ($\tau_0 < 30$ Pa) the magnitudes of the higher harmonic moduli are no more than 1% of G'_1, and show no clear variation with stress amplitude, indicating the linear regime where higher harmonics are negligible. Above $\tau_0 = 30$ Pa the higher harmonic moduli monotonically increase and the sample response is nonlinear. Note that the higher harmonics appear even though G'_1 and G''_1 seem to be independent of τ_0.

A wider range of the Fourier spectrum is shown in Figure 3-9 for a point in the linear regime at low stress and for a point in the nonlinear regime at high stress. The plots show the intensity of each frequency, scaled by the intensity of the fundamental frequency.

The linear regime is completely dominated by the fundamental harmonic. The next strongest harmonic ($3\omega_1$) is only 1.5% as strong as the fundamental. This is in the range of the background noise of the signal, since the even harmonic $4\omega_1$ is also

1.5% as strong as the fundamental and, as mentioned in Section 2.3.1, even harmonics are not physical.

The nonlinear regime is dominated by the fundamental harmonic, but the other odd harmonics are no longer negligible. The third harmonic $3\omega_1$ is more than 20% as strong as the fundamental. Note that even harmonics are almost zero, though due to noise in the original data signal they have a finite value.

The higher harmonics in an oscillatory shear experiment can be a very sensitive indicator for identifying the linear and nonlinear regimes of a given material response, but their physical interpretation is difficult. As mentioned in Section 2.3.1, for a sinusoidal input signal G_1'' is the only mode with a simple interpretation and represents viscous energy dissipation, but all higher harmonic moduli components are able to store energy. The extent of physical interpretation for the data in Figure 3-8 is that as τ_0 is increased the viscous nature of the material, as indicated by G_1'', decreases. At the same time the material seems to become more nonlinearly elastic in nature, since all modes of energy storage increase as τ_0 increases.

3.2.3 Lissajous curves

Native pedal mucus exhibits a strongly nonlinear response leading up to yield, as evidenced by the Fourier transform analysis of Section 3.2.2. In addition to Fourier transform rheology, the nonlinear behavior can be examined with Lissajous curves, as described in Section 2.3.2. The three oscillatory stress sweeps of Figure 3-7 have been plotted as Lissajous curves in Figures 3-10 to 3-12.

Figure 3-10 shows Lissajous curves at progressively increasing stress at a fixed frequency $\omega = 5$ rad.s^{-1}. At low stress the curves appear elliptical, because the sample is responding as a linear viscoelastic material. The elliptical curves become increasingly distorted as the oscillatory stress amplitude τ_0 is increased. At large strains the curves appear to turn upward like a strain-stiffening material (similar to the example in Figure 2-4). At the highest stresses explored for $\omega = 5$rad.s^{-1}, the loops appear to cross over themselves. This may be a true response of the material, but may also be due to the competition between inertia of the instrument and the

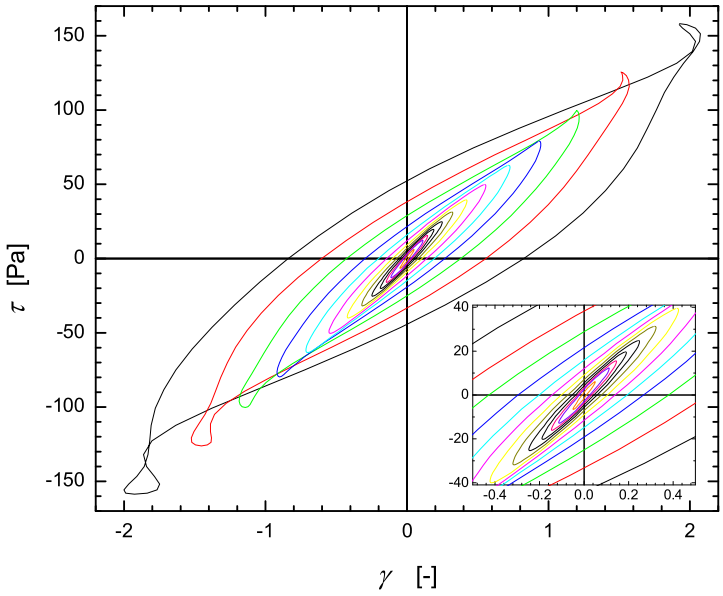

Figure 3-10: Lissajous curves for an oscillatory stress sweep of pedal mucus from *Limax maximus* ($\omega = 5.0$ rad.s^{-1}).

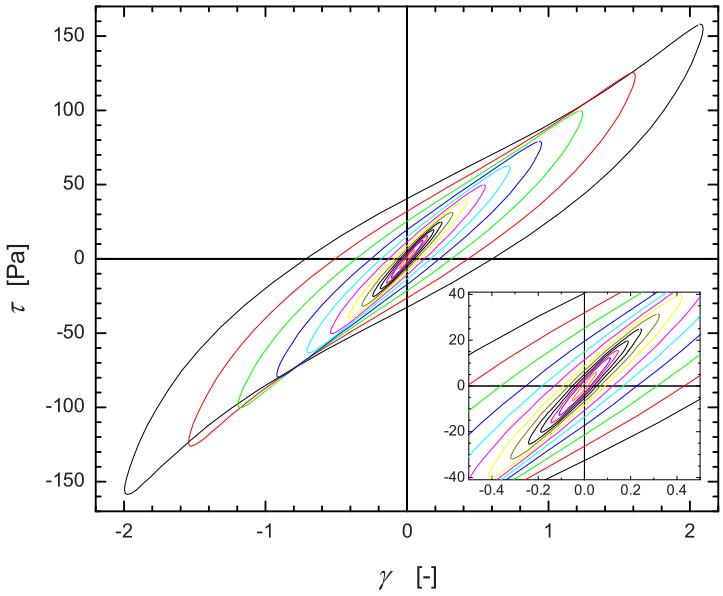

Figure 3-11: Lissajous curves for an oscillatory stress sweep of pedal mucus from *Limax maximus* ($\omega = 1.0$ rad.s^{-1})

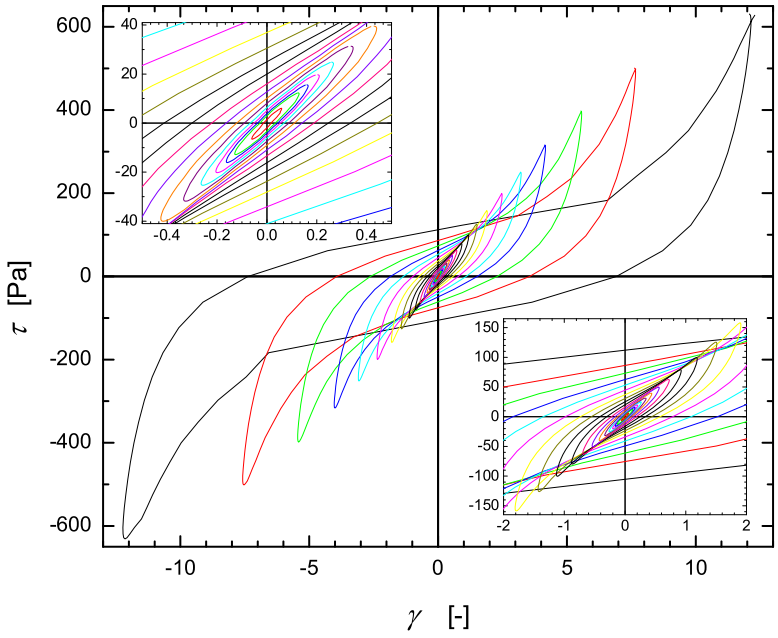

Figure 3-12: Lissajous curves for an oscillatory stress sweep of pedal mucus from *Limax maximus* ($\omega = 0.5$ rad.s^{-1}).

elasticity of the sample, since the test is performed by imposing an oscillatory stress, not strain. As we saw in Section 3.1 this can lead to overshoots in free-oscillations.

Lissajous curves for pedal mucus at $\omega = 1$ rad.s^{-1} are shown in Figure 3-11. The mucus again shows a linear response at low stress amplitudes, as indicated by the elliptical shape of the curves. As the stress amplitude is increased the curves distort. At large strains the curves again turn upward, and are reminiscent of a strain-stiffening material. Unlike the curves for $\omega = 5$ rad.s^{-1}, no overlapping is observed in the curves at $\omega = 1$ rad.s^{-1}.

The oscillatory stress sweep at $\omega = 0.5$ rad.s^{-1} explored higher stress amplitudes than the other two tests. Figure 3-12 shows Lissajous curves for oscillatory tests of pedal mucus at $\omega = 0.5$ rad.s^{-1}. Again, the curves appear elliptical in the linear regime, but become progressively distorted as τ_0 is increased. The curves are distorted in a similar way to the data shown in previous figures; at large strains the stress turns up, indicating a type of strain-stiffening behavior. This trend becomes

more pronounced as the yield stress is approached. The nonlinear elasticity at each frequency will be quantified in the following section, as outlined in Section 2.3.3. It is significant to note that this nonlinear response is not captured by monitoring G_1', which is shown in Figure 3-7 to be nearly constant even into the non-linear regime. Furthermore, the physical interpretation could not be elucidated with Fourier transform rheology by monitoring the coefficients of higher harmonics.

3.2.4 Quantitative measure of stiffening

The Lissajous curves presented in Figures 3-10 to 3-12 appear to indicate the material is strain stiffening, but this apparent stiffening has not yet been quantified. This section will apply the newly proposed quantitative measures of LAOS (Section 2.3.3) to the pedal mucus results initially presented in Figure 3-7.

First, the small-strain elastic shear modulus M was calculated at each stress amplitude τ_0, and is shown in Figure 3-13. This measure of elasticity should reduce to G_1' in the linear regime, as proven in Section 2.3.3. This appears to be the case if we compare Figure 3-13 to Figure 3-7, since $M \approx G_1'$ for low stresses. At high stress M deviates from G_1', dropping down to $M \approx 10$ Pa just before yield, whereas $G_1' \approx 40$ Pa just before yield. The decrease in M is apparent from the Lissajous curves by recalling that M is defined as the slope $d\tau/d\gamma$ when $\gamma = 0$. For example, in Figure 3-12 this slope progressively decreases as τ_0 increases.

The small-strain elastic shear modulus M decreases with increasing τ_0 as the bulk yield stress is approached. This decrease in elasticity can be interpreted partial yielding. Some network components that contribute to elasticity are weakened or broken, but the sample is not fully yielded. In fact, network components that contribute to large strain elasticity are still intact, as will be seen by analyzing L, the large strain elastic shear modulus.

The large strain elastic shear modulus L was calculated as a function of τ_0 (Figure 3-14). This measure also reduces to G_1' in the linear regime, which can be seen by comparing the small stress results of Figure 3-14 to Figure 3-7. The large strain modulus is approximately equal to G_1' even at large stress. At the highest stress

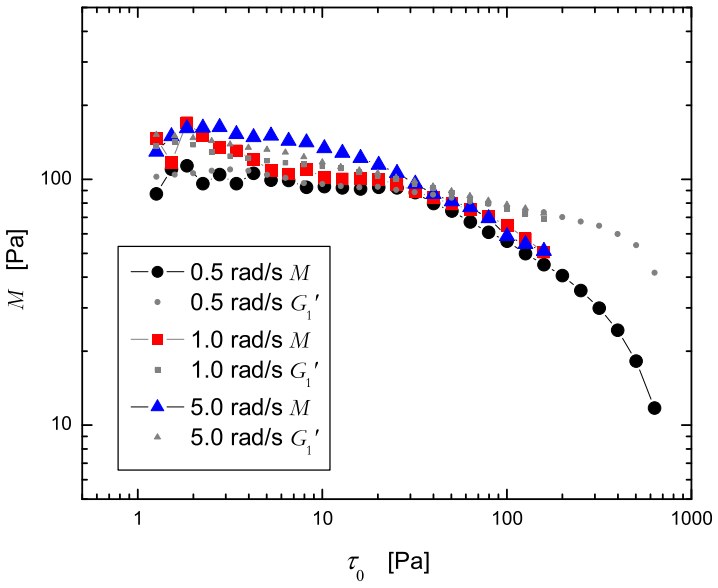

Figure 3-13: Small strain elastic modulus, M, for an oscillatory stress sweep of pedal mucus at various frequencies, G_1' data from Figure 3-7.

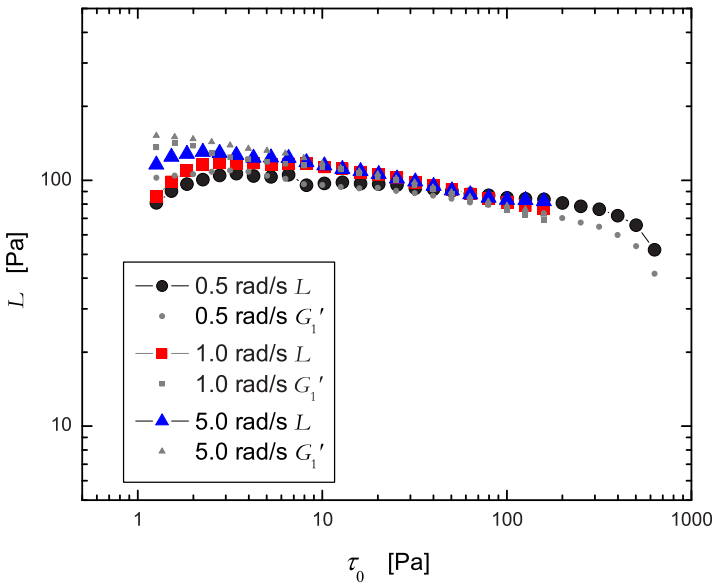

Figure 3-14: Large strain elastic modulus, L, for an oscillatory stress sweep of pedal mucus at various frequencies, G_1' data from Figure 3-7.

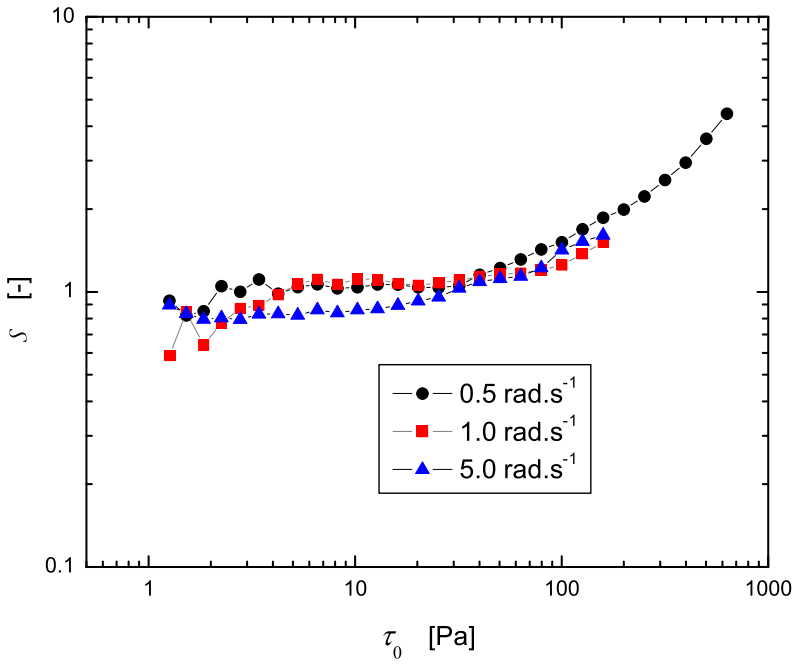

Figure 3-15: Elastic stiffening ratio, S, for an oscillatory stress sweep of pedal mucus at various frequencies.

$L \approx 50$ Pa, whereas $G_1' \approx 40$ Pa. Thus, while L slightly decreases with increasing τ_0, it does not seem to decrease relative to G_1'.

Comparing the values of L and M serves as a measure of stiffening for a material, as outlined in Section 2.3.3. This comparison is quantified by $S = L/M$, shown in Figure 3-15. In the linear viscoelastic regime it is expected that $S = 1$. This expectation agrees with the results shown in the figure, although it should be noted that noise from calculating L and M could be magnified upon the calculation of S. Nonetheless, this data of $S(\tau_0)$ confirms the strain-stiffening appearance of the Lissajous curves of Figures 3-10 to 3-12. This stiffening appears to be independent of the frequencies examined, as each curve begins to show significant stiffening near $\tau_0 \approx 100$ Pa.

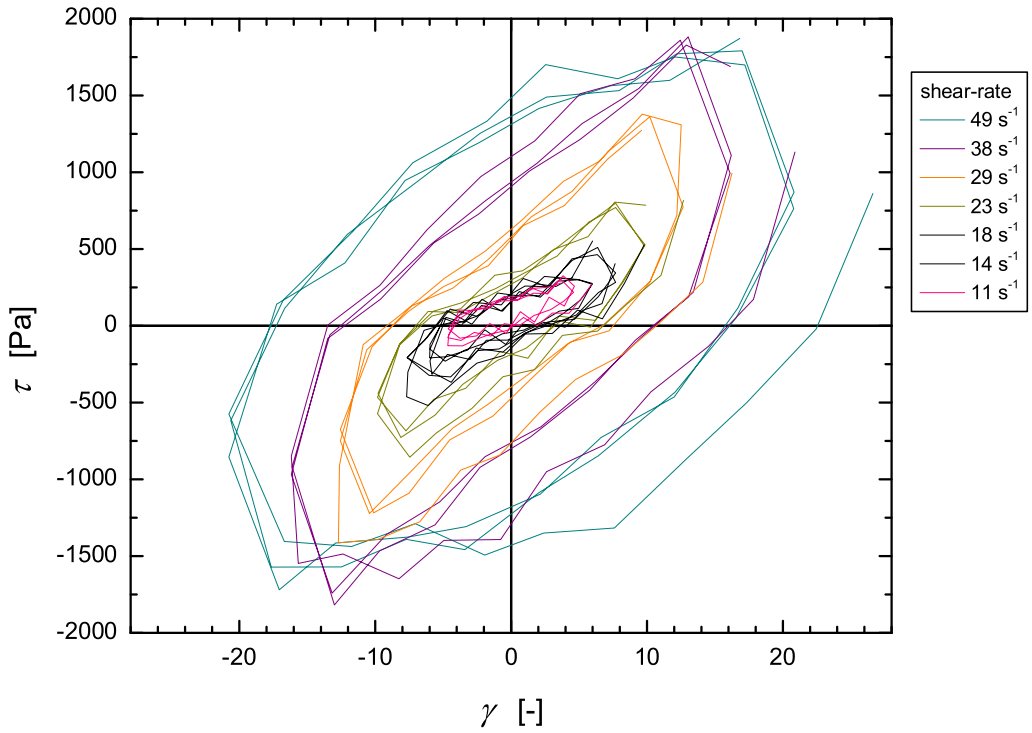

Figure 3-16: Lissajous curves for pedal mucus tested on the FMR, $\gamma_0 \leq 21$ ($A = 20$ mm^2, T=22°C, Cycle time ≈ 0.8 s).

3.3 Microgap rheology

Pedal mucus from *Helix aspera* was also tested using the Flexure-based Microgap Rheometer (FMR), which was described in Section 2.4. Steady-state flow was very difficult to achieve with pedal mucus, since the working distance of the FMR is limiting, unlike a rotational rheometer which allows for essentially infinite strain. The results should therefore be interpreted in terms of small and large amplitude cyclic tests, with the triangle wave strain input described in Section 2.4.4.

Figure 3-16 shows the results of oscillatory tests of pedal mucus with the FMR. Each cyclic test was performed with a fixed cycle period ($T_{cycle} = 0.8$ s) and varying shear-rate $\dot{\gamma}_0$. Smaller shear-rates also correspond to smaller strain amplitude γ_0, since the cycle period is fixed; for a triangle wave input these three parameters are

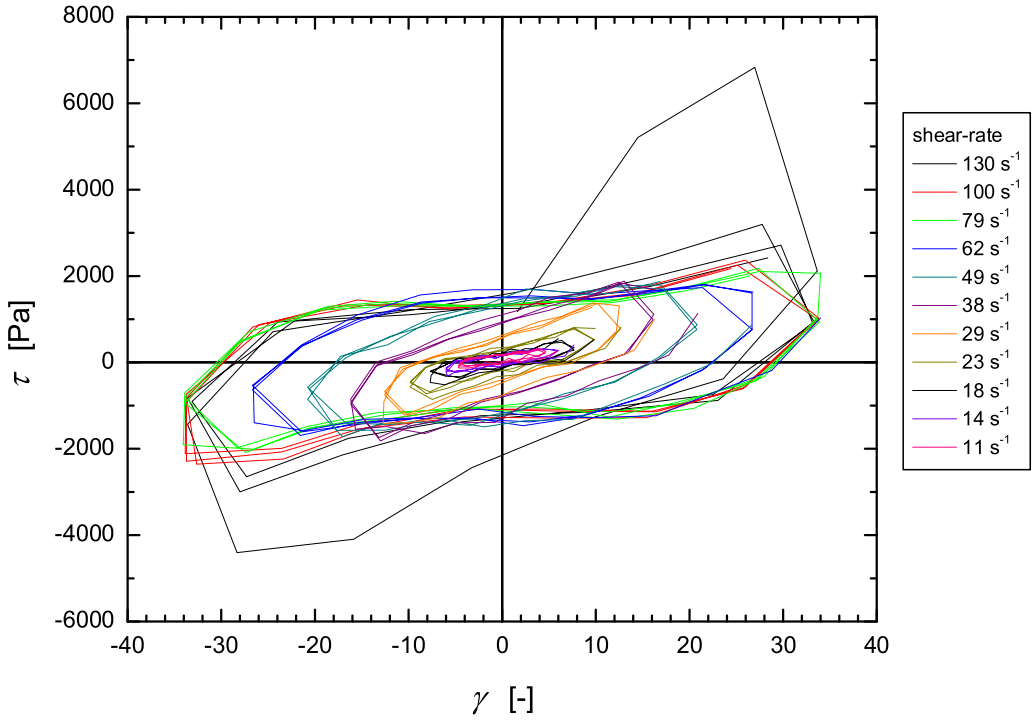

Figure 3-17: Lissajous curves for pedal mucus tested on the FMR (A = 20 mm^2, T=22°C, Cycle time $\approx$ 0.8 s).

related by

$$T_{cycle} = \frac{4\gamma_0}{\dot{\gamma}_0} = \frac{2\Delta x}{V_{plate}} \tag{3.14}$$

where Δx is the end-to-end displacement of the moving plate and V_{plate} is the velocity of the plate.

The short cycle time T_{cycle} = 0.8 s causes the data to appear slightly choppy or sparse due to the data acquisition rate of 24 Hz corresponding to 19 points per cycle. Multiple cycles are shown for each value of $\dot{\gamma}_0$ to give a sense of the average steady state response.

Unfortunately the quantitative measures M, L, and S can only be applied to the FMR results if the material displays a Kelvin-model response (as discussed in

Section 2.4.4). Although pedal mucus may respond like a Kelvin model, the data sampling was too slow and the oscillation frequency to high to capture smooth Lissajous curves. However, some remarks can still be made about the results. The data at the lowest γ_0 reported ($\gamma_0 = 4.7$) is similar to the theoretical Kelvin model response shown in Figure 2-13. As γ_0 is increased, some strain-stiffening qualities are observed, just as in the bulk rheometer results of Figures 3-10 through 3-12.

Figure 3-17 plots Lissajous curves at even larger strains for pedal mucus tested on the FMR, and includes the curves from Figure 3-16 for comparison. It should be noted that a constant cycle time T_{cycle} was programmed, but the maximum strain limits of the instrument were reached for the curves at the highest shear rates ($\dot{\gamma} = 130, 100, 79\ \mathrm{s}^{-1}$). For these shear-rates the cycle time varies while the strain amplitude γ_0 is held constant at its maximum value.

Some initial network rupture can be seen in the curve for $\dot{\gamma} = 130\ \mathrm{s}^{-1}$, as indicated by the initially large stress response that decays away as the sample continues to be periodically strained. This curve was actually the first shear-rate examined, and smaller shear-rates were subsequently tested. The maximum stress observed is over 6000 Pa, far exceeding the stress explored with oscillatory tests on the bulk rheometer. One reason that higher stress can be explored on the FMR is that the sample is not exposed to rotational motion, and therefore if the sample is ruptured there is no tendency to be thrown out of the gap.

At the largest strain-amplitude of $\gamma_0 \approx 32$ the material appears to exhibit a similar strain-stiffening to that observed with LAOS tests. Specifically, the short-range elastic modulus, qualitatively indicated by the slope $d\tau/d\gamma$ at $\gamma = 0$, progressively decreases, which can be interpreted as the destruction of elastic elements that contribute to short-range elasticity. Other elastic elements appear to still be intact, since the stress continues to increase or "strain-harden" at increasing strain.

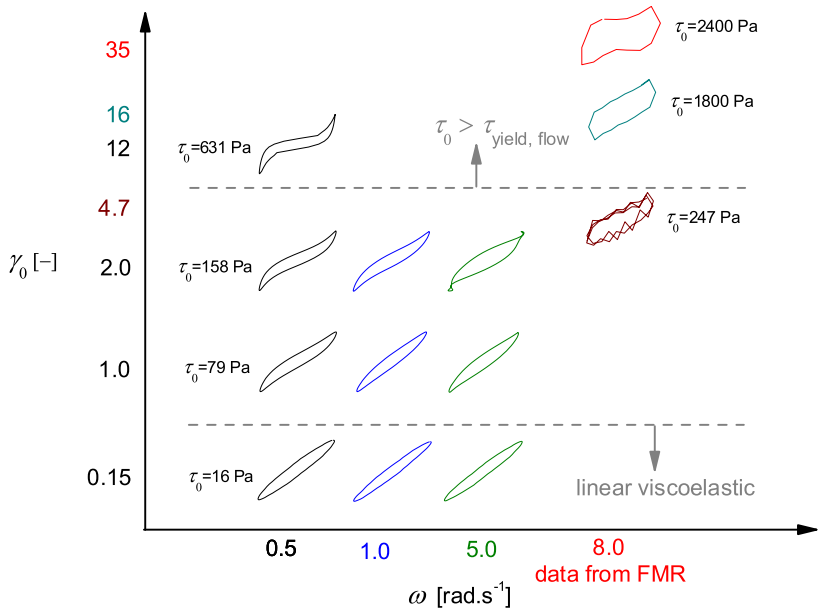

Figure 3-18: Pipkin diagram for pedal mucus of the terrestrial slug *Limax maximus*. Each point in Pipkin space has a Lissajous curve associated with it.

3.4 Overview: the Pipkin diagram

The oscillatory test results presented in this chapter can be described with the framework of a Pipkin space, which was described in Section 2.3 and shown schematically in Figure 2-1. Recall that Pipkin space maps a rheological test according to two variables: the input amplitude γ_0 (or τ_0) and the input frequency ω. The FMR results can be mapped in this space by determining the input frequency as

$$\omega_{FMR} = \frac{2\pi}{T_{cycle}} = \frac{\pi\dot{\gamma}_0}{2\gamma_0}. \tag{3.15}$$

A Lissajous curve exists for every point in Pipkin space (i.e. the (ω,γ_0) space). Figure 3-18 displays the Pipkin space of the terrestrial gastropod pedal mucus examined in this chapter. Representative Lissajous curves are shown in the different regimes of behavior. Linear viscoelastic behavior is observed for small enough input amplitude, resulting in elliptical Lissajous curves. The three curves shown in the

linear regime were tested with an imposed stress amplitude $\tau_0 = 16$ Pa. The strain amplitude response $\gamma_0 = 0.15$ was approximately the same for each of the three different frequencies. This would probably not be the case if a larger range of frequency was probed, since even a simple Kelvin model for a viscoelastic solid would predict a strain amplitude γ_0 which depends on the imposed frequency.

When the input amplitude (γ_0 or τ_0) is larger than a critical value, the rheological response of pedal mucus becomes nonlinear. The elliptical curves become exceedingly distorted further as the material is driven deeper into the non-linear regime, and the pedal mucus exhibits strain-stiffening. The strain amplitude response γ_0 is still rather independent of frequency, therefore the three curves tested under $\tau_0 = 79$ Pa and $\tau_0 = 158$ Pa all responded with $\gamma_0 = 1.0$ and $\gamma_0 = 2.0$, respectively.

A line representing the steady-state flow yield stress τ_y is shown in Figure 3-18 for reference (where $\tau_y \approx 250$ Pa as determined by the flow tests in Figure 3-1). However, the stress amplitude τ_0 required to fully yield the sample appears to be larger than τ_y, and may be a function of frequency ω. A yield strain may also be identified. Denny reports a yield strain $\gamma_y \approx 5 - 6$ for pedal mucus from *Ariolimax columbianus* as measured from step-rate tests [4]. The results shown here are consistent with that result.

As the input amplitude τ_0 is increased beyond τ_y , the Lissajous curves show even more pronounced strain-stiffening. Furthermore, the short range elastic modulus decreases as short-range elastic network components are ruptured and the sample is partially yielded. Interestingly, however, the pedal mucus continues to have an elastic nature even for $\tau_0 > \tau_y$. It is expected that the sample would fully yield at even larger τ_0, but as previously mentioned the sample was ejected from the gap at these larger stresses. It is not known if terrestrial gastropods use this peculiar feature of strain-stiffening for locomotive purposes.

Chapter 4

Modeling Adhesive Locomotion: Criteria for Optimizing a Slime Simulant

This chapter discusses different ways to model adhesive locomotion, with the goal of understanding the optimization of the working fluid. First, a simple model is developed to explore what fluid properties, in general, are required for successful adhesive locomotion on a horizontal surface. Inclined locomotion is then considered, first with a generalized Newtonian fluid (GNF) with variable viscosity. A simple model with an idealized yield stress fluid is then examined. Finally, a yield stress fluid with a finite restructuring time is used in the model. All of these models provide insight in developing criteria for optimizing a slime simulant for a mechanical crawler.

4.1 Adhesive locomotion model

Adhesive locomotion is modeled with a crawler that has discrete pads actuated by an internal force (Figure 4-1). The crawler rests on a thin film of fluid of height h. In this model a controlled force separates one pad away from the rest, while the rest are rigidly connected. A controlled force might come from muscles in real snails or from the "muscle-wire" (shape-memory alloy) that actuates Chan's robotic crawler

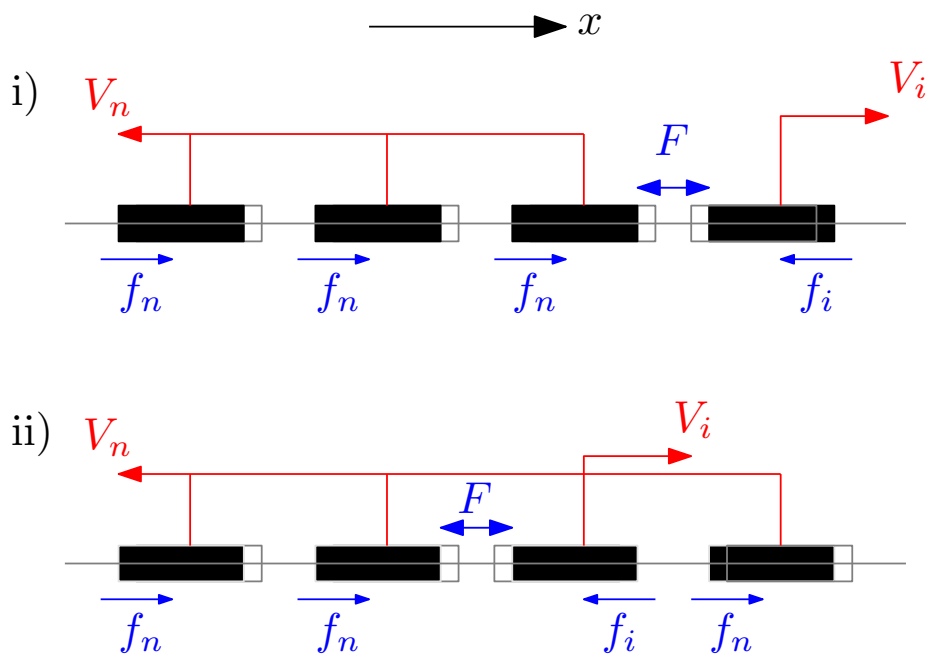

Figure 4-1: Model for discrete adhesive locomotion - the crawler consists of discrete pads and rests on a fluid with thickness h. A controlled force iteratively separates one pad from the rest.

(Figure 1-2).

This model includes several assumptions. First, acceleration is neglected. This is a reasonable approximation if the internal force F changes slow enough, so as to achieve a quasi-steady state. Second, each pad contains $1/N^{th}$ of the total mass. Third, pads moving in the same direction are rigidly connected. Thus, as depicted in the figure, only two velocities need to be considered: the velocity of the pad tending forward V_i and the velocity of all the pads tending rearward V_n. The viscous shear stress exerted by the fluid on a pad is given by $\tau = \eta\dot{\gamma}$, which neglects the end effects at the edge of the pads. Here the viscosity η is not necessarily a constant, which is known as a generalized Newtonian fluid model. The viscosity of the fluid is assumed to be a general function of shear stress, $\eta = \eta(\tau)$, motivated by the flow viscosity results in Figure 3-1.

The discrete pad model can be generalized with $\phi = 1/N$, which represents the fraction of the crawler which is moving forward. Note that ϕ is physically limited to values of $0 < \phi < 1.0$. However, due to symmetry, values of $\phi > 0.5$ will be dismissed.

F	internal force (e.g. muscles)
V_i	velocity of the pad tending forward
f_i	viscous force on pad tending forward
V_n	velocity of the pads tending rearward
f_n	viscous force on a pad tending rearward
N	number of pads
$\phi = 1/N$	fraction of crawler moving forward
A	total area of pads
A_p	area of each pad
h	fluid thickness
$\eta(\tau)$	stress dependent flow viscosity
V_{cm}	velocity of center of mass

Table 4.1: Definitions of variables for controlled-force adhesive locomotion model.

For example, $\phi = 0.2$ is the same as $\phi = 0.8$, except that the coordinate system is reversed. Therefore, in this model ϕ will be limited to values of $0 < \phi < 0.5$.

4.1.1 Velocity expression

The velocity of the center of mass will be monitored to indicate the net velocity of the crawler. Since the mass is distributed evenly among the pads, the center of mass velocity is expressed by

$$V_{cm} = \phi V_i - (1 - \phi)V_n. \tag{4.1}$$

The velocities V_i and V_n are determined by a force balance on the pads. On the forward-tending pad the actuating force F is balanced by the viscous force on the bottom of the pad. The force balance on the forward-tending pad may be expressed as

$$F = f_i = \tau_i \phi A \tag{4.2}$$

$$F = \eta(\tau_i)\frac{V_i}{h}\phi A \tag{4.3}$$

where τ_i is the shear stress acting on the fluid under the forward-tending pad, $\tau_i = F/A$. It has been noted that the shear-rate under the forward-tending pad is $\dot{\gamma}_i =$

V_i/h.

Similarly, a force balance on the rearward-tending pads provides an expression in which V_n is related to the internal actuation force F, which is given by

$$F = f_n = \tau_n[1-\phi]A \tag{4.4}$$

$$F = \eta(\tau_n)\frac{V_n}{h}[1-\phi]A. \tag{4.5}$$

Again the viscous shear stress acting on the bottom of the pads, τ_n, balances the actuation force F. Note that the total area over which the shear stress acts on the rearward-tending pads is $(1-\phi)A$.

Equation 4.3 and 4.5 can be solved explicitly for the pad velocities V_i and V_n, and then substituted into Equation 4.1 to give an expression for V_{cm} as a function of F and the viscosity function,

$$V_{cm} = \frac{Fh}{A}\left[\frac{1}{\eta(\tau_i)} - \frac{1}{\eta(\tau_n)}\right]. \tag{4.6}$$

Successful adhesive locomotion results when $V_{cm} \neq 0$. A non-zero velocity only results if $\eta(\tau_i) \neq \eta(\tau_n)$. This statement requires two features of the fluid and the mechanical crawler. That is, for successful adhesive locomotion:

1. The fluid must have a non-Newtonian viscosity.

2. Different stresses must be applied to the fluid beneath the forward- and rearward-tending pads, since even with a non-Newtonian viscosity, $\tau_i = \tau_n$ would result in the forward-tending and rearward-tending pads "feeling" the same viscosity. Thus, differential areas must be actuated to create a differential stress. Furthermore, $N = 3$ is the smallest number of pads that can produce locomotion for a crawler with discrete pads of equal area.

For $\phi < 0.5$, the forward-tending pad will always exert a higher stress on the fluid than the rearward-tending pads ($\tau_i > \tau_n$). Equation 4.6 shows that a shear-thinning fluid, $\eta(\tau_i) < \eta(\tau_n)$, will result in positive net velocity, $V_{cm} > 0$. Conversely,

a shear-thickening fluid, $\eta(\tau_i) > \eta(\tau_n)$, will result in a negative net velocity, $V_{cm} < 0$, according to the coordinate system shown in Figure 4-1. Negative net velocity is still valuable progress, since the positive direction of the coordinate system in Figure 4-1 is arbitrary.

4.1.2 Efficiency expression

A measure of locomotive efficiency for adhesive locomotion will help guide the design and material selection process. A Froude propulsive efficiency is typically used for creatures that locomote in a fluid, such as swimmers and fliers [31]. Swimmers and fliers impart momentum onto the surrounding media to propel themselves forward, thus giving the surrounding medium kinetic energy. The Froude efficiency compares the kinetic energy of the subject with the total kinetic energy of both the subject and the surrounding media,

$$\varepsilon_{\text{Froude}} = \frac{KE_{\text{subject}}}{KE_{\text{subject}} + KE_{\text{surroundings}}}. \tag{4.7}$$

However, in the case of adhesive locomotion the subject is not necessarily propelled forward by imparting momentum onto the fluid. Furthermore, the kinetic energy of the fluid is almost negligible, especially in the case of a very thin film.

Since the Froude efficiency is not useful for adhesive locomotion, a new measure is introduced. This measure of efficiency compares useful power to total dissipated power,

$$\varepsilon = \frac{P_{\text{useful}}}{P_{\text{dissipated}}}. \tag{4.8}$$

The total dissipated power can be determined from the viscous dissipation in the fluid. Conveniently, in this controlled-force model, the total dissipated power can be directly related to the actuating force, represented as

$$P_{\text{dissipated}} = FV_i + FV_n \tag{4.9}$$

Newtonian Fluid	$\eta_i = \eta_n$	$\varepsilon \to 0$
Yield Stress Fluid	$\eta_i << \eta_n$	$\varepsilon \to \phi$
Extremely Shear-thickening	$\eta_i >> \eta_n$	$\varepsilon \to (1-\phi)$

Table 4.2: Limits of locomotive efficiency ε as determined by the steady-flow viscosity function $\eta(\tau)$ of the fluid for discrete pad adhesive locomotion.

since the internal actuation force F acts on both the forward-tending and rearward-tending portions of the crawler. It is reasonable to think that the useful power should somehow be related to the center of mass velocity V_{cm} and the forward thrust on the crawler. In this controlled-force model, the thrust in the direction of motion is always F, thus the useful power is represented as

$$P_{\text{useful}} = F\,|V_{cm}|\,. \tag{4.10}$$

Therefore, the expression for locomotive efficiency becomes

$$\varepsilon = \frac{|V_{cm}|}{V_i + V_n} \tag{4.11}$$

where V_i and V_n are always positive, as defined in Figure 4-1 . The expressions for velocity as a function of internal actuation force F (Equations 4.3, 4.5, and 4.6) can be substituted into the previous expression to give

$$\varepsilon = \frac{\left|\frac{1}{\eta_i} - \frac{1}{\eta_n}\right|}{\frac{1}{\phi\eta_i} + \frac{1}{(1-\phi)\eta_n}} \tag{4.12}$$

where $\eta_i = \eta(\tau_i)$ and $\eta_n = \eta(\tau_n)$ are the viscosities of the fluid under the forward-tending and rearward-tending pads, respectively.

Equation 4.12 gives an expression for efficiency ε as a function of the number of pads on the crawler and the viscosity function of the fluid. Thus, viscosity data for real fluids can be used to determine ε for a given design platform. It is interesting to note the this expression for efficiency does not seem to depend on the mass of the robot nor the thickness of the fluid (however, V_{cm} from Equation 4.6 does depend on the fluid thickness).

It is useful to explore the limits of efficiency for some example fluids. For a Newtonian fluid, where $\eta_i = \eta_n$, the locomotive efficiency $\varepsilon = 0$. This is the expected result, since $V_{cm} = 0$ for a Newtonian fluid.

For a yield stress fluid, which is an example of the most extreme shear-thinning fluid, $\eta_i << \eta_n$, the locomotive efficiency $\varepsilon \to \phi$. For a robot with five pads, such as Chan's Robosnail, $\varepsilon = 0.2$ for a yield stress fluid. This matches with intuition if one considers that $\phi = (1/N)^{th}$ of the crawler makes forward progress on a yield stress fluid, since one pad moves forward and no pads move rearward.

Finally, in the limit of an extreme shear-thickening fluid ($\eta_i >> \eta_n$), one finds that $\varepsilon \to (1-\phi)$. For this extreme case $(N-1)$ pads are able to make progress, while one pad experiences a much higher viscosity and is essentially "stuck." Therefore the fraction of the crawler that makes progress is $(1-\phi) = (N-1)/N$. The limiting values of locomotive efficiency ε as determined by the steady-flow viscosity function are summarized in Table 4.2.

4.2 Horizontal locomotion simulation

The force-controlled adhesive locomotion model of Section 4.1 can be used with empirical steady-flow viscosity functions, $\eta(\tau)$, of real fluids to examine performance. Figure 4-2 shows the viscosity functions of four "sample" (or "candidate") fluids, including native pedal mucus from *Helix aspera*, as reported in Chapter 3. LaponiteRD in water is another yield stress fluid (details in Chapter 5). Locust bean gum in water is an example of a shear-thinning fluid, and is also discussed in more detail in Chapter 5. Cornstarch in water is a shear-thickening fluid, as indicated by the data in Figure 4-2 (Cornstarch data courtesy of Suraj Deshmukh).

Cornstarch data was fit to a quadratic expression, given by

$$\eta_{\text{cornstarch}} = 10^{-5}\tau^2 + 0.0691\tau + 0.15 \tag{4.13}$$

where τ is in units of Pa and η in Pa.s. There is no physical basis for a quadratic fit; it

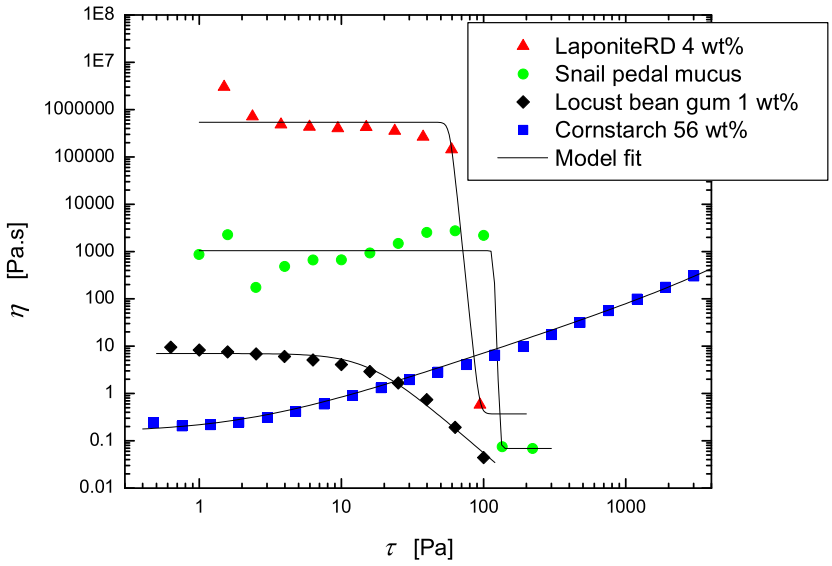

Figure 4-2: Viscosity functions $\eta(\tau)$ of some real fluids. Data for the cornstarch solution has been fit to a quadratic function, whereas each other fluid has been fit to an Ellis model. (Cornstarch data courtesy of Suraj Deshmukh, pedal mucus data reported in Chapter 3, Laponite and locust bean gum data reported in Chapter 5).

serves only to represent a continuous viscosity function that adequately matches the experimental data. The three remaining fluids were fit to the Ellis model, in general given by

$$\frac{\eta - \eta_\infty}{\eta_0 - \eta_\infty} = \frac{1}{1 + (c\tau)^d}. \tag{4.14}$$

The Ellis model represents a shear-thinning fluid that exhibits a Newtonian plateau viscosity η_0 at low-stress and a high-stress Newtonian plateau viscosity η_∞. The parameters c and d determine the location and shape of the transition between the lower and upper limits of viscosity. Table 4.3 gives the Ellis Model parameters used for the three shear-thinning fluids in Figure 4-2.

The locomotive efficiency expression given by Equation 4.12 can be used with the steady-flow viscosity functions of Figure 4-2 to examine the expected efficiency of a mechanical crawler on a horizontal surface. Using parameters that are relevant to

	η_0 [Pa.s]	η_∞ [Pa.s]	c [Pa^{-1}]	d [-]
Snail pedal mucus	1043	0.06882	0.008512	86.47
LaponiteRD 4 wt%	5.407×10^5	0.37	0.01737	28.95
Locust bean gum	7.003	2.025×10^{-9}	0.0648	2.585

Table 4.3: Ellis model parameters for three shear-thinning fluids shown in Figure 4-2.

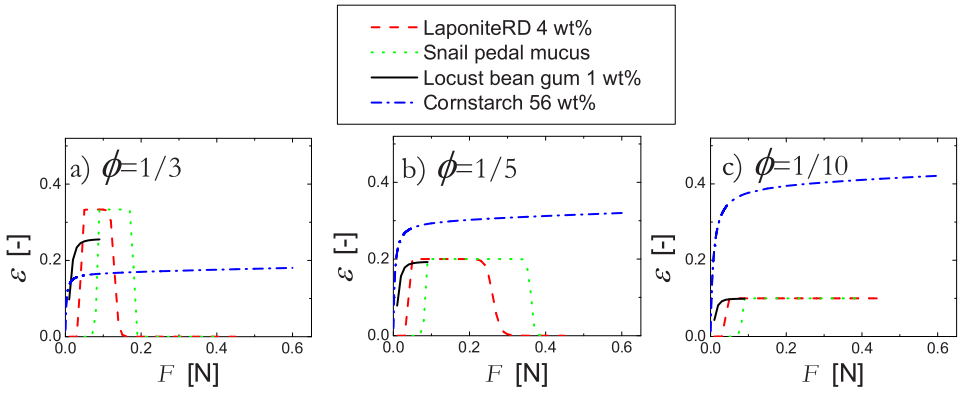

Figure 4-3: Locomotive efficiency ε as a function of actuation force F for some sample fluids using the controlled-force adhesive locomotion model on a horizontal surface.

Chan's Robosnail, the area of each pad $A_p = 6.9$ cm^2 and the thickness of fluid below each pad $h = 1$ mm. The efficiency with various ϕ and various viscosity functions are shown in Figure 4-3.

Locomotive efficiency ε is shown as a function of the internal actuation force F. For the shear-thinning fluids at low actuation force (and therefore low stress under the pads) $\varepsilon = 0$, since both the forward-tending and rearward-tending pads experience the same low-stress Newtonian viscosity η_0. For the shear-thickening fluid this also happens to be the case, since η is such a weak function at low τ. The efficiency of each fluid increases as η becomes a stronger function of τ at higher applied stress. This happens much more sharply for the yield-stress fluids, pedal mucus and LaponiteRD. The yield-stress fluids quickly reach the maximum efficiency possible for shear-thinning fluids ($\varepsilon \to \phi$). This quick jump to maximum efficiency happens for each yield stress fluid in all configurations ($\phi = 0.33, 0.2, 0.1$). The

moderately shear-thinning fluid, locust bean gum, is able to achieve the maximum possible efficiency only for $\phi = 0.2$ and $\phi = 0.1$. For $\phi = 0.33$ the smaller stress difference limits the efficiency, since the viscosity difference is not as great.

At high enough actuation force the efficiency of the yield-stress fluids drops back down to zero. This happens when the stress under the rearward-tending pads exceeds the yield stress, and all pads experience the same high-stress Newtonian viscosity η_∞. This might also be expected for the locust bean gum, but no rheological data was obtained at such high stresses, and therefore could not be used in the simulation.

The efficiency of the shear-thickening fluid increases from zero as η becomes a stronger function of τ. For $\phi = 0.33$ the shear-thickening fluid is unable to achieve an efficiency that is as high as those obtained with the shear-thinning fluids. However, for both $\phi = 0.2$ and $\phi = 0.1$ the shear-thickening fluid is able to achieve a higher locomotive efficiency than any other fluid. This might be expected, since the maximum efficiency possible with a shear-thickening fluid ($\varepsilon \to (1 - \phi)$) is higher than a shear-thinning fluid ($\varepsilon \to \phi$) as shown in Table 4.2, and a larger difference between η_i and η_n is achieved with smaller ϕ, since $\eta = \eta(\tau)$. Thus, a real shear-thickening fluid *does* have the potential to be more efficient than yield stress fluids in horizontal adhesive locomotion. It is noteworthy that nature does not use a shear-thickening fluid for adhesive locomotion, even though a higher ε appears to be possible. This could be due to several reasons, one of them being that snails also crawl up inclines, which was not considered in the previous analysis. Inclined locomotion is discussed in the following section.

4.3 Inclined locomotion model

The adhesive locomotion model developed in Section 4.1 is only applicable on a flat surface. The weight of a crawler must be considered for inclined locomotion since a component of the weight acts to provide an additional shear stress on the fluid. The sketch from Figure 4-1 is modified to consider inclined locomotion, as presented in Figure 4-4. The same assumptions apply to this modified model. Note that the

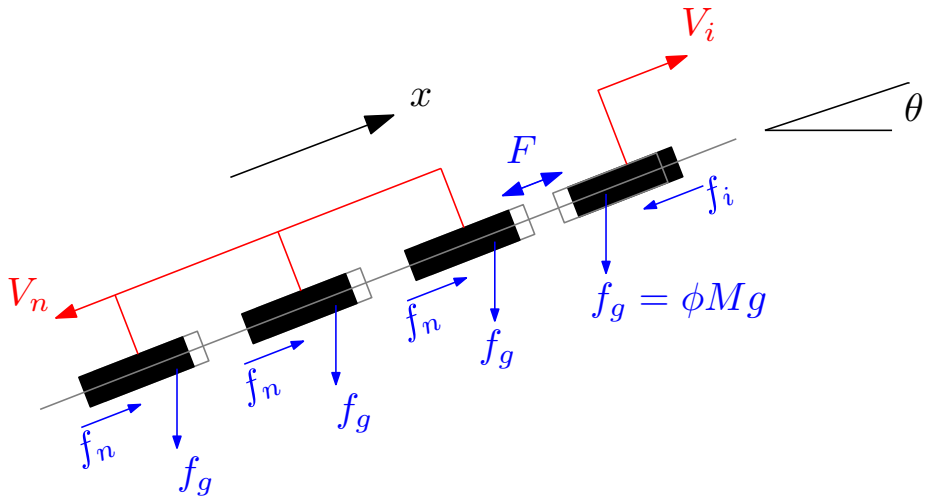

Figure 4-4: Locomotion model for discrete adhesive locomotion on an inclined surface; a controlled force iteratively separates one pad from the rest.

weight is distributed equally among the N pads, such that the magnitude of the gravitational force on each pad $f_g = \phi Mg$, where M is the total mass of the crawler.

4.3.1 Generalized Newtonian fluid

The expressions which were used to solve for V_i and V_n in the horizontal locomotion model (Equations 4.3 and 4.5) must be modified for inclined locomotion. The component of the gravitational force that opposes forward locomotion and imposes a shear stress on the fluid, $f_g \sin\theta$, must be included. As done in Section 4.1, forces are balanced on the forward-tending pad, and also balanced on the rearward-tending pads. These expressions can be solved for V_i and V_n, and used to express the center of mass velocity, resulting in

$$V_{cm} = \frac{h}{A}\left\{[F - \phi Mg\sin\theta]\left[\frac{1}{\eta_i} - \frac{1}{\eta_n}\right] - \frac{1}{\eta_n}Mg\sin\theta\right\} \tag{4.15}$$

where again $\eta_i = \eta(\tau_i)$ is the viscosity under the forward-tending pad and $\eta_n = \eta(\tau_n)$ is the viscosity under the rearward-tending pads.

For a Newtonian fluid, on an incline where $\theta > 0$, the center of mass velocity is negative, i.e. downhill. Similarly, on an incline for $\theta < 0$ the center of mass velocity is positive, which is also downhill. Thus, a Newtonian fluid cannot be used for inclined

adhesive locomotion; the crawler simply slides downhill.

A crawler could make uphill progress on a shear-thickening fluid. That is, for $\theta < 0$, the net velocity is negative and uphill. However, when the crawler rests ($F = 0$) the robot slides downhill. Thus, to maintain a given position ($V_{cm} = 0$) energy must be continuously expended.

A shear-thinning fluid can also enable an uphill velocity if the viscosity difference is dramatic enough to counteract gravity. Again for a crawler to hold its position energy must continuously be expended, since when the crawler rests it will slide downhill with a velocity

$$V_{rest} = -\frac{h}{\eta_i}\frac{Mg\sin\theta}{A}. \tag{4.16}$$

However, the downhill slide can be reduced by increasing the low-stress viscosity, η_0 in the Ellis model. As $\eta_0 \to \infty$, the fluid approaches a true yield stress fluid, where no flow occurs below a critical stress. For this idealized case, the crawler can rest without expending energy.

4.3.2 Idealized yield stress fluid

It is useful to examine a model in which the robot crawls on a yield stress fluid. That is, below a critical yield stress τ_y the fluid does not flow. This is an idealized model, but is approximately true for some fluids, especially native slime and LaponiteRD, as shown in Figure 4-2, where the low stress viscosity is on the order of 10^3 Pa.s and 10^6 Pa.s, respectively. A common constitutive equation for a yield stress fluid is the Bingham model, which relates shear stress to strain rate as

$$\tau = \tau_y + \eta_B\dot{\gamma} \tag{4.17}$$

where η_B is referred to as the plastic viscosity, but is not the apparent viscosity. An expression for apparent viscosity $\eta \equiv \tau/\dot{\gamma}$ results as

$$\eta = \infty \qquad \tau \leq \tau_y \tag{4.18}$$

$$= \eta_B + \tau_y/\dot{\gamma} \qquad \tau > \tau_y. \tag{4.19}$$

A minimum critical stress τ_y exists such that the crawler does not slide downhill. For static conditions, i.e. when no pads are being actuated, the minimum yield stress required to hold the crawler stable is

$$\tau^s_{y,min} = \frac{Mg\sin\theta}{A}. \tag{4.20}$$

There exists a different minimum yield stress for dynamic conditions, i.e. when the crawler is trying to move forward. First, notice that the actuating force must be large enough to yield the fluid under the forward-tending pad, while the shear stress exerted by the rearward-tending pads must not yield the fluid. A minimum actuating force to yield the fluid under the forward-tending pad is

$$F_{min} = \tau_y \phi A + \phi Mg\sin\theta, \tag{4.21}$$

since this force must counteract the weight of the pad and also yield the fluid. The force can not be too large, however, or the rearward-tending pads will also yield. The maximum actuating force is then expressed as

$$F_{max} = \tau_y(1-\phi)A - Mg\sin\theta(1-\phi), \tag{4.22}$$

since both the actuating force and the contribution of the weight that is distributed to the rearward-tending pads act to yield the fluid.

A minimum dynamic yield stress can be found in the limit that $F_{min} = F_{max}$, which implies that the forward-tending pad and the rearward-tending pads all yield at the same time. The minimum yield stress under a *crawling* robot is then found to

be

$$\tau^d_{y,min} = \frac{Mg\sin\theta}{A}\left[\frac{1}{1-2\phi}\right] \tag{4.23}$$

$$= \tau^s_{y,min}\left[\frac{1}{1-2\phi}\right]. \tag{4.24}$$

The minimum dynamic yield stress is therefore a factor of $1/(1-2\phi)$ larger than the static yield stress. This can be used as a design criteria when choosing a slime simulant. The result suggests that a lower yield stress is required for a crawler with a smaller proportion of forward-tending area, for example having a larger number of pads while holding the total area of the pads constant.

The minimum yield stress result can be rearranged so that, given the yield stress of a fluid τ_y, the maximum weight of the crawler can be determined. Rearranging Equation 4.23 gives

$$(Mg\sin\theta)_{max} = \tau_y A\left[1-2\phi\right]. \tag{4.25}$$

To optimize locomotion, one may want to increase speed and/or efficiency. Once the forward-tending pad has yielded the fluid, the speed of the crawler is inversely proportional to the flow viscosity. Thus, another material property to be considered for optimization is the post-yield viscosity, which should be minimized to increase the speed of the crawler. For many fluids the post-yield viscosity is not constant (e.g. the Bingham model in Equation 4.19). A benchmark for comparing fluids might be the viscosity at a certain $\dot{\gamma}$ (or τ) . For example, Chan's crawler exerts strain-rates on the fluid on the order of $\dot{\gamma} \approx 10$ s^{-1}, since $V \approx 1$ cm.s^{-1} and $h \approx 1$ mm. Thus, the post-yield viscosity can be taken at a benchmark shear rate as

$$\eta_{\text{post-yield}} = \eta|_{\dot{\gamma}=10s^{-1}}. \tag{4.26}$$

For example, the post-yield viscosity of the Bingham model (Equation 4.19) is

$$\eta_{\text{post-yield}} = \eta_B + \frac{\tau_y}{10\ s^{-1}}. \tag{4.27}$$

For this locomotion model with an idealized yield stress fluid, $\eta_n = \infty$ and $\eta_i \sim \eta_{\text{post-yield}}$ during motion.

For a yield stress fluid, where no flow occurs below a critical stress, the locomotive efficiency $\varepsilon = \phi$, as given in Table 4.2. This efficiency is independent of other material properties, and can only be changed by modifying the mechanical design. Thus no fluid properties can be optimized to improve efficiency, within the context of this idealized yield stress model. Note, however, that this is not the case with a real fluid which exhibits a finite viscosity below the yield stress, and may exhibit time-dependent effects. One time-dependent feature, a restructuring time, will be considered in the following section.

For the controlled-force adhesive locomotion model developed in this section, with a crawler on an idealized yield stress fluid, the two properties of the fluid that optimize locomotion are:

1. A minimum yield stress, $\tau^d_{y,min}$, required for stable inclined locomotion (Equation 4.23).

2. Post-yield viscosity, $\eta_{\text{post-yield}}$, minimized to increase speed (Equation 4.26).

4.3.3 Yield stress fluid with restructuring time

A further generalization of a yield stress fluid is to consider its time-dependent nature. Shearing a yield stress fluid breaks down the microstructural arrangement within the fluid; after cessation of flow the microstructure takes a finite time to rearrange and confer a yield stress upon the material again. For example, with a physical gel such as pedal mucus, the network of units is broken in order to flow, and when the flow is stopped a finite time is required for the network to restructure. This time dependent character of rheology in which structure breaks down during flow and builds up again

during rest is known as thixotropy (the reverse behavior in which shearing promotes aggregation is known as antithixotropy)[32]. The restructuring of the yield stress may take many forms. A possible expression for a yield stress with a single restructuring time is

$$\tau_y(t_r) = \tau_{y,0}(1 - e^{-t_r/\lambda}) \tag{4.28}$$

where $\tau_{y,0}$ is the long-rest-time yield stress, λ is the restructuring timescale, and t_r is the time that the material has been able to restructure, i.e. the time since the material stopped flowing.

The finite restructuring time imposes limits on the maximum velocity of an adhesive locomotion crawler. After moving a portion of its foot forward, a crawler must wait for the material to regain an adequate yield stress before actuating the next portion. The rearward-tending pads must not yield the material while the forward-tending portion exerts sufficient stress to yield the fluid. This competition can be expressed as

$$F_{min}(t) \leq F_{max}(t) \tag{4.29}$$

where $F_{min}(t)$ is the minimum required force to yield the forward-tending pad and $F_{max}(t)$ is the maximum actuation force that can be applied without yielding the fluid under the rearward-tending pads, which support the crawler. Using the expressions for F_{min} and F_{max} given by Equations 4.21 and 4.22, and considering a time-dependent yield stress, Equation 4.29 becomes

$$\tau_{y,i}(t_{r,i})\phi A + \phi Mg\sin\theta \leq \tau_{y,n}(t_{r,n})[1-\phi]A - Mg\sin\theta[1-\phi] \tag{4.30}$$

$$\tau_{y,i}(t_{r,i}) \leq \tau_{y,n}(t_{r,n})\frac{[1-\phi]}{\phi} - \frac{Mg\sin\theta}{\phi A} \tag{4.31}$$

where $\tau_{y,i}(t_{r,i})$ is the yield stress under the forward-tending portion, and $\tau_{y,n}(t_{r,n})$ is the yield stress under the most recently moved rearward-tending portion. If t_a is the time between actuating each pad, then $t_{r,i} = Nt_a = t_a/\phi$ is the time since a forward-

tending pad last yielded the fluid. Furthermore, $t_{r,n} = t_a$ since t_a is the smallest time that any rearward-tending pad has been allowed to rest. That pad would then have the lowest yield stress of all rearward-tending pads, because it has had the least time to recover its structure.

The minimum required yield stress for adhesive locomotion was given by Equation 4.23, and can be introduced into the above expression, giving

$$\tau_y(t_a/\phi)\,\phi \;\;\leq\;\; \tau_y(t_a)[1-\phi] - \tau^d_{y,min}[1-2\phi]. \tag{4.32}$$

Substituting the expression for a time-dependent yield stress (Equation 4.28) into the previous equation gives

$$\tau_{y,0}(1-e^{-t_a/(\phi\lambda)})\,\phi \;\;\leq\;\; \tau_{y,0}(1-e^{-t_a/\lambda})(1-\phi) - \tau^d_{y,min}(1-2\phi). \tag{4.33}$$

The maximum velocity of a crawler is then inversely related to the minimum time t_a which satisfies the above expression. The average velocity of the crawler, V_{cm}, on a yield stress fluid is given by (from Equation 4.1)

$$V_{cm} = \phi V_i = \phi\frac{\Delta x}{t_a} \tag{4.34}$$

where Δx is the length each pad moves during a single actuation step and t_a is again the time between actuating each pad.

Equation 4.33 can be non-dimensionalized. First, a non-dimensional yield stress τ^*_y is introduced as

$$\tau^*_y = \frac{\tau^d_{y,min}}{\tau_{y,0}}. \tag{4.35}$$

The non-dimensional yield stress is limited to the rage $0 \leq \tau^*_y \leq 1$. The limits do not come from $\tau_{y,0}$, which may have any finite value, but exist because stable locomotion can only occur if the fluid posses a large enough yield stress (Equation 4.23). The lower bound of $\tau^*_y = 0$ is set by $\tau^d_{y,min} = 0$, which corresponds to horizontal locomotion

in which the crawler does not require a yield stress to remain in place. The upper bound $\tau^d_{y,min} = 1$ is set by $\tau^d_{y,min} = \tau_{y,0}$ since stable locomotion is not possible if $\tau_{y,0} < \tau^d_{y,min}$, i.e. if the fluid's yield stress does not meet the minimum requirements.

A non-dimensional velocity V^* can also be introduced, where the average velocity V_{cm} from Equation 4.34 is scaled by the actuation step length Δx and the characteristic restructuring time λ of the fluid, given by

$$V^* = \frac{V_{cm}}{\Delta x/\lambda} = \frac{\phi \Delta x/t_a}{\Delta x/\lambda} \tag{4.36}$$

$$= \phi \frac{\lambda}{t_a}. \tag{4.37}$$

As desired, this choice for the non-dimensional variables τ^*_y and V^* completely eliminates the variables $\tau_{y,0}$, $\tau^d_{y,min}$, λ, and t_a from Equation 4.33. The non-dimensional expression that governs the crawler velocity is then given by

$$1 - e^{-1/V^*} \leq (1 - e^{-\phi/V^*}) \frac{1-\phi}{\phi} - \tau^*_y \frac{1-2\phi}{\phi}. \tag{4.38}$$

Noting that the maximum velocity V^*_{max} occurs when the above expression is an equality, and using the relation $e^{-\phi/V^*} = e^{-1/V^*} e^{(1-\phi)/V^*}$, Equation 4.38 can be rearranged to implicity solve for V^*_{max},

$$V^*_{max} = 1/\ln\left(\frac{\phi}{(1-2\phi)(1-\tau^*_y)} \left[\frac{1-\phi}{\phi} e^{(1-\phi)/V^*_{max}} - 1 \right] \right). \tag{4.39}$$

The above expression can be solved iteratively for V^*_{max} as a function of τ^* for given values of ϕ. Results for values of $\phi = 0.01 - 0.33$ are plotted in Figure 4-5. Values of ϕ are limited to $\phi = 1/N < 0.33$ since the model assumes iterative discrete pad locomotion, and $N = 3$ is the smallest number of pads that can produce locomotion. Contour lines of constant V^*_{max} are shown for values of $V^*_{max} = 0 - 1$ at intervals of 0.05. Note that $V^*_{max} = 0$ for $\tau^*_y = 1$ and that V^*_{max} increases as τ^*_y decreases.

The V^*_{max} curves dramatically increase as $\tau^* \to 0$, but do not diverge. Physically, $\tau^* \to 0$ corresponds to the case where the fluid's long-rest-time yield stress is much

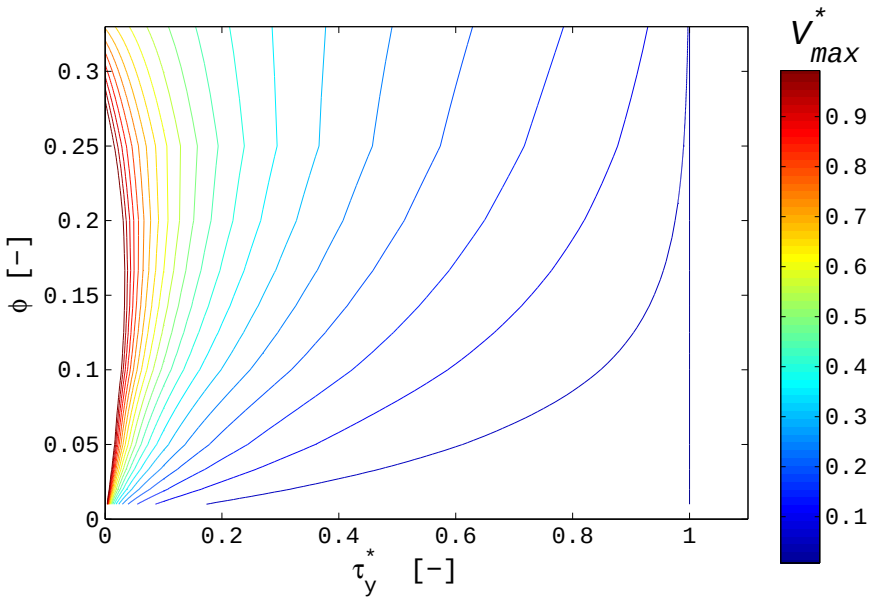

Figure 4-5: Maximum dimensionless velocity V^*_{max} of a crawler on a time-dependent yield stress fluid; contours of constant V^*_{max} are shown for values of $V^*_{max} = 0 - 1$ at intervals of 0.05. Values of V^*_{max} at $\tau^*_y = 0$ are given in the following figure.

larger than required for stable locomotion ($\tau_{y,0} >> \tau^d_{y,min}$). The values of V^*_{max} at $\tau^*_y = 0$ are shown in Figure 4-6 as a function of ϕ.

The maximum *dimensional* crawling velocity of the center of mass is determined by

$$V_{cm,max} = V^*_{max} \frac{\Delta x}{\lambda}. \tag{4.40}$$

For example, for $V^*_{max} = 1$, if the crawler displaces each pad a distance $\Delta x = 1$ cm during an actuation step, and the restructuring time of the fluid $\lambda = 10$ s, the maximum dimensional velocity $V_{max} = 1$ mm.s^{-1}. It is apparent that V_{max} is inversely proportional to the restructuring time λ for a given V^*_{max}.

If a fluid has a very fast restructuring time, then the maximum dimensional velocity may be quite large, for example if $\lambda = 10^{-3}$ s and $\Delta x = 1$ cm, then the maximum velocity $V_{max} = 10$ m.s^{-1}. The resulting velocity may be much larger than the crawler is physically capable of providing, for example being limited by the maximum velocity of the actuators moving the pads. In this case it is the mechanical design that limits

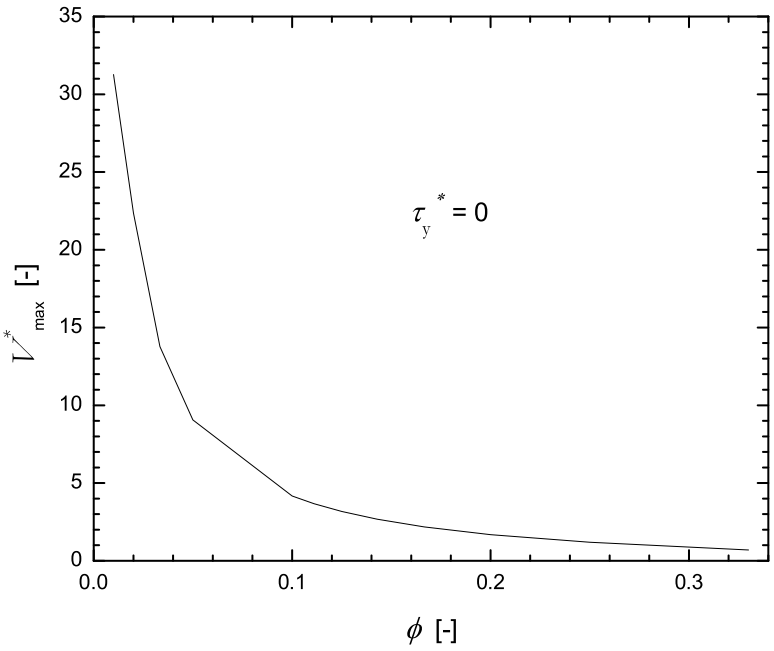

Figure 4-6: Maximum dimensionless velocity V^*_{max} when $\tau^*_y = 0$ for a crawler on a time-dependent yield stress fluid.

the velocity, and not the restructuring time of the fluid.

In conclusion, the restructuring time λ of a yield stress fluid should be minimized to increase the velocity of a mechanical crawler. There is a lower limit to minimizing λ, since eventually the mechanical design will limit the velocity. The restructuring time does not affect the locomotive efficiency ε of a yield stress fluid, since $\varepsilon \rightarrow \phi$ for a yield stress fluid, as shown in Table 4.2.

For adhesive locomotion on an inclined surface, using the most general yield stress fluid which includes a restructuring time (Equation 4.28), the following properties of the fluid should be sought:

1. A minimum yield stress $\tau^d_{y,min}$ (Equation 4.23), which is required for adhesive locomotion on an inclined surface.

2. Post-yield viscosity, minimized to increase speed (Equation 4.26).

3. Non-dimensional yield stress τ^* (Equation 4.35), minimized to increase crawler speed (Figure 4-5).

4. Restructuring time λ of a yield stress fluid (Equation 4.28), minimized to increase speed (Equation 4.40).

Furthermore, locomotive efficiency ε for a simple yield stress fluid is only a function of ϕ, the fraction of the crawler that iteratively moves forward (Table 4.2). No fluid properties can be optimized to improve the locomotive efficiency within the framework of a simple yield stress fluid. However, a real fluid will possess a finite η for $\tau < \tau_y$, and this low stress viscosity should be maximized to improve ε and reduce rearward motion during rest.

Chapter 5

Survey of Possible Slime Simulants

The material selection criteria developed in Section 4.3.3 are now used to compare the potential of possible slime simulants for adhesive locomotion with a mechanical crawler. A variety of yield stress fluids will be surveyed, including native mucus, polymer gels, particulate gels, emulsions, foams, and field-responsive fluids. Results from personal experiments and scientific literature will be used.

Two material properties will be used to compare possible slime simulants: the yield stress τ_y and the post-yield viscosity $\eta_{\text{post-yield}}$. Recall from Section 4.3.3 that a minimum yield stress $\tau^d_{y,min}$ exists to enable adhesive locomotion, given by Equation 4.23. This minimum yield stress $\tau^d_{y,min}$ for Chan's mechanical crawler climbing up a vertical wall is $\tau^d_{y,min} = 150$ Pa, since $Mg = 0.31$ N, $A = 5 \times 6.9$ cm^2, and $\phi = 1/N = 0.2$. Furthermore, $\eta_{\text{post-yield}}$ should be minimized to increase locomotive speed. The restructuring time λ will not be fully considered at this time; the limit $\lambda \to 0$ will be used to simplify the problem, which allows the fluid to be modeled as a Generalized Newtonian Fluid. Furthermore, information regarding a time-dependent yield stress is rarely reported in the scientific literature.

A dimensionless measure which compares the yield stress τ_y and the flow viscosity η is the Bingham number, Bn. The Bingham number is motivated by the Bingham model of a yield stress material, which was given by Equation 4.17. The Bingham

number Bn is defined as

$$Bn \equiv \frac{\tau_y}{\tau_{flow}} = \frac{\tau_y}{\eta\dot{\gamma}} \tag{5.1}$$

which is a comparison of the yield stress to the viscous flow stress. For adhesive locomotion Bn compares the stress which supports the crawler under static (no flow) conditions to the stress which resists locomotion. Since the viscosity is a function of shear rate, a representative $\dot{\gamma}$ must be chosen to calculuate Bn. As outlined in Section 4.3.2, $\eta_{\text{post-yield}}$ is taken at a shear rate $\dot{\gamma} = 10\ \text{s}^{-1}$, which is a representative shear rate for Chan's mechanical crawler, since $V \approx 1\ \text{cm.s}^{-1}$ and $h \approx 1\ \text{mm}$. A large Bn optimizes adhesive locomotion, since a high yield stress is increases support of a crawler and a small flow viscosity increases crawler speed.

Legend name	Description	Reference
Banana slug	Native pedal mucus from the banana slug (*Ariolimax columbianus*)	[4]
Rice eel	Native mucus which covers the outer body of the rice eel (*Monopterus albus*)	personal data
Garden snail	Native pedal mucus from the common garden snail (*Helix aspera*)	personal data

Table 5.1: Details of mucus data which is shown in Figures 5-1 to 5-4.

Native mucus will be used as a benchmark to which other fluids will be compared. Table 5.1 gives the details of three native mucus gels used for this study. The terrestrial slug *Ariolimax columbianus* and the terrestrial snail *Helix aspera* use their pedal mucus for adhesive locomotion. Pedal mucus was collected as described in Section 2.1. The mucus from the rice eel (*Monopterus albus*) is excreted on the outer body, and is not used for adhesive locomotion; however, as the mucus exhibits a yield stress it will be used for comparison. Mucus was collected by removing an eel from its water environment and scraping off the slime with a latex-gloved hand. Mucus

was immediately deposited on a rheometer for testing.

5.1 Polymeric gels

Many polymeric gels exhibit the critical material property required for inclined adhesive locomotion, that is, a recoverable yield stress. Table 5.2 lists some selected polymer gel materials and indicates the source of the data. Material preparation and testing protocols can be found in the cited references.

5.1.1 Material preparation

Preparation of the materials personally tested will be described in this section.

Carbopol is a high molecular weight carbomer (a polymer of acrylic acid) used to modify the rheology of a variety of personal care products. Carbopol 940 was obtained from the Noveon corporation (Cleveland, OH). Slime simulants based on Carbopol were prepared at various concentrations ranging from 0.5% - 4% (w/w), where w/w refers to weight of the additive with respect to the total weight of the mixture. The polymer was obtained as a white powder, and was added to deionized water being agitated with a magnetic stirrer. Samples were mixed for a minimum of 30 minutes. The Carbopol-water mixtures initially have a pH near 3, and each was neutralized with NaOH to achieve a pH = 7, which produces a clear gel. The rheology of Carbopol mixtures depends on the pH, with maximum thickening occurring within a pH range 5-9 [40]. Carbopol dispersions are typically interpreted as microgels [41, 42], in which crosslinked polymer particles are formed and swell in water. The outside of each particle exposes dangling ends which overlap with the dangling ends of other particles above a critical concentration, producing a sample-spanning network structure.

High vacuum grease was purchased from the Dow Corning Corporation (Midland, MI). Aloe gel was purchased under the Banana Boat brand name, labeled as *Soothing Aloe Aftersun Gel*. The aloe gel is distributed by Sun Pharmaceuticals Corp (Delray Beach, FL). Locust bean gum was a gift from P.L. Thomas & Co., Inc. (Morristown,

Legend name	Description	Reference
Grease	Dow Corning high vacuum grease	personal data
Grease in oil	Dow Corning high vacuum grease in 0.1 Pa.s silicone oil; 15wt%, 25wt%	courtesy of Suraj Deshmukh
Alginate	Alginate in water; 4.4% (w/w) with Ca cations; τ_y extrapolated from data	[33]
Carageenan	Grindsted Carageenan in water; 2%, 3%	[34]
Xanthan	Xanthan in water; 1%, 2%, 3%	[34]
LBG/Xanthan	Locust bean gum and xanthan in water (1:1); 0.8% (w/w) total, $\eta_{\text{post-yield}}$ unavailable	[35]
Dextran	Dextran in water; 250mg/ml; 0mM $CaCl_2$, 1.9mM $CaCl_2$; τ_y and $\eta_{\text{post-yield}}$ extrapolated from data	[36]
HPG3	hydrophobically modified (hydroxypropyl) guar, called HPG3, in water; 1.5wt%; $\eta \approx 10^2$ Pa.s for $\tau < \tau_y$	[37]
Carbopol	Carbopol 940 in water, pH7; 0.5%, 1%, 2%, 3%, 4% (w/w)	personal data
Aloe Gel	Banana Boat, Soothing Aloe Aftersun Gel	personal data
Collagen	Type I collagen in water; 0.5%, 2%, 3.5%, 5% (w/w)	personal data
Blend	Carbopol 940 : sodium alginate : guar gum in artificial tear fluid; 0.5:0.2:0.2, 0.6:0.3:0.3; unknown concentration, fit to Bingham model	[38]
Hair gel	Miss Helen blue hair gel	[39]
LBG	Locust bean gum in Ringer's solution; 1% (w/w)	personal data

Table 5.2: Details of the polymer gels shown in Figure 5-1.

NJ). Locust bean gum was added directly to a Ringer's solution and mixed with a magnetic stirrer. The Ringer's solution is DI water containing 0.86 mg/ml NaCl, 0.03 mg/ml KCl, and 0.033 mg/ml CaCl.

The collagen mixture was prepared by adding 0.25 g of microfibrillar, type I collagen isolated from bovine tendon (Integra LifeSciences, Plainsboro, NJ) to 4 ml of DI water. After mixing the solution, 1 ml of 3.0M acetic acid was injected, resulting in a mixture of 5% (w/w) collagen in 0.6M acetic acid solution. The collagen and acetic acid solution was mixed using two syringes joined with a female-female Luer-lock assembly, in which the solution was pushed from one syringe to another ten times in succession. The solution was allowed to rest for three hours in order to equilibrate. The mixture was then centrifuged for 45 minutes at 4000g to remove air bubbles. The resulting clear gel was kept at 4°C until it was needed for testing.

5.1.2 Results

The yield stress τ_y and post-yield viscosity $\eta_{\text{post-yield}}$ of the polymeric gels described in Table 5.2 are shown in Figure 5-1, along with the results of the native mucus samples listed in Table 5.1. Figure 5-1 is a plot of τ_y and $\eta_{\text{post-yield}}$ for each material. The minimum required yield stress, $\tau^d_{y,min}$ of Chan's crawler is shown for reference, to divide the plot into regions of feasible an infeasible materials for allowing the crawler to traverse a vertical wall. Additionally, lines of constant Bn are shown, which appear as diagonal lines with a slope of one.

It is immediately apparent that a few polymeric gels have a yield stress which would support the adhesive locomotion of Chan's crawler on a vertical surface. Grease, collagen, carbopol, and dextran all have a sufficient yield stress. However, none of the other materials have a sufficient yield stress at the concentrations tested.

Many of the polymeric gels have a Bingham number in the range $0.1 < Bn < 1$, even as the concentration is varied. Furthermore, the Bingham number often remains constant as concentration is varied, which implies that τ_y and $\eta_{\text{post-yield}}$ are affected by concentration in the same way. As concentration is increased so that a sufficient τ_y is achieved, $\eta_{\text{post-yield}}$ will increase by the same proportion. In other words, the increased resistance to motion is a price to be payed for reaching a higher yield stress.

Two native mucus samples have $Bn > 1$: Banana slug pedal mucus, and Rice eel mucus. This means that the viscous, or dissipative, stress at $\dot{\gamma} = 10\ \text{s}^{-1}$ is less than

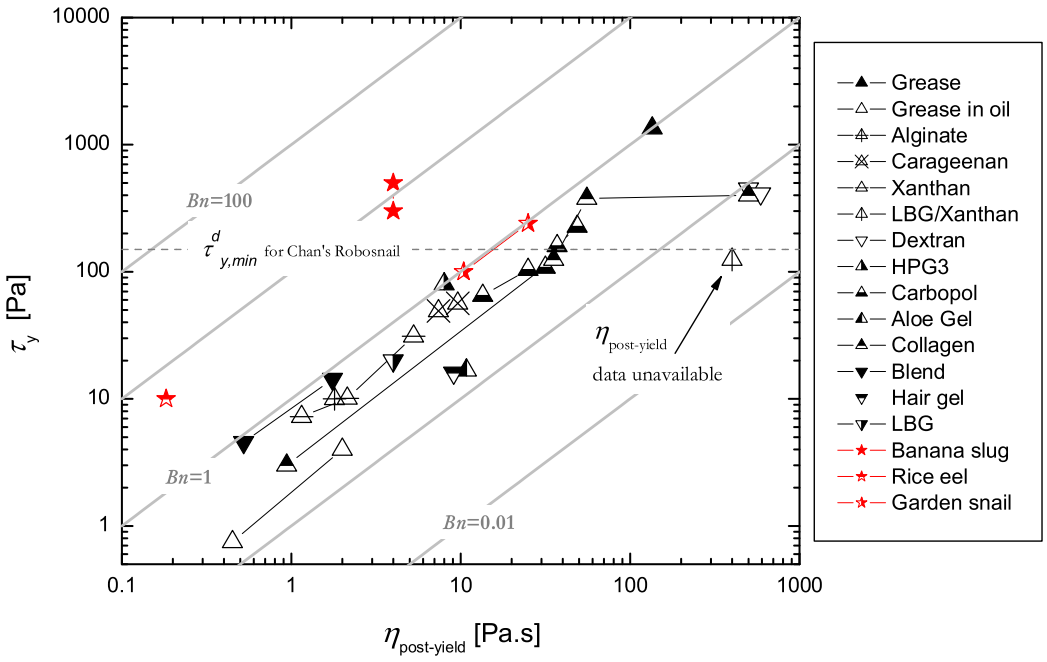

Figure 5-1: Material selection space for comparing yield stress fluids - Polymer Gels.

τ_y.

The carbopol gel is produced from a commercially available polymer, which allows the rheology to be examined as a function of concentration (unlike the grease, for example). A more detailed rheological study of the carbopol mixture will be given in Chapter 6, where it will be compared directly with native pedal mucus.

5.2 Particulate gels

A selection of particulate gels are listed in Table 5.3. The table gives some details of the materials, along with reference information. Details of the material preparation and testing protocol can be found in the appropriate references.

Legend name	Description	Reference
Laponite	LaponiteRD in water, pH=10; 3%, 4%, 5%, 7% (w/w)	personal data
Bentonite 1	Na_2CO_3-activated Kutahya bentonite in water-based solution, 2.5% Na_2CO_3; 2%, 4%, 6%; $\eta_{\text{post-yield}}$ reported at $\dot{\gamma}$=348 s^{-1}	[43]
Bentonite 2	Ca-bentonite and Na-bentonite in water; 2% (w/w), τ_y extrapolated from data	[44]
Bentonite 3	Clarsol FB5 bentonite in water; 3% - 11% (w/w); τ_y measured with vane technique, $\eta_{\text{post-yield}}$ unavailable	[45]
Cloisite	Exfoliated montmorillonite clay (Cloisite 20A) in xylene; 1% - 10% (w/w),	[46]
Shp clay 1	Jebel Shemsi clay in water; 8%-11% (w/w), $\eta_{\text{post-yield}}$ unavailable	[47]
Shp clay 2	Jebel Shemsi clay in water-salt; 8.5%(w/w); 0M-0.2M NaCl, $\eta_{\text{post-yield}}$ unavailable	[47]
Kaolin	Kaolin (plate-like particles) in water; 51% (w/w)	[48]
TiO_2	A-HR TiO_2 (sphere-like particles, 0.5μm diameter) in water, pH=2.4; 50% (w/w)	[48]
SiO_2	Mixture of SiO_2 flour and R-HD2 TiO_2 in water (1.00:0.12), ; 70% (w/w) total solids concentration, $\eta_{\text{post-yield}}$ unavailable	[48]

Table 5.3: Details of the particulate gels shown in Figure 5-2.

5.2.1 Material preparation

Laponite was the only material personally prepared and tested. LaponiteRD was obtained from Rockwood Specialties Group, Inc. (Princeton, NJ). LaponiteRD is a disc-shaped colloidal particle measuring approximately 30 nm in diameter and 1 nm in thickness [49]. Laponite clay particles form a fractal network when mixed with water at sufficient concentration [50]. If the colloidal dispersion is properly filtered,

however, it forms a colloidal glass [51].

Simulants based on Laponite were prepared at concentrations ranging from 1% to 7% (w/w), where w/w refers to weight of the additive with respect to the total weight of the mixture. A yield stress was not observed for concentrations of 2.5% or less. Dispersions were prepared by adding Laponite powder to deionized water being agitated with a magnetic stirrer. Samples were mixed for 30 minutes, centrifuged, and degassed to remove air bubbles. In all cases a clear solution was formed. Laponite dispersions were brought to pH=10±5% by addition of NaOH to make them chemically stable [49]. Dispersions were kept in a sealed container and allowed to rest for a minimum of 6 hours before testing.

Immediately before testing, Laponite samples were subjected to a pre-shear at a shear rate $\dot{\gamma} = 5\ \mathrm{s}^{-1}$ for 25 seconds, followed by three minutes of recovery. The pre-shear and recovery sequence helped to erase strain history and sample loading effects, as Laponite is known to be thixotropic and to exhibit "rheological aging" even under quiescent conditions [50].

5.2.2 Results

Results for the particulate gels are shown in Figure 5-2. For some materials $\eta_{\text{post-yield}}$ data was not available; these materials are plotted in the region where $\eta_{\text{post-yield}} \geq 100$ Pa.s at arbitrary values of $\eta_{\text{post-yield}}$. Additionally, viscosity data for the Bentonite 1 sample was only reported for $\dot{\gamma} = 348\ \mathrm{s}^{-1}$, thus the magnitudes of the lines of constant Bn do not apply to this sample, since the lines strictly correspond to a shear-rate $\dot{\gamma} = 10\ \mathrm{s}^{-1}$.

Four particulate gel samples meet the minimum yield stress criteria for Chan's Robosnail: Laponite, Cloisite, Shp clay, and TiO_2. It is also apparent that many particulate gel samples fall very close to the line $Bn = 1$. The value $Bn = 1$ corresponds to the yield stress being exactly equal to the viscous flow stress at the specified shear rate. This situation may easily occur for a material whose viscosity drops many orders of magnitude within an extremely narrow range of stress. This is the case of pedal mucus from *Helix aspera*, as shown previously in Figure 3-1 which plots the

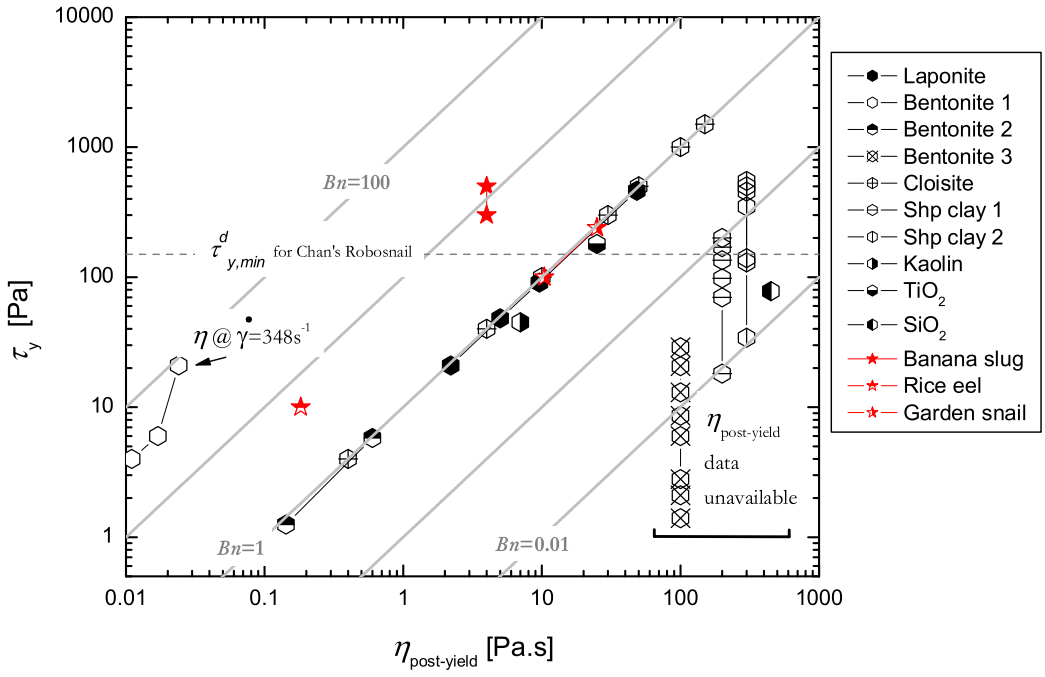

Figure 5-2: Material selection space for comparing yield stress fluids - Particulate Gels.

steady state flow viscosity η as a function of shear stress τ. That so many particulate gels fall on the line $Bn = 1$ implies that viscosity drops dramatically within a very narrow range of imposed shear stress.

LaponiteRD was available to be examined as a function of concentration. A more detailed rheological study of the laponite mixtures will be given in Chapter 6, where it will be compared directly with native pedal mucus.

5.3 Emulsions, foams, and composites

A number of emulsions were surveyed for this study. A wet foam is similar in morphological structure to an emulsion, and so this category is also included in this section. More complicated materials, such as peanut butter, are also included in this section. Peanut butter is partly emulsified but also includes solid material suspended throughout the material. Toothpaste is also a complicated material, consisting of

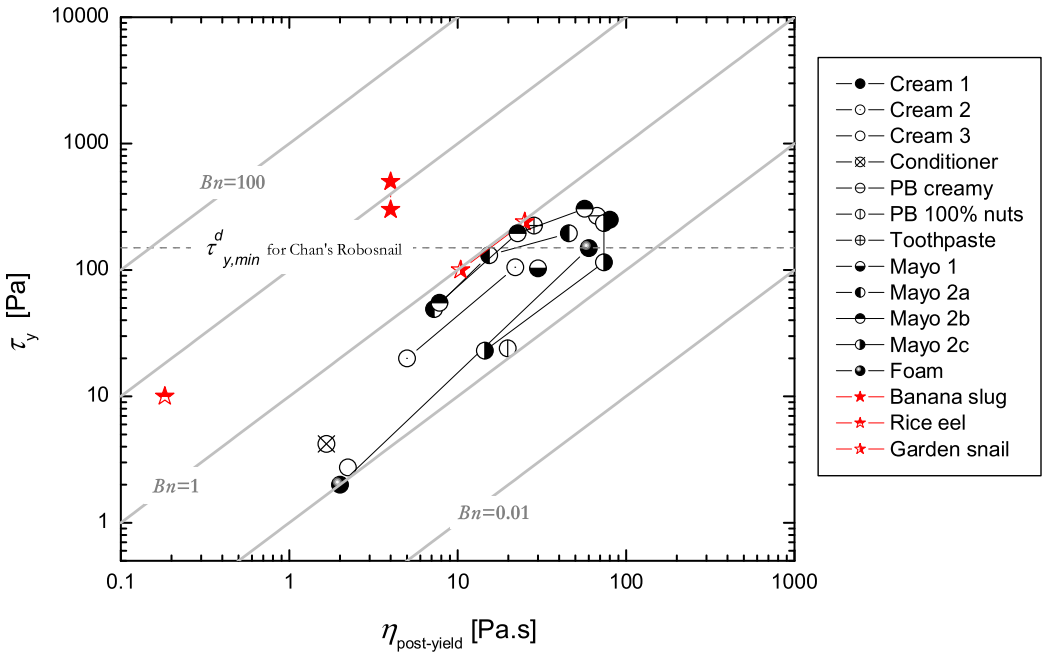

Figure 5-3: Material selection space for comparing yield stress fluids - Emulsions, Foams, and Composites.

solid materials. All of the emulsions, foams, and composites examined for this study are listed in Table 5.4.

5.3.1 Material preparation

All personally tested materials were available as commercial products. The Cream 3 and Conditioner samples are made available by Westin hotels under the Heavenly Bath brand name. Toothpaste was purchased from a local store, sold by the Crest Co., labeled as *Regular paste - tartar control*. The toothpaste is opaque, and light blue in color.

5.3.2 Results

The yield stress and post-yield viscosity values for the materials listed in Table 5.4 are shown graphically in Figure 5-3.

Legend name	Description	Reference
Cream 1	Commercially available skin creme (brand not reported)	[25]
Cream 2	Prepared lamellar gel-structured "cream" containing emulsifiers, 2% triethanolamine, and water; 6.5% and 13% emulsifiers	[52]
Cream 3	Westin's Heavenly Bath brand "hydrating cream"	personal data
Conditioner	Westin's Heavenly Bath brand conditioner	personal data
PB creamy	Commercially available "smooth" peanut butter (brand not reported), data fit to Bingham model	[53]
PB 100% nuts	Commercially available "100% peanuts" peanut butter (same brand as above, but not reported), data fit to Bingham model	[53]
Toothpaste	Crest regular paste	personal data
Mayo 1	Factory sample of mayonnaise, fit to Herschel-Bulkley model	[52]
Mayo 2a	Apparent rheology of mayonnaise prepared with various xanthan gum concentrations; 50% (w/w) oil; 0.5%, 1.0%, 1.5% (w/w) xanthan gum	[54]
Mayo 2b	Same physical sample as Mayo 2a but with data corrected for slip	[54]
Mayo 2c	Slip corrected rheology of mayonnaise prepared with various oil concentrations, no xanthan gum; 75%, 80%, 85% (w/w) oil	[54]
Foam	Commercial shaving foam (Gilette Foamy, regular), tested with rough surface, fit to Herschel-Bulkley model	[39]

Table 5.4: Details of the emulsions, foams, and composites shown in Figure 5-3.

Legend name	Description	Reference
MR fluid	Carbonyl iron powder (CIP) (1.1 μm diameter) in grease/oil mixture; 0.0, 0.05, 0.09, 0.13 Tesla	[55]
ER fluid	Surface modified complex strontium titanate particles in silicone oil ($\nu = \eta/\rho = 5 \times 10^{-5}$ m^2/s); 23% (v/v); 1.0, 1.8 kV/mm	[56]

Table 5.5: Details of the field-responsive fluids shown in Figure 5-4.

Many of the materials shown in Figure 5-3 are able to meet the minimum yield stress criteria for Chan's Robosnail: Cream 1, PB creamy, Toothpaste, and some concoctions of the Mayo 2 sample. The highest yield stress values are only 2-3 times as large as the required yield stress. This is in contrast to the highest yield stress values within the polymer gel and particulate gel categories, some of which were nearly 10 times as large as the minimum required yield stress.

All of the materials shown in Figure 5-3 fall between $0.1 < Bn < 1$, and many maintain the same value of Bingham number as concentration is varied. Similar to the findings for polymer gel and particulate gel materials, the yield stress and post-yield viscosity seem to increase colinearly.

An important note should be made about the data shown for the Mayo 2a and Mayo 2b samples, which give the apparent and slip corrected data, respectively. Although the data labeled as Mayo 2b may better describe the material since it is corrected for the slip which occurred during testing, it may not be the best indicator of what will happen under a real crawler. Thus, the apparent yield stress and apparent viscosity, which is given by the data labeled Mayo 2a, would be a better indicator of the performance of the material under an actual mechanical crawler, where slip is likely to occur.

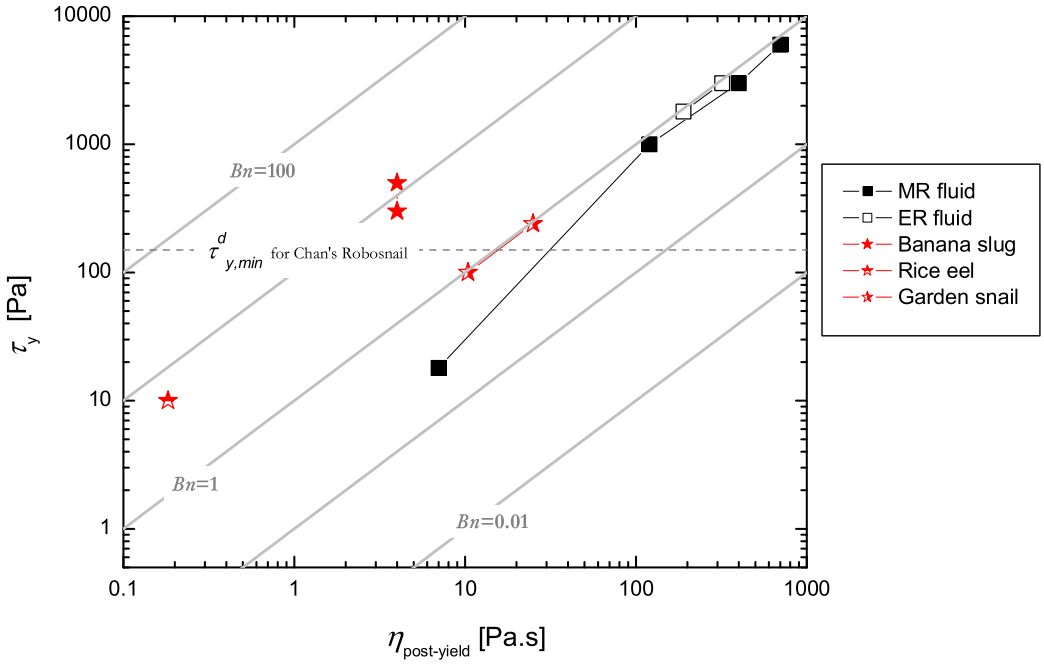

Figure 5-4: Material selection space for comparing yield stress fluids - Field-Responsive Fluids.

5.4 Field-responsive fluids

Field-responsive fluids are able to change their mechanical properties when exposed to an electric or magnetic field. These materials frequently show very high yield stresses when exposed to the appropriate field. Of course, for a crawler to exploit the field-induced properties of these materials, electric or magnetic fields must be generated between the crawler and the substrate. Table 5.5 lists two field-responsive fluids examined for this study.

5.4.1 Material preparation

Neither of the materials listed in Table 5.5 were personally prepared. Details of material preparation can be found in the references given in Table 5.5.

5.4.2 Results

The yield stress and post-yield viscosity data for the two field-responsive fluids are shown in Figure 5-4. Each fluid is able to achieve a yield stress more than one order of magnitude larger than the minimum required yield stress for Chan's Robosnail. Thus, even though an electric or magnetic field generator would need to be carried by the crawler, the materials may still provide an adequate yield stress to carry the additional weight. Furthermore, each fluid achieves $Bn \approx 1$, indicating a dramatic drop in viscosity over a small range of applied shear stress.

5.5 Conclusions

In summary, this chapter has shown that several candidate materials are available which would allow inclined locomotion of a mechanical crawler. No materials have $Bn > 1$, other than some natural mucus gels, and for many materials $0.1 < Bn < 1$. Each category of viscoplastic materials contains multiple formulations which exhibit an adequate yield stress for wall climbing. Some polymeric gels and particulate gels far-exceed the required yield stress, $\tau^d_{y,min}$, whereas emulsions only narrowly exceed the required yield stress. Field-responsive fluids also far exceed $\tau^d_{y,min}$, but require the generation of a magnetic or electric field. Future tests should also compare the restructuring time λ of those materials which meet the minimum yield stress criteria, since this parameter was also shown to influence adhesive locomotion performance (Section 4.3.3).

Chapter 6 will examine the detailed rheology of two promising simulants: a polymer gel (Carbopol) and particulate gel (Laponite). The linear and nonlinear rheology of these two potential simulants will be compared with that of native slime.

Chapter 6

Results: Detailed Rheology of Two Slime Simulants

Two promising slime simulants, based on Laponite and Carbopol, were examined in detail and compared with native pedal mucus from the terrestrial snail *Helix aspera* and the terrestrial slug *Limax maximus*. Comparisons were made using traditional rheological measurements, including flow viscosity, creep, and small amplitude oscillatory shear (SAOS). Furthermore, the nonlinear rheology of each simulant is compared with that of pedal mucus (which was reported in Chapter 3).

6.1 Steady shear flow

The steady shear viscosity of the Carbopol-based and Laponite-based simulants are shown in Figures 6-1 and 6-2, respectively. The steady shear viscosity of native pedal mucus from *Hexlix aspera* is also shown for reference in each figure. Henceforth, the Carbopol-based simulant will be referred to as Carboslime and the Laponite-based simulant will be referred to as Laposlime. Material preparation and testing protocols for Carboslime and Laposlime were given in Sections 5.1.1 and 5.2.1, respectively.

All tested concentrations of Carboslime exhibit an apparent yield stress (i.e. concentrations $\geq$ 0.5%, where % implies (w/w) concentration throughout this entire chapter). Laposlime shows an apparent yield stress for concentrations $\geq$ 3%. Each

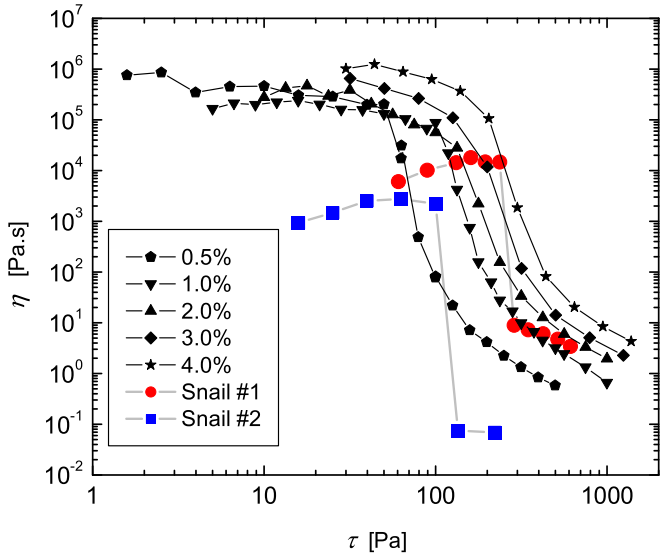

Figure 6-1: Steady shear flow viscosity of Carboslime (Carbopol940 in water, pH7), 0.5%–4.0% (AR1000, plate with sandpaper, h=1000 μm, T=25°C, solvent trap; plate diameter D=4 cm for 0.5%–2%, D=2 cm for 3%–4%). Pedal mucus data from Figure 3-1.

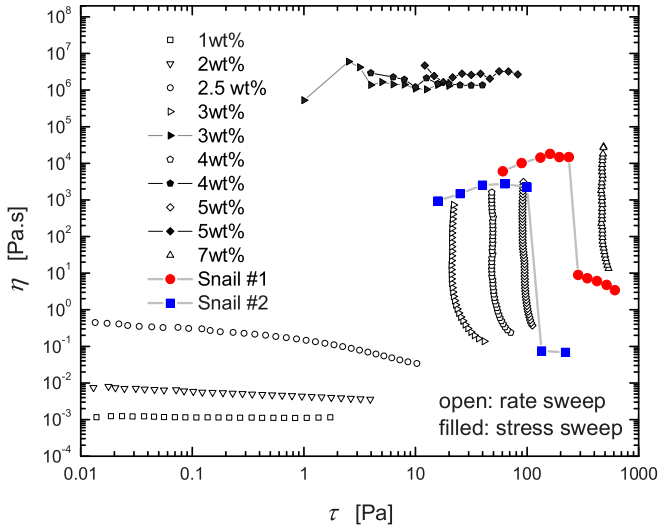

Figure 6-2: Steady shear flow viscosity of Laposlime (LaponiteRD in water, pH10), 1%–7% (AR1000, T=25°C, solvent trap; various geometries, D=6 cm 1° cone for 1%–2%, D=4 cm 2° cone for 2.5%, D=4 cm plate h=1000 μm with sandpaper for 3%–7%). Pedal mucus data from Figure 3-1.

of these materials is rheologically reversible, so that solid-like properties are regained when the stress is reduced below the yield stress, and the test can be repeated to give the same data.

Each yield stress material exhibits a finite, but large, viscosity at low stress. The viscosity for each material is so high that it is solid-like for timescales on the order of seconds, which is the relevant timescale of locomotion for natural snails [30] and Chan's mechanical crawler. For example, with a viscosity $\eta \approx 10^7$ Pa.s, and a fluid thickness $h = 1$ mm, Chan's crawler would slump down a vertical wall at a rate of only 30 μm/hr. At a critical stress the viscosity drops by several decades. Since flow exists at any finite stress, none of these materials exhibits a true yield stress, but rather display an apparent yield stress. Native slime and Laposlime share a steep and dramatic drop in viscosity at the yield stress, whereas the viscosity of Carboslime drops less quickly as the stress is increased. The steepness of this drop is quantified by the Bingham number, as mentioned in Chapter 5, where $Bn = 1$ corresponds to $\tau_y = \tau_{flow}$, indicating a vertical drop in viscosity as a function of stress.

The drop in viscosity of Laposlime occurs over such a narrow range of stress that a stress-sweep could not capture the behavior. Thus, a rate-sweep was performed from high shear-rates down to low shear-rates. This technique allows for large changes in viscosity to be measured over a small change in stress. A rate-sweep is limited by the smallest rotational rate that the rheometer's control loop can manage ($\omega_{min} \approx 10^{-3}$ rad.s^{-1} for the AR1000), thus a stress-sweep was used to explore the high viscosity ($\omega < \omega_{min}$) region of the flow curve. Stress-sweep tests quickly reveal the time-dependent nature of Laposlime's yield stress. The sample is deformed so little during a sweep from low to high stress that the network has time to grow, resulting in a larger apparent yield stress than determined by the rate-sweep tests (this time-dependent yield stress could be used to quantify the thixotropy of the material). The stress-sweep data have therefore been truncated to be consistent with the rate-sweep data.

The data for both simulants show that the yield stress is a strong function of concentration. The maximum yield stress of each simulant is limited by the imprac-

ticality of increasing the concentration beyond a certain point. Extremely high yield stress materials are also difficult to test, since they suffer from slip at the boundaries [57]. Laposlime at 7% is prone to slipage at the boundary, as can be witnessed by observing the edge of the sample during the test [58]. Thus, the data reported in in Figure 6-2 give the apparent viscosity for a gap $h = 1000$ μm; if slip is occurring then the measured viscosity will be a function of gap height.

6.2 Creep

Linear viscoelastic material properties were examined using creep and small amplitude oscillation tests. Native slime is compared to simulants which have similar yield stress values: a Carboslime at 2% and a Laposlime at 5%, each having a yield stress $\tau_y \approx 100$ Pa. The linear rheological regime is defined such that the material properties are not a function of the input stress amplitude, and thus each creep and oscillation test in the linear regime is performed below the yield stress ($\tau_0 << \tau_y$). Figures 6-3 and 6-4 show the creep response of Carboslime 2% and Laposlime 5%. The creep compliance of native slime, from Figure 3-2, is included for reference.

Each simulant initially shows a dominant elastic response, followed by a small amount of flow, as indicated by the slight slope of the compliance curve. The average compliance of Carboslime and Laposlime are noticeably smaller than native pedal mucus, indicating that these materials are stiffer at small strains. At short times a damped inertio-elastic ringing can be seen for each material, as was observed with native slime in Figure 3-2. If the inertial contribution is known, then the storage modulus G' and loss modulus G'' can be determined at the free oscillation ringing frequency, as was done with native slime in Section 3.1. This analysis will not be performed on Carboslime or Laposlime. Note that the ringing frequency of Laposlime is so high that under-sampling occurs, and the signal is aliased.

At sufficiently long times the slope of each compliance curve approaches a constant. The rate of change of compliance with time is exactly equal to the inverse of viscosity, and the steady state values match well with the large finite viscosity of each material

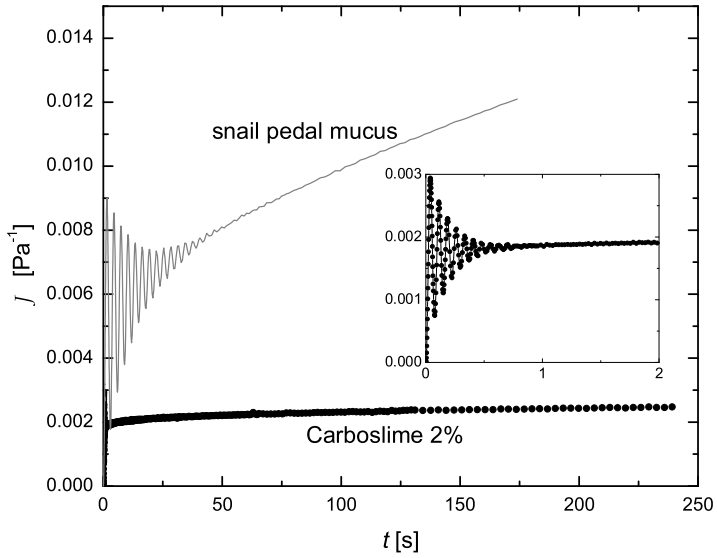

Figure 6-3: Creep compliance of Carboslime 2.0% (AR1000, T=25°C, solvent trap; D=4 cm plate with sandpaper, h=1000 μm, τ_0 = 5 Pa). Pedal mucus data from Figure 3-2.

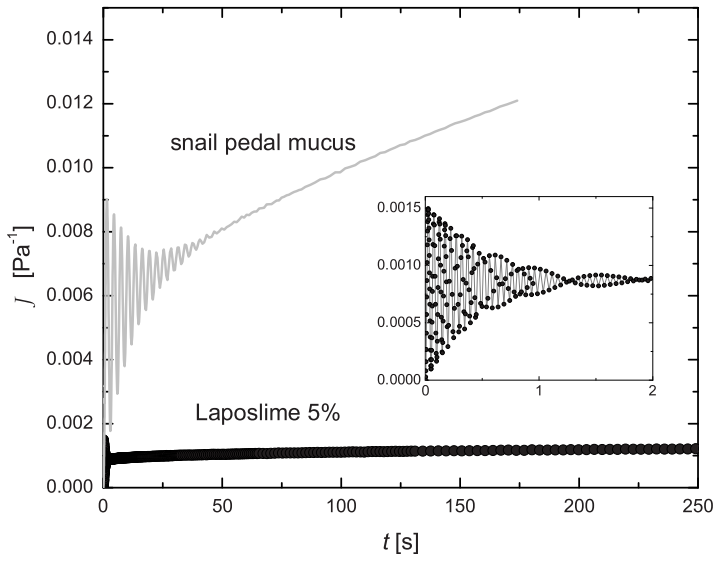

Figure 6-4: Creep compliance of Laposlime 5% (AR1000, T=25°C, solvent trap; D=4 cm plate with sandpaper, h=1000 μm, τ_0 = 20 Pa). Pedal mucus data from Figure 3-2.

below the yield stress; for Carboslime $\eta = (dJ/dt)^{-1} = 2 \times 10^5$ Pa.s, and for Laposlime $\eta = (dJ/dt)^{-1} = 3 \times 10^6$ Pa.s.

6.3 Small amplitude oscillatory shear (SAOS)

The linear viscoelastic moduli, G' and G'', were examined at multiple frequencies with SAOS. Both G' and G'' were found to be weak functions of frequency for each material below the yield stress, as shown in Figures 6-5 and 6-6. Although each material has approximately the same yield stress, the storage moduli vary across an order of magnitude; native slime has the lowest elastic modulus, near 200 Pa, whereas the Laposlime has a storage modulus $G' \approx$2000 Pa. Thus, although the yield stress is comparable, the elastic stiffness of the particulate gel simulant shown in Figure 6-6 is a factor of ten larger than native slime. This comparative stiffness is consistent with the creep compliance results.

The loss tangent of each material is shown as a function of frequency in Figure 6-7. The loss tangent is defined as $\tan\delta = G''/G'$, and thus compares the magnitudes of the viscoelastic moduli. The loss tangent of each material is on the order of 0.1 for most of the frequency range. The notable exception is Laposlime, in which the loss tangent goes down to approximately 0.02 at higher frequencies, indicating that the elastic modulus is nearly two orders of magnitude larger than the loss modulus.

6.4 Nonlinear, large amplitude oscillation

The first harmonic storage modulus G'_1 and loss modulus G''_1 are shown in Figures 6-8 and 6-9 as a function of stress amplitude τ_0 at a fixed frequency of $\omega = 1$ rad/s. At low stresses each material shows a very weak or no dependence on the input stress amplitude. Each material undergoes a transition at a critical stress at which the elastic response dramatically decreases. As mentioned previously, no data could be collected for native slime beyond this critical stress since the material was ejected from the gap. The critical stress amplitude for this transition corresponds approximately

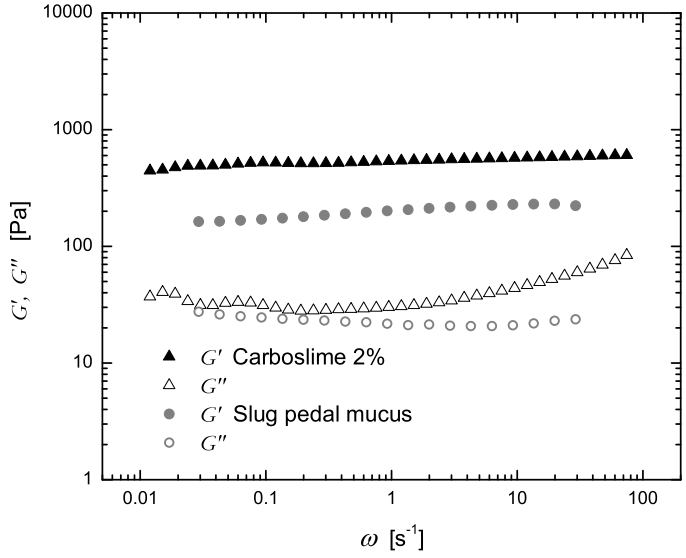

Figure 6-5: Frequency dependent viscoelastic moduli of Carboslime 2.0% (AR1000, D=4 cm plate with sandpaper, h=1000 μm, T=25°C, solvent trap, $\tau_0 = 5$ Pa). Pedal mucus data from Figure 3-4.

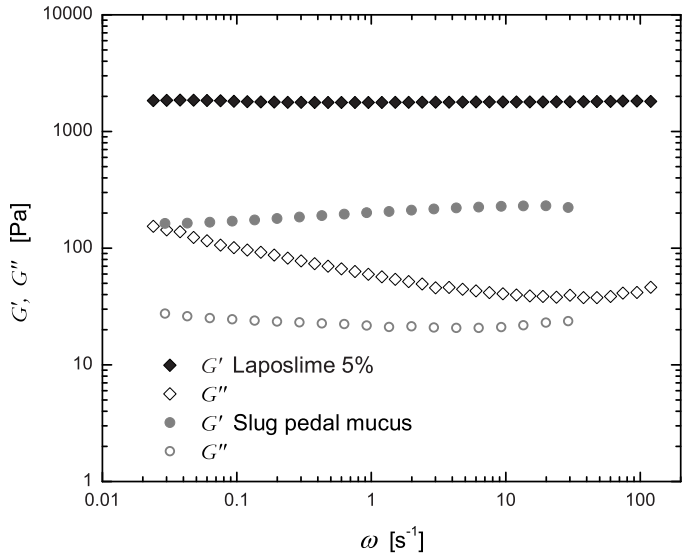

Figure 6-6: Frequency dependent viscoelastic moduli of Laposlime 5% (AR1000, T=25°C, solvent trap; D=4 cm plate with sandpaper, h=1000 μm, $\tau_0 = 20$ Pa). Pedal mucus data from Figure 3-4.

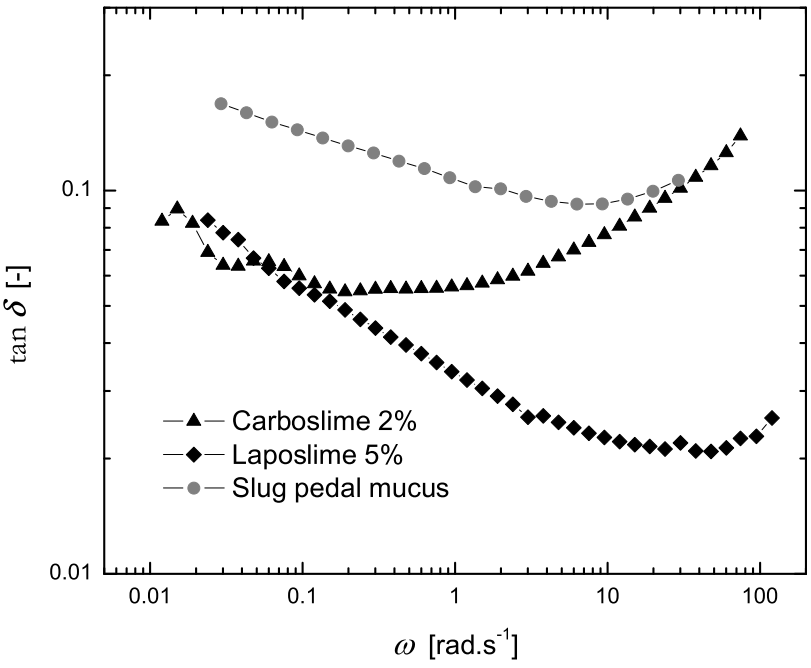

Figure 6-7: Loss tangent of Carboslime 2.0% and Laposlime 5%, compared to native pedal mucus; same protocols as Figure 6-5 and Figure 6-6. Pedal mucus data from Figure 3-4.

to the apparent yield stress in steady flow tests. The sharpness of the transition also corresponds with the steady shear flow results; the polymer gel Carboslime exhibits a soft shoulder transition, whereas the slime and particulate gel Laposlime show a sharp transition.

As the stress amplitude approaches the yield stress, a minor difference can be seen in the behavior of G_1' and G_1'' for each material. The loss modulus G_1'' appears to increase just before yield for each material; this increase is most pronounced with the Carboslime. The increase in G_1'' prior to yield, combined with a decrease in G_1', has been observed in other materials and is classified as type III behavior by Hyun and coworkers [59]. The variation of the first harmonic storage modulus is less interesting as the yield stress is approached; in each case G_1' is a weak function of stress amplitude for $\tau_0 < \tau_y$. However, upon closer inspection, a dramatic difference in the material response leading up to failure becomes apparent.

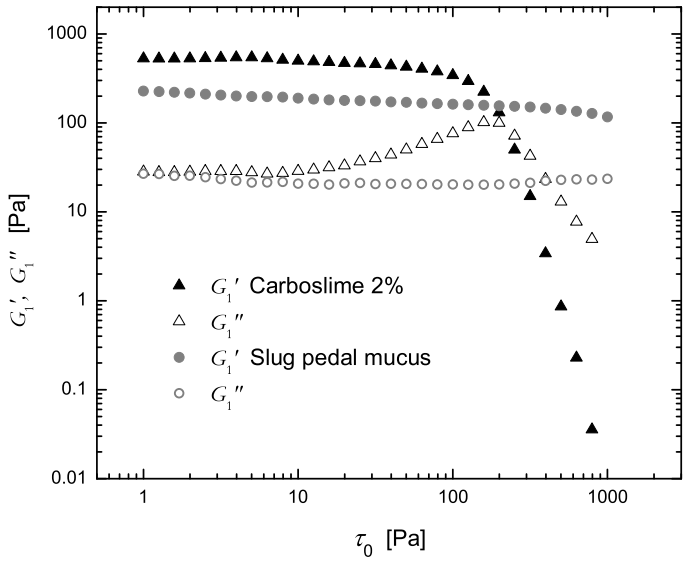

Figure 6-8: Stress dependent viscoelastic moduli of Carboslime 2.0% (AR1000, T=25°C, solvent trap; D=4 cm plate with sandpaper, h=1000 μm, $\omega = 1$ rad.s^{-1}). Pedal mucus data from Figure 3-3.

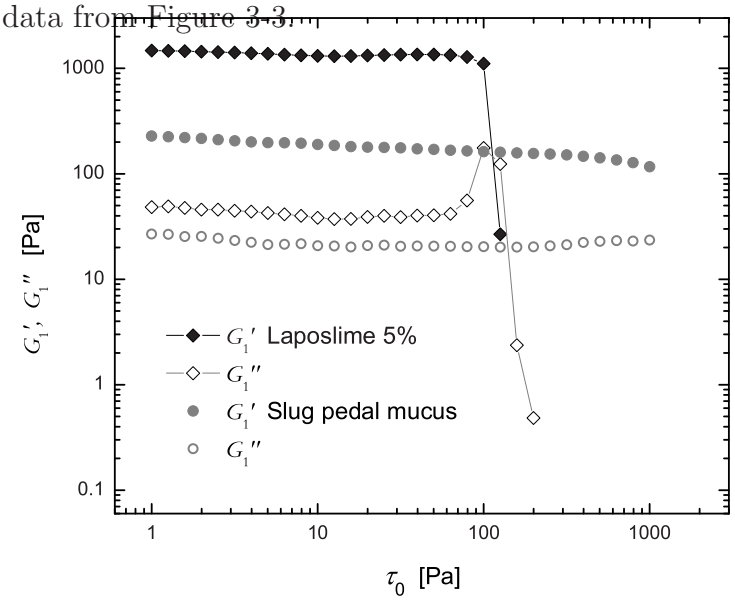

Figure 6-9: Stress dependent viscoelastic moduli of Laposlime 5% (AR1000, T=25°C, solvent trap; D=4 cm plate with sandpaper, h=1000 μm, $\omega = 1$ rad.s^{-1}). Pedal mucus data from Figure 3-3.

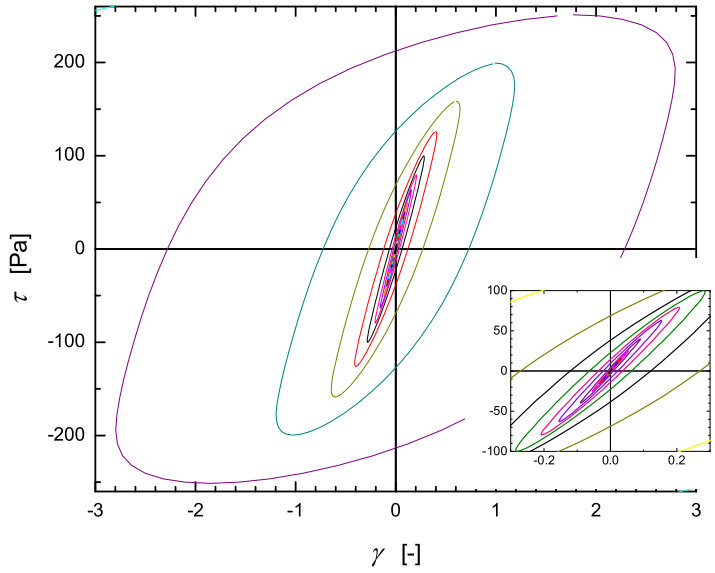

Figure 6-10: Lissajous curves of Carboslime 2.0%, from oscillatory stress sweep of Figure 6-8 (AR1000, T=25°C, solvent trap; D=4 cm plate with sandpaper, h=1000 μm).

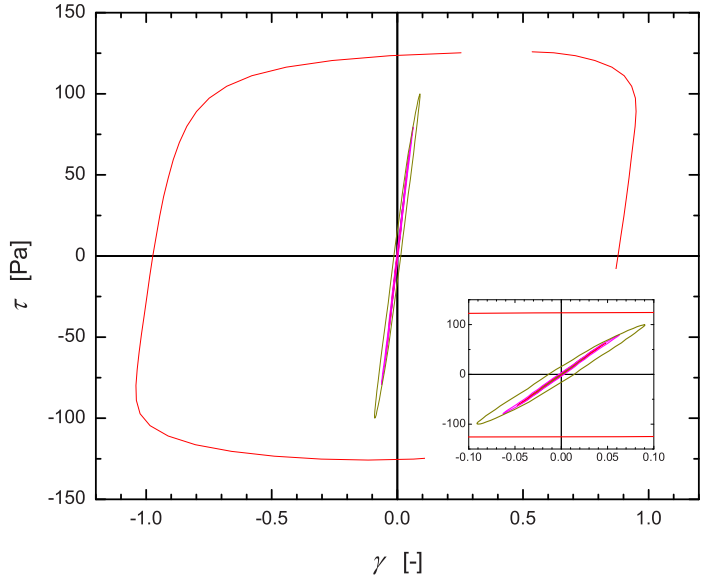

Figure 6-11: Lissajous curves of Laposlime 5%, from oscillatory stress sweep of Figure 6-9 (AR1000, T=25°C, solvent trap; D=4 cm plate with sandpaper, h=1000 μm).

With the aid of a Lissajous curve one can immediately see the substantial difference in each material's non-linear response to an oscillatory stress input, as shown in Figures 6-10 and 6-11. As outlined in Section 2.3.2, Lissajous curves are parametric plots of stress upon strain, with each curve corresponding to a particular frequency and stress amplitude.

The Lissajous curves of each material at low stress appear as tight ellipses (see insets in Figures 6-10 and 6-11) indicating $G' >> G''$, thus only a small area is enclosed and the response is dominated by elasticity. As the stress amplitude is increased toward the yield stress, each material exhibits distinctive behavior. The Laposlime maintains tight ellipse curves almost all the way up to yield, and subsequently undergoes a quick transition to viscous behavior, shown by a dramatic increase in the area enclosed by the curve. This transition is consistent with the sudden drop in viscosity for the steady shear flow curves. The Carboslime Lissajous curves (Figure 6-10) gradually broaden to enclose more area, and thus show a gradual transition from elastic to viscous behavior. This soft transition is consistent with the steady shear flow tests and the behavior of G_1' and G_1'' as the oscillatory stress amplitude is increased.

In contrast to both simulants, native slime exhibits a strongly nonlinear response leading up to yield. As summarized with the Pipkin diagram of Figure 3-18, for native slime the elliptical curves which appear at low stresses become exceedingly distorted as stress is increased, and appear to be strain-stiffening. The strain-stiffening reported for native slime is not mimicked by either the Carboslime or Laposlime simulants.

6.5 Time dependency of yield stress

As discussed in Section 4.3.3, the apparent yield stress, or critical stress, of a material may depend on how long the sample has been at rest since it was last yielded, i.e. how much time it has been allowed to restructure. Furthermore, the maximum velocity of a mechanical crawler is inversely proportional to the restructuring time (Equation 4.40).

The restructuring times of Carboslime and Laposlime were examined with stress overshoot tests. Figure 6-12 displays the sequence of a stress overshoot test. The

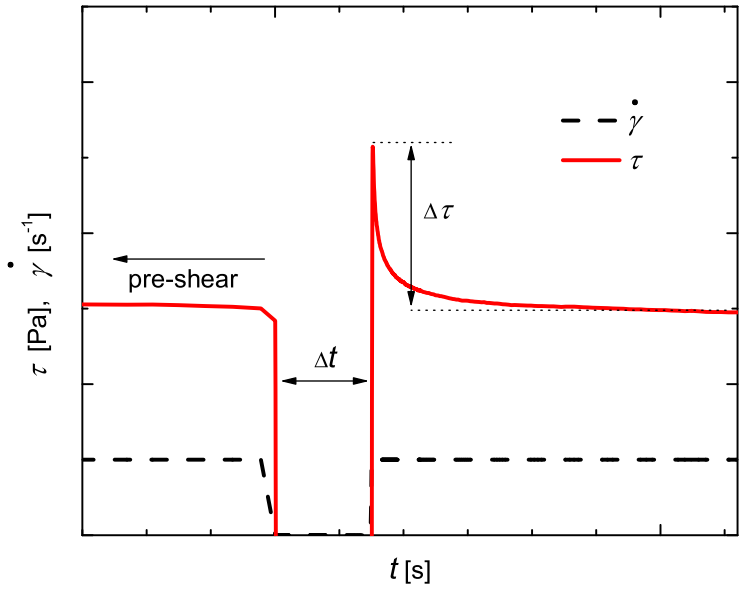

Figure 6-12: Experimental procedure for determining a stress overshoot which depends on rest time.

sample is first "pre-sheared" to yield the material and erase strain history effects. The pre-shear is abruptly brought to a halt, at which point the sample is allowed to rest for a time Δt. A step-strain-rate is then imposed, which yields the sample. The overshoot stress $\Delta\tau$ is then determined as the difference between the peak stress and the steady flow stress.

The overshoot stress is not quantitatively equivalent to the yield stress as defined in this work. However, it is closely related to the yield stress, since it is the peak stress which occurs as the material is ruptured. The overshoot stress is a combination of elastic breaking stress and flow stress, and will therefore depend on the shear-rate.

A possible form of the time dependent yield stress was suggested with Equation 4.28. The same form of that equation will be used for fitting the time-dependency of the overshoot stress, since zero overshoot stress may be expected if the sample is not allowed to restructure ($\Delta t = 0$), and a steady state value of overshoot stress is achieved for sufficient rest times. An exponential approach to a long-rest-time $\Delta\tau$ is

	Fitting Parameter	Carboslime 2%	Laposlime 3%
Equation 6.1 exponential	A [Pa]	4.59 ±0.19	35.70 ±2.43
	λ [s]	0.82 ±0.15	17.34 ±3.44
	R^2 [-]	0.870	0.961
Equation 6.2 stretched exponential	A [Pa]	4.98 ±0.21	64.99 ±7.0
	λ [s]	0.749 ±0.098	88.2 ±25
	B [-]	0.451 ±0.083	0.594 ±0.019
	R^2 [-]	0.997	0.9995

Table 6.1: Fitting parameters and confidence intervals for stress overshoot data of Carboslime 2% and Laposlime 3%.

expressed as

$$\Delta\tau = A\left(1 - e^{-\Delta t/\lambda}\right) \tag{6.1}$$

where A is the maximum overshoot stress at long rest times and λ is the characteristic restructuring time. Here λ is assumed to represent the restructuring time of both the overshoot stress and the yield stress.

An extra parameter can be added to Equation 6.1 to represent a "stretched-exponential" approach to a maximum overshoot stress. Stretched exponentials have been observed with numerous systems and have been associated with the presence of fractal networks [60]. A stretched exponential approach to a long-rest-time $\Delta\tau$ is given by

$$\Delta\tau = A\left(1 - e^{-(\Delta t/\lambda)^B}\right) \tag{6.2}$$

where λ is still regarded as the restructuring time of the material and B is the stretching exponent.

The results of time-dependent overshoot tests for the simulants are shown in Figures 6-13 and 6-14. The Laposlime sample is at a concentration of 3%. Laposlime was pre-sheared at $\dot{\gamma} = 5\ \mathrm{s}^{-1}$ for 60 seconds; Carboslime was pre-sheared at $\dot{\gamma} = 5\ \mathrm{s}^{-1}$ for five seconds (less shearing was needed to eliminate strain history effects with the Carboslime). Each was allowed to rest for a specified time and then sheared at

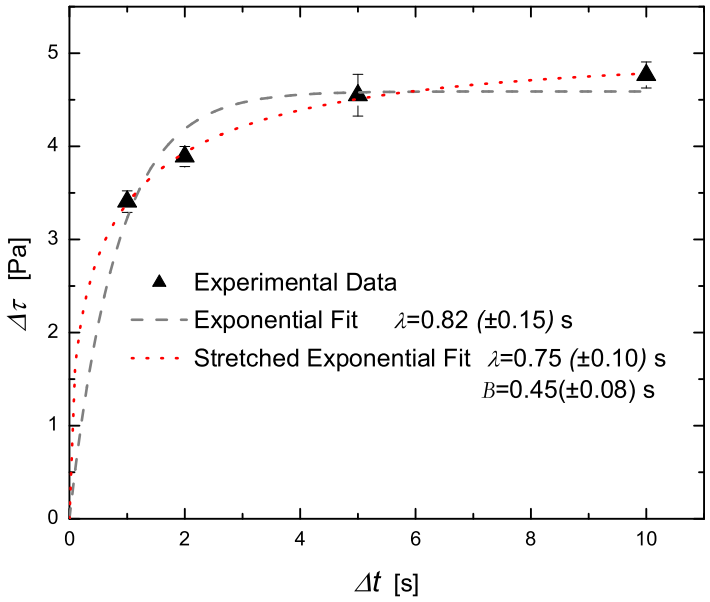

Figure 6-13: Time-dependent stress overshoot of Carboslime 2.0% (ARES, T=25°C, solvent trap; D=5.0 ~~cm 1° cone~~).

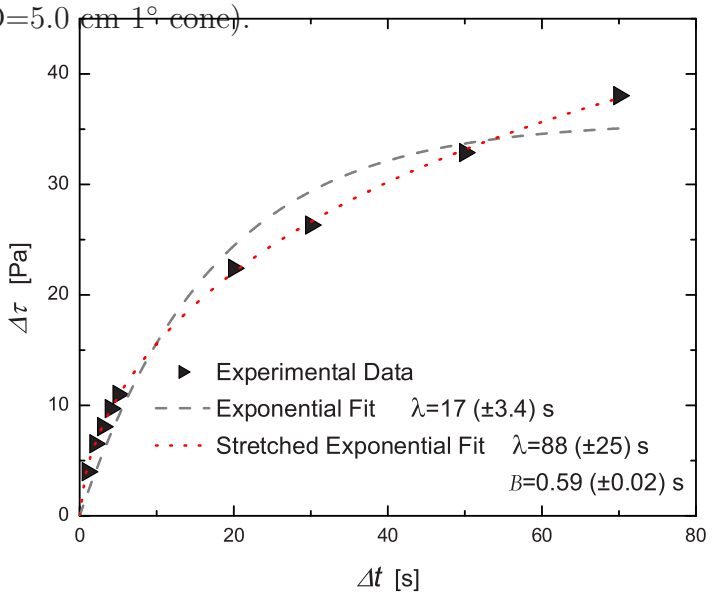

Figure 6-14: Time-dependent stress overshoot of Laposlime 3.0% (ARES, T=25°C, solvent trap; D=5.0 cm 1° cone).

$\dot{\gamma} = 5\ s^{-1}$. Error bars are shown for the Carboslime data since each test was repeated three times. Each data set has been fit to Equations 6.1 and 6.2. Table 6.1 reports

the fitting results.

For a yield stress that grows in a similar fashion to Equation 6.1, the restructuring time λ was shown to be inversely related to the maximum velocity of a crawler (Equation 4.40). The Carboslime has a much faster restructuring time than the Laposlime. The restructuring time of Carboslime is $\lambda \approx 0.8$ s, whereas the restructuring time of Laposlime is $\lambda \approx 17$ s. Thus, the maximum velocity of a mechanical crawler on Carboslime would be approximately 20 times that of a crawler on Laposlime. The restructuring times determined by fitting Equation 6.2 (stretched-exponential) are also dramatically different ($\lambda \approx 90$ s for Laposlime and $\lambda \approx 0.7$ s for Carboslime).

6.6 Summary

The two simulants compared in this chapter have similar yield stresses, but when examined in detail, in linear and nonlinear deformations, show some differences in rheological properties. Table 6.2 summarizes the results of this chapter.

Laposlime yields and transitions to a steady flow response over a much narrower range of stress than Carboslime, and therefore Laposlime has a much higher Bingham number. In this respect, Laposlime is more similar to native pedal mucus. However, Laposlime is much stiffer and more elastic than both Carboslime and native pedal mucus. Laposlime is approximately ten times as stiff as native slime; Carboslime is approximately three times as stiff.

The non-linear rheology of Carboslime and Laposlime are quite different, in that Laposlime undergoes a very quick transition to yield, whereas Carboslime gradually transitions to yield, as shown by the Lissajous curves in Figures 6-10 and 6-11. The quick yield transition of Laposlime is typical for a particulate gel. Furthermore, neither of these simulants mimics the strain-stiffening observed with native pedal mucus (Figure 3-18).

Finally, the restructuring time of the simulants are an order of magnitude different from each other. This is the most dramatic difference between the two simulants and strongly affects their successful use in adhesive locomotion. Once a simulant has been

	Native pedal mucus	Carboslime 2% Polymer gel	Laposlime 5% Particulate gel
Yield stress τ_y [Pa]	100–240	108	90.75
$\eta\|_{\dot{\gamma}=10\ s^{-1}}$ [Pa.s]	10.4–25	31.6	9.6
$Bn\|_{\dot{\gamma}=10\ s^{-1}}$ [-]	0.96	0.34	0.95
$G'\|_{\omega=1\ rad.s^{-1}}$ [Pa]	200	540	1800
$G''\|_{\omega=1\ rad.s^{-1}}$ [Pa]	20	30	60
Pre-yield stiffening	Yes	No	No
Restructuring time [s]	-	0.8	17

Table 6.2: Summary of rheological properties of two simulants with a similar apparent yield stress; properties of native pedal mucus shown for reference.

shown to provide an adequate yield stress for inclined locomotion, the restructuring time of the material should be examined, since this property is directly related to the maximum crawler velocity, as discussed in Section 4.3.3. Therefore, of the two simulants analyzed in this chapter, Carboslime is the better candidate for aiding adhesive locomotion.

Chapter 7

Conclusions

The contributions of this thesis can be can be summarized as follows.

Chapter 2 introduced a new characterization technique for analyzing the non-linear shear rheology of materials, by quantifying the non-linear elastic response. Section 2.3.3 introduced three measures for quantifying non-linear elasticity in oscillatory shear:

1. M: Small strain elastic shear modulus; reduces to G' in linear viscoelastic regime.

2. L: Large strain elastic shear modulus; reduces to G' in linear viscoelastic regime.

3. S: Elastic stiffening ratio; $S = 1$ in linear viscoelastic regime.

These measures provide a physical interpretation of non-linear behavior.

Chapter 3 reported the detailed rheology of native pedal mucus from terrestrial gastropods (the terrestrial snail *Helix aspera* and the terrestrial slug *Limax maximus*). Pedal mucus from terrestrial gastropods has been known to exhibit a yield stress [4], but this thesis reported the first ever examination of progressive transition to yield with increasing oscillatory shear stress amplitude. Lissajous curves were used to represent graphically the rheological response, which indicated strain-stiffening behavior. The newly proposed quantitative measures of non-linear elasticity were applied to this data, and they quantified the strain-stiffening of pedal mucus. The

maximum elastic stiffening ratio observed was $S_{max} \approx 4.5$. Strain-stiffening has been observed in other biological materials [61], but has typically been reported only by monitoring the first harmonic storage modulus G_1' and its dependence upon input amplitude, e.g. γ_0. This thesis demonstrates that strain-stiffening can exist (Figure 3-15) even though the first harmonic modulus G_1' decreases (Figure 3-7). Finally, a Pipkin diagram was used to map the non-linear rheology and provide a complete "rheological fingerprint" of pedal mucus (Figure 3-18).

Chapter 4 developed the design and optimization criteria for a fluid which would enable adhesive locomotion. It was shown that any fluid with a non-Newtonian shear viscosity can be used for horizontal adhesive locomotion, and that shear-thickening fluids can be more efficient that yield stress fluids on horizontal terrain. For adhesive locomotion on an inclined surface, using the most general yield stress fluid model which includes a restructuring time (Equation 4.28), the following properties of the fluid should be sought:

1. A minimum yield stress $\tau_y > \tau_{y,min}^d$ (Equation 4.23), which is required for adhesive locomotion on an inclined surface.

2. Post-yield viscosity, minimized to increase speed (Equation 4.26).

3. Non-dimensional yield stress τ^* (Equation 4.35), minimized to increase crawler speed (Figure 4-5).

4. Restructuring time λ of a yield stress fluid (Equation 4.28), minimized to increase speed (Equation 4.40).

Furthermore, locomotive efficiency ε for a simple yield stress fluid is only a function of ϕ, the fraction of the crawler that iteratively moves forward (Table 4.2).

Chapters 5 and 6 were devoted to the search for a suitable slime simulant to be used with Chan's Robosnail (Figure 1-2). Dozens of materials were surveyed, including polymer gels, particulate gels, emulsions, foams, composites, and field-responsive fluids. The results support the feasibility of a mechanical wall climber without needing to harvest native slime, that is, commercially available materials could be used with

Chan's Robosnail for adhesive locomotion on any incline. Two promising simulants were examined in detail in Chapter 6: a polymeric gel and a particulate gel simulant (Table 6.2). Both materials had similar yield stresses, but the restructuring time of the polymer gel was an order of magnitude less than the particulate gel. Thus the polymer gel, Carboslime (material preparation given in Section 5.1.1) is the better material for use in adhesive locomotion.

Appendix A

Biochemistry Reference

	Abbrev.	Full Name
A	Ala	Alanine
C	Cys	Cysteine
D	Asp	Aspartic acid
E	Glu	Glutamic acid
F	Phe	Phenylalanine
G	Gly	Glycine
H	His	Histidine
I	Ile	Isoleucine
K	Lys	Lysine
L	Leu	Leucine
M	Met	Methionine
N	Asn	Asparagine
P	Pro	Proline
Q	Gln	Glutamine
R	Arg	Arginine
S	Ser	Serine
T	Thr	Threonine
V	Val	Valine
W	Trp	Tryptophan
Y	Tyr	Tyrosine

Table A.1: Amino acids and their abbreviations

Bibliography

[1] J. Dekker, J. W. A. Rossen, H. A. Buller, and A. W. C. Einerhand. The MUC family: an obituary. *Trends in Biochemical Sciences*, 27(3):126–131, 2002.

[2] C. Taylor, K. I. Draget, J. P. Pearson, and O. Smidsrod. Mucous systems show a novel mechanical response to applied deformation. *Biomacromolecules*, 6(3):1524–1530, 2005.

[3] J. F. Grenon and G. Walker. Biochemical and rheological properties of the pedal mucus of the limpet, patella-vulgata l. *Comparative Biochemistry and Physiology B-Biochemistry and Molecular Biology*, 66(4):451–458, 1980.

[4] M. W. Denny and J. M. Gosline. The physical-properties of the pedal mucus of the terrestrial slug, ariolimax-columbianus. *Journal of Experimental Biology*, 88(OCT):375–393, 1980.

[5] B. Chan, N. J. Balmforth, and A. E. Hosoi. Building a better snail: Lubrication and adhesive locomotion. *Physics of Fluids*, 17(11), 2005.

[6] M. W. Denny. The role of gastropod pedal mucus in locomotion. *Nature*, 285(5761):160–161, 1980.

[7] M. W. Denny. Molecular biomechanics of molluscan mucous secretions. In Peter W. Hochachka, editor, *The Molluska*, volume 1. Metabolic Biochemistry and Molecular Biomechanics. 1983.

[8] S. J. Gendler and A. P. Spicer. Epithelial mucin genes. *Annual Review of Physiology*, 57:607–634, 1995.

[9] J. Perez-Vilar and R. L. Hill. The structure and assembly of secreted mucins. *Journal of Biological Chemistry*, 274(45):31751–31754, 1999.

[10] L. E. Bromberg and D. P. Barr. Self-association of mucin. *Biomacromolecules*, 1(3):325–334, 2000.

[11] M. W. Denny. Invertebrate mucous secretions: Functional alternatives to vertebrate paradigms. In E. Chantler and N. A. Ratcliffe, editors, *Mucus and Related Topics*, volume 43 of *Symposia of the Society for Experimental Biology*. The Company of Biologists Limited, Cambridge, UK, 1989.

[12] R. Denton, W. Forsman, S. H. Hwang, M. Litt, and C.E. Miller. Viscoelasticity of mucus: Its role in ciliary transport of pulmonary secretions. *American Review of Respiratory Disease*, 98(3):380–391, 1968.

[13] M. King. Experimental models for studying mucociliary clearance. *European Respiratory Journal*, 11(1):222–228, 1998.

[14] C. Taylor, A. Allen, P. W. Dettmar, and J. P. Pearson. The gel matrix of gastric mucus is maintained by a complex interplay of transient and nontransient associations. *Biomacromolecules*, 4(4):922–927, 2003.

[15] A. N. Round, M. Berry, T. J. McMaster, S. Stoll, D. Gowers, A. P. Corfield, and M. J. Miles. Heterogeneity and persistence length in human ocular mucins. *Biophysical Journal*, 83(3):1661–1670, 2002.

[16] J. Celli, B. Gregor, B. Turner, N. H. Afdhal, R. Bansil, and S. Erramilli. Viscoelastic properties and dynamics of porcine gastric mucin. *Biomacromolecules*, 6(3):1329–1333, 2005.

[17] A. M. Smith and M. C. Morin. Biochemical differences between trail mucus and adhesive mucus from marsh periwinkle snails. *Biological Bulletin*, 203(3):338–346, 2002.

[18] J.D. Ferry. *Viscoelastic properties of polymers*. Wiley, 3d edition, 1980.

[19] J. M. Dealy and K. F. Wissbrun. *Melt rheology and its role in plastics processing: theory and applications*. Van Nostrand Reinhold, New York, 1990.

[20] R. M. Christensen. *Theory of viscoelasticity: an introduction*. Academic Press Edition: 2nd ed., New York, 1982.

[21] S. N. Ganeriwala and C. A. Rotz. Fourier-transform mechanical analysis for determining the nonlinear viscoelastic properties of polymers. *Polymer Engineering and Science*, 27(2):165–178, 1987.

[22] J. Guo, D. Hwang, G.H. McKinley, C. Tiu, and P.H.T. Uhlherr. Rheological fingerprinting of nonlinear (yield stress) materials. In *XIVth International Congress of Rheology*, Seoul, Korea, 2004.

[23] M. Wilhelm. Fourier-transform rheology. *Macromolecular Materials and Engineering*, 287(2):83–105, 2002.

[24] T. T. Tee and J. M. Dealy. Nonlinear viscoelasticity of polymer melts. *Transactions of the Society of Rheology*, 19(4):595–615, 1975.

[25] C. Clasen and G. H. McKinley. Gap-dependent microrheometry of complex liquids. *Journal of Non-Newtonian Fluid Mechanics*, 124(1-3):1–10, 2004.

[26] G. A. Davies and J. R. Stokes. On the gap error in parallel plate rheometry that arises from the presence of air when zeroing the gap. *Journal of Rheology*, 49(4):919–922, 2005.

[27] H. A. Barnes and K. Walters. The yield stress myth. *Rheologica Acta*, 24(4):323–326, 1985.

[28] H. A. Barnes. The yield stress - a review or 'pi alpha nu tau alpha rho epsilon iota' - everything flows? *Journal of Non-Newtonian Fluid Mechanics*, 81(1-2):133–178, 1999.

[29] C. Baravian and D. Quemada. Using instrumental inertia in controlled stress rheometry. *Rheologica Acta*, 37(3):223–233, 1998.

[30] M. W. Denny. A quantitative model for the adhesive locomotion of the terrestrial slug, ariolimax-columbianus. *Journal of Experimental Biology*, 91(APR):195–217, 1981.

[31] S. Vogel. *Life in moving fluids: the physical biology of flow*. Princeton University Press, 2nd edition, 1994.

[32] H. A. Barnes. Thixotropy - a review. *Journal of Non-Newtonian Fluid Mechanics*, 70(1-2):1–33, 1997.

[33] Z. Y. Wang, Q. Z. Zhang, M. Konno, and S. Saito. Sol-gel transition of alginate solution by the addition of various divalent-cations - a rheological study. *Biopolymers*, 34(6):737–746, 1994.

[34] M. Marcotte, A. R. T. Hoshahili, and H. S. Ramaswamy. Rheological properties of selected hydrocolloids as a function of concentration and temperature. *Food Research International*, 34(8):695–703, 2001.

[35] V. B. Pai and S. A. Khan. Gelation and rheology of xanthan/enzyme-modified guar blends. *Carbohydrate Polymers*, 49(2):207–216, 2002.

[36] P. A. Padmanabhan, D. S. Kim, D. Pak, and S. J. Sim. Rheology and gelation of water-insoluble dextran from Leuconostoc mesenteroides NRRL B-523. *Carbohydrate Polymers*, 53(4):459–468, 2003.

[37] T. Aubry and M. Moan. Rheological behavior of a hydrophobically associating water-soluble polymer. *Journal of Rheology*, 38(6):1681–1692, 1994.

[38] T. M. Aminabhavi, S. A. Agnihotri, and B. V. K. Naidu. Rheological properties and drug release characteristics of ph-responsive hydrogels. *Journal of Applied Polymer Science*, 94(5):2057–2064, 2004.

[39] A. Lindner, P. Coussot, and D. Bonn. Viscous fingering in a yield stress fluid. *Physical Review Letters*, 85(2):314–317, 2000.

[40] Noveon Inc. Neutralizing carbopol and pemulen polymers in aqueous and hydroalcoholic systems, 1998.

[41] N. W. Taylor and E. B. Bagley. Dispersions or solutions - mechanism for certain thickening agents. *Journal of Applied Polymer Science*, 18(9):2747–2761, 1974.

[42] J. O. Carnali and M. S. Naser. The use of dilute-solution viscometry to characterize the network properties of carbopol microgels. *Colloid and Polymer Science*, 270(2):183–193, 1992.

[43] N. Yildiz, Y. Sarikaya, and A. Calimli. The effect of the electrolyte concentration and pH on the rheological properties of the original and the Na2CO3-activated Kutahya bentonite. *Applied Clay Science*, 14(5-6):319–327, 1999.

[44] S. Isci, E. Gunister, O. I. Ece, and N. Gungor. The modification of rheologic properties of clays with pva effect. *Materials Letters*, 58(12-13):1975–1978, 2004.

[45] N. J. Alderman, G. H. Meeten, and J. D. Sherwood. Vane rheometry of bentonite gels. *Journal of Non-Newtonian Fluid Mechanics*, 39(3):291–310, 1991.

[46] Y. Zhong and S. Q. Wang. Exfoliation and yield behavior in nanodispersions of organically modified montmorillonite clay. *Journal of Rheology*, 47(2):483–495, 2003.

[47] O. M'Bodj, N. K. Ariguib, M. T. Ayadi, and A. Magnin. Plastic and elastic properties of the systems interstratified clay-water-electrolyte-xanthan. *Journal of Colloid and Interface Science*, 273(2):675–684, 2004.

[48] P. H. T. Uhlherr, J. Guo, C. Tiu, X. M. Zhang, J. Z. Q. Zhou, and T. N. Fang. The shear-induced solid-liquid transition in yield stress materials with chemically different structures. *Journal of Non-Newtonian Fluid Mechanics*, 125(2-3):101–119, 2005.

[49] A. Mourchid, E. Lecolier, H. Van Damme, and P. Levitz. On viscoelastic, birefringent, and swelling properties of laponite clay suspensions: Revisited phase diagram. *Langmuir*, 14(17):4718–4723, 1998.

[50] F. Pignon, A. Magnin, J. M. Piau, B. Cabane, P. Lindner, and O. Diat. Yield stress thixotropic clay suspension: Investigation of structure by light, neutron, and x-ray scattering. *Physical Review E*, 56(3):3281–3289, 1997.

[51] D. Bonn, H. Kellay, H. Tanaka, G. Wegdam, and J. Meunier. Laponite: What is the difference between a gel and a glass? *Langmuir*, 15(22):7534–7536, 1999.

[52] J. R. Stokes and J. H. Telford. Measuring the yield behaviour of structured fluids. *Journal of Non-Newtonian Fluid Mechanics*, 124(1-3):137–146, 2004.

[53] G. P. Citerne, P. J. Carreau, and M. Moan. Rheological properties of peanut butter. *Rheologica Acta*, 40(1):86–96, 2001.

[54] L. Ma and G. V. Barbosacanovas. Rheological characterization of mayonnaise.2. flow and viscoelastic properties at different oil and xanthan gum concentrations. *Journal of Food Engineering*, 25(3):409–425, 1995.

[55] S. S. Deshmukh. *Field-responsive ('Smart') fluids for advanced automotive applications*. SM Thesis, Massachusetts Institute of Technology, 2003.

[56] Y. L. Zhang, K. Q. Lu, G. H. Rao, Y. Tian, S. H. Zhang, and J. Liang. Electrorheological fluid with an extraordinarily high yield stress. *Applied Physics Letters*, 80(5):888–890, 2002.

[57] H. A. Barnes. A review of the slip (wall depletion) of polymer-solutions, emulsions and particle suspensions in viscometers - its cause, character, and cure. *Journal of Non-Newtonian Fluid Mechanics*, 56(3):221–251, 1995.

[58] D. M. Kalyon, P. Yaras, B. Aral, and U. Yilmazer. Rheological behavior of a concentrated suspension - a solid rocket fuel simulant. *Journal of Rheology*, 37(1):35–53, 1993.

[59] K. Hyun, S. H. Kim, K. H. Ahn, and S. J. Lee. Large amplitude oscillatory shear as a way to classify the complex fluids. *Journal of Non-Newtonian Fluid Mechanics*, 107(1-3):51–65, 2002.

[60] J. R. Macdonald and J. C. Phillips. Topological derivation of shape exponents for stretched exponential relaxation. *Physical Review E*, 122(7), 2005.

[61] M. L. Gardel, J. H. Shin, F. C. MacKintosh, L. Mahadevan, P. Matsudaira, and D. A. Weitz. Elastic behavior of cross-linked and bundled actin networks. *Science*, 304(5675):1301–1305, 2004.